MARCO GRISON

SINGLE-MOLECULE COHESION AND ADHESION IN MUSCLE CELLS

Dissertation at Physics Department E22
Technische Universität München

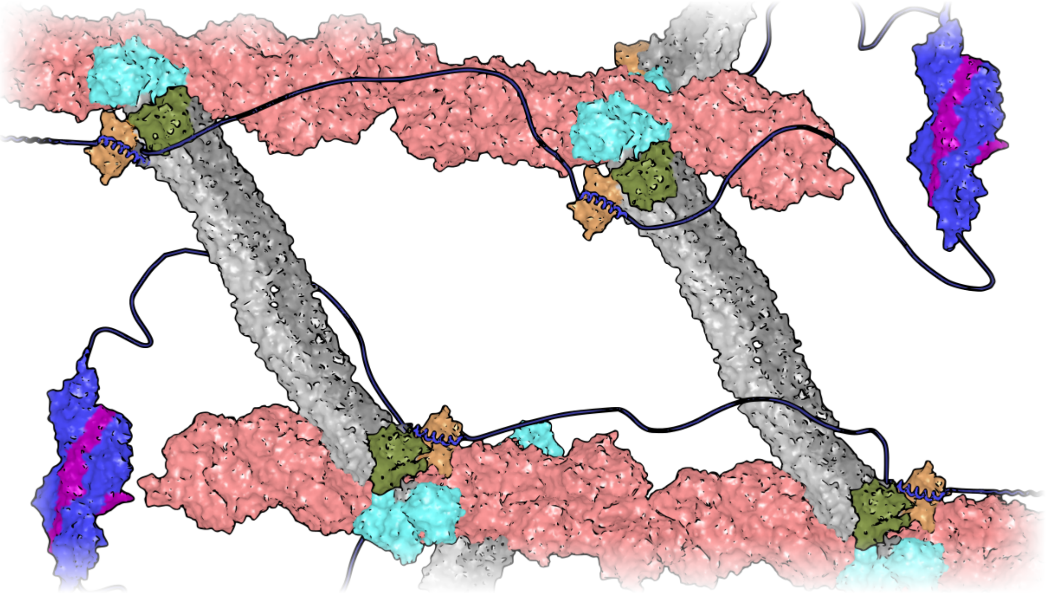

TECHNISCHE UNIVERSITÄT MÜNCHEN
PHYSICS DEPARTMENT

SINGLE-MOLECULE COHESION AND ADHESION IN MUSCLE CELLS

MARCO GRISON

Vollständiger Abdruck der von der Fakultät für Physik der Technischen Universität München zur Erlangung des akademischen Grades eines

Doktors der Naturwissenschaften (Dr. rer. nat.)

genehmigten Dissertation.

Vorsitzender: Prof. Dr. Martin Zacharias

Prüfer der Dissertation:
1. Prof. Dr. Matthias Rief
2. Prof. Dr. Andreas Bausch

Die Dissertation wurde am 05.04.2017 bei der
Technischen Universität München eingereicht und durch die
Fakultät für Physik am 17.05.2017 angenommen.

Marco Grison: *Single-molecule cohesion and adhesion in muscle cells,* ©
April 2017

ABSTRACT

Muscle is the tissue responsible for the locomotion of the body and for the beating of the heart, thanks to its ability to generate active forces upon contraction. A large number of protein/protein interactions are involved in the stabilisation of the muscular tissue. Surprisingly, many of those interactions ehibit low affinities. Hence, the question arises how weak bonds can provide long-term myocyte cohesion and adhesion. The work presented in this thesis deals with two weak protein/protein interactions, the first involving α-actinin and titin, the other talin and integrin. To mechanically probe the strength of the bonds between single protein pairs, optical tweezers were employed, since they allow high resolution force measurements in the low-piconewton range.

Titin acts as a molecular spring, restoring the muscle resting length after the tissue is streched, but how it is connected to the cytoskeleton is still a matter of debate. The interaction of titin with the actin crosslinker α-actinin has been proposed as a candidate for titin anchoring. Upon force application with optical tweezers, we found that the bond between α-actinin and titin broke apart at forces lower than those which are physiologically relevant. The unbinding forces were strongly dependent on the pulling geometry, but the lifetime of a single bond never exceeded 2 s. Since titin has seven similar α-actinin binding motifs, we probed different interactions and observed that only three motifs bind α-actinin with significant mechanical stability. We propose a model explaining how the concerted action of many parallel bonds can provide long-term anchoring of titin.

With similar methods we studied the interaction between talin and integrin, required for the lateral adhesion of parallel myocytes and for the connection with tendon cells. We found talin and integrin to detach at low forces, with lifetimes lower than 100 ms even in the absence of load. Such fast kinetics suggest that a stable connection can be achieved only with many parallel bonds, or if other interactions are involved. We further investigated the affinity of the bond using the competitive binding of an integrin molecule tethered to talin *versus* one free in solution, and measured values comparable to those found in literature. These experiments will facilitate the further investigation of the coordinated role of the cell membrane and different integrin substrates in connecting together the cytoskeleton and the extracellular matrix.

PUBLICATIONS

Some ideas and figures have appeared previously in the following publication:

Grison M, Merkel U, Kostan J, Djinović-Carugo K, Rief M, α-Actinin/titin interaction: A dynamic and mechanically stable cluster of bonds in the muscle Z-disk. *PNAS*, 114(5):1015–1020, January 2017.

And the eighth and final rule:
If this is your first night at Fight Club, you **have** *to fight.*

Tyler Durden

ACKNOWLEDGMENTS

First and foremost I want to express my gratitude to my advisor, Prof. *Matthias Rief*. He taught me the importance of solid scientific method, encouraged my research and supported me throughout failures. Moreover, he is a source of inspiration because of his promotion of an incomparably productive but comfortable atmosphere in the lab.

I would like to acknowledge all the members of the E22, E27 and E69 chairs for their cooperation, feedback and friendship. In particular, my thanks go to *Lorenz Rognoni*, who introduced me to the techniques and the methods. To my (c)office mates *Markus Jahn* and *Philipp Wortmann*, who gracefully put up with my endless complaints. To the lunchy-lunchy crew, who prolonged my life expectancy by keeping me away from the mensa. Especially *Leone Rossetti*, *Francesco Dighera*, *Benni Pelz*, *Kasia Tych* and *Katharina Henneberg*. Kasia deserves a special mention also for editing this text and making it readable to the rest of the world.

I thank *Thomas Suren* and *Fabian Schneider* for being a precious source of friendship, and *Florian Praetorius* and *Matthias Schickinger* for the comments on the obscene Italian comics of the *Alter Ofen*. For fruitful discussions, I want to acknowledge *Alex Mehlich*, *Fabian Ziegler*, *Ulrich Merkel*, *Ziad Ganim*, *Gabriel Zoldak*, *Daniela Bauer*, *Soumit Mandal* and *Andreas Weißl*.

For assisting me to the research facilities I thank *Gabriele Chmel*, *Karin Vogt*, *Monica Rusp* and *Rudi Lehrhuber*. For helping me in the labyrinthine depths of bureaucracy, *Elke Fehlsenfeld*, *Nicole Mittermüller* and *Anne Ploss*.

I am also thankful to our collaborators: *Kristina Djinović-Carugo* and her group—together with *Andrea Ghisleni*—for sharing their knowledge about muscle; *Reinhard Fässler* and his group for helping with comments and ideas; *Lukas Miller* for providing me the precious sequence of a long protein linker, and *Magnus Bauer* for the assistance in the ybbR-tag conjugation. I also want to thank three of the students I supervised, *Stefan Ernst*, *Maximilian Zwiebel* and *Julia Hirschmann*, for their contribution to the α-actinin project.

A very special gratitude goes to my mother, my father and my sister. They sustained me in my studies and made sacrifices on my behalf.

My last sincere thanks go to *Paola Pecci* for the support and the affection along the years I spent in Munich. Words cannot express how immensely grateful I am to her.

CONTENTS

1 INTRODUCTION 1

I EXPERIMENTAL APPROACH AND METHODS 5

2 SMFS USING OPTICAL TWEEZERS 7
  - 2.1 Single-molecule force spectroscopy 7
  - 2.2 Protein/protein interaction mechanics 8
  - 2.3 Optical Tweezers principles 8
  - 2.4 Experimental setup 10
  - 2.5 Dumbbell assay formation 12
  - 2.6 Experimental assays 13

3 THEORY AND DATA ANALYSIS 17
  - 3.1 Energy landscape theory 17
  - 3.2 Force-ramp analysis 18
  - 3.3 Passive-mode assay 20
  - 3.4 Jump assay 25
  - 3.5 Competition assay 26

II α-ACTININ/TITIN INTERACTION 31

4 TITIN ANCHORING IN THE Z-DISK 33
  - 4.1 The sarcomere is the basic contractile unit of striated muscles 33
  - 4.2 The role of titin in muscle elongation 34
  - 4.3 Titin anchoring in the sarcomere 36
  - 4.4 α-actinin/titin interaction 37
  - 4.5 Summary 38

5 α-ACTININ BINDING TO TITIN Z-REPEAT 7 39
  - 5.1 Constant velocity trace 39
  - 5.2 Unfolding pathway 40
  - 5.3 Kinetics at high forces: jump assay 40
  - 5.4 Force-dependent kinetics and mechanics 41
  - 5.5 Binding affinity: the competition assay 42
  - 5.6 A better estimation of the midpoint force 43
  - 5.7 Pulling on titin T7 only 45
  - 5.8 Summary 46

6 α-ACTININ/TITIN INTERACTION: A CLUSTER OF BONDS 49
  - 6.1 Interaction of α-actinin with other titin Z-repeats 49
  - 6.2 Titin anchoring lifetime estimation 52
  - 6.3 Discussion and outlook 53
  - 6.4 Summary 54

III TALIN/INTEGRIN INTERACTION 57
7 FORCE TRANSDUCTION ACROSS THE CELL MEMBRANE 59
7.1 Integrins transduces force across the membrane 59
7.2 Integrin/talin interaction 60
7.3 Integrin and talin isoform specificity 61
7.4 Open questions 62
8 TALIN/INTEGRIN INTERACTION 63
8.1 T2-β1D and T1-β1A force response 63
8.2 T2-β1D force-dependent kinetics 65
8.3 Two-binding-mode hypothesis 65
8.4 A construct lacking the MP α-helix 66
8.5 Linker-effect hypothesis 67
8.6 A construct with a longer linker 68
8.7 Discussion 69
8.8 Summary 70
9 BINDING AFFINITY AND OUTLOOK 73
9.1 An integrin mutant has a high affinity with talin 73
9.2 The "dead state" issue 75
9.3 Competition with the native β1D integrin tail 76
9.4 Outlook 78
9.5 Summary 80

IV APPENDIX 81
A SUPPLEMENTARY EXPERIMENTS ON α-ACTININ AND TITIN 83
A.1 Bimodal stability of the FB state 83
A.2 The PullA construct and the FU state 86
A.3 Effective concentration of the tethered peptide 87
A.4 Correction of PullT7 rebinding rates 88
B ALTERNATIVE BIOCONJUGATION TECHNIQUES 91
B.1 Introduction 91
B.2 Requirements to get a working dumbbell assay 92
B.3 Beyond cysteine modifications 93
B.4 Protein tags as an alternative approach 95
B.5 HaloTag 95
B.6 HaloTag with a known target protein 96
B.7 Interaction of α-actinin 2 with the neck region 98
B.8 ybbR tag 99
B.9 Summary 101
C MATERIAL AND METHODS 103
C.1 Cloning and Expression 103
C.2 Experimental protocol 104

c.3 Sequences for the α-actinin/titin interaction 104
c.4 Sequences for the talin/integrin interaction 106
c.5 Protocol for HaloTag conjugation 106
c.6 Protocol for ybbR conjugation 108

ACRONYMS

AFM	Atomic force microscopy
AOD	Acousto-optic deflector
CoA	Coenzyme A
CL	Contour length
DMSO	Dimethyl sulfoxide
ECM	Extracellular matrix
EtOH	Ethanol
eWLC	Estensible worm-like chain
FRET	Förster resonance energy transfer
HMM	Hidden Markov model
IPTG	Isopropyl β-D-1-thiogalactopyranoside
MD	Membrane distal
MP	Membrane proximal
NA	Numerical aperture
NMR	Nuclear magnetic resonance
SFMS	Single-molecule force spectroscopy
Sfp	Sfp phosphopantetheinyl transferase
TCEP	Tris(2-carboxyethyl)phosphine
WLC	Worm-like chain

1

INTRODUCTION

All eukaryotic cells are equipped with a network of filamentous proteins, called *the cytoskeleton*. It maintains cell shape, provides routes for internal trafficking and rapidly responds to extracellular mechanical stimuli. This intracellular scaffold is formed by three protein filaments, actin filaments, microtubules and intermediate filaments [94].

The cytoskeleton's structure and function can vary with species and tissue. Myocytes, i.e. muscle cells, are dominated by actin filaments, that are spatially organised with a symmetry absent in all other cell types [132]. In particular, cells from striated muscle, a category comprising the voluntary skeletal muscle and the involuntary cardiac muscle, retain a semi-crystalline organisation of the cytoskeleton, which is essential to performing the task of converting chemical energy into highly directed mechanical forces.

The hierarchical and pattern-like structure of striated muscle tissues is also evident in the organisation of their smaller components. The cardiac myocyte shown in Fig. 1A is composed of repeated small contractile units, called sarcomeres, which in turn are formed from directed and precisely interdigitated cytoskeletal filaments (Fig. 1B).

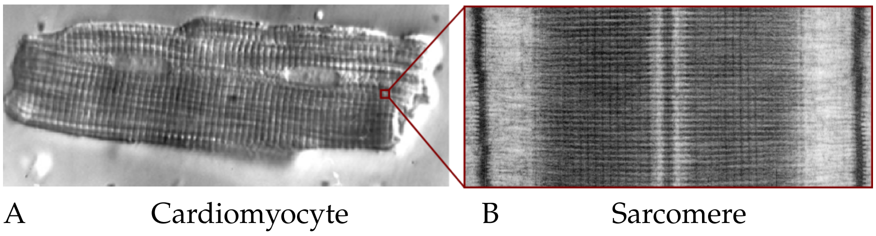

Fig. 1. Regularity of muscle cells. Electron micrographs of a cardiac muscle cell (A), and of a single sarcomere (B). The precise spatio-temporal control of the bonds involved in muscle assembly and maintenance results in the observed semi-crystalline organisation of the sarcomere. From [74].

Despite its astonishing regularity, the sarcomere is not a static structure. The rigidity required upon contraction is in fact combined with a fine-tuned elasticity under stretching conditions. To fulfil these different requirements, the sarcomere is composed of a large number of specialised proteins. For instance, the molecular motor myosin generates the force to contract the sarcomere, while the elastic spring titin provides the stiffness to restore the resting length after elongation [34]. The stable connectivity between the single components is indispensable for correctly transmitting forces along the muscle: The contraction of the whole muscular tissue, both that which initiates voluntary movements (skeletal muscle) or that which pumps blood through the circulatory system (cardiac muscle), is possible due to the tight connection between adjacent sarcomeres. Likewise, body locomotion relies on the strong linkage between muscles and bones, which is mediated by tendons. How the sarcomere is assembled with such precision, how it retains its structure regardless repetitive high stresses and how it achieves structural adaptability, are still widely unexplored questions [46]. A comprehensive understanding of the molecular interactions may help to unveil the mechanical properties of the muscle tissue, since even a single point mutation within a protein can lead to severe myopathies such as heart failure or muscular dystrophies [2, 19].

TWO IMPORTANT PROTEIN/PROTEIN INTERACTIONS

This work examines the mechanical properties of interactions between myocyte-specific proteins.[1] The first interaction investigated involves α-actinin and titin, two proteins that interact at the edge of each sarcomere, and have been proposed to maintain sarcomere cohesion upon muscle stretching [34]. The second bond is formed by talin and integrin, which mediate lateral adhesion of parallel myocytes and connect them to tendon cells at the myotendinous junction [4, 82], as shown in Fig. 2.

The affinities of the α-actinin/titin and talin/integrin interactions, despite their important role, have been reported to be comparatively low (in the micromolar range) [4, 56], which points to a low mechanical stability. This raises the question of which molecular mechanism leads to long-term cell cohesion and adhesion.

No comprehensive studies have been performed so far on the forces at which these bonds break apart, nor on the force dependence of the bond lifetimes. The measurement of such quantities relies on the ability to apply and record a controlled load on the bond, which cannot be done in bulk experiments. To this end, single-molecule force-spectroscopy (SMFS) techniques have emerged in recent times as powerful tools to manipulate isolated components of various biological systems. Among the available SMFS methods, *optical tweezers* have been employed in this work, because of the expected low forces (on the order of piconewtons) involved in the protein/protein interactions studied [60, 99].

---

[1] The proteins studied in this thesis are either specific to muscle tissue, such as α-actinin 2 or titin, or are ubiquitous but have specific isoforms expressed in muscle cells, such as integrin β1D and talin 2.

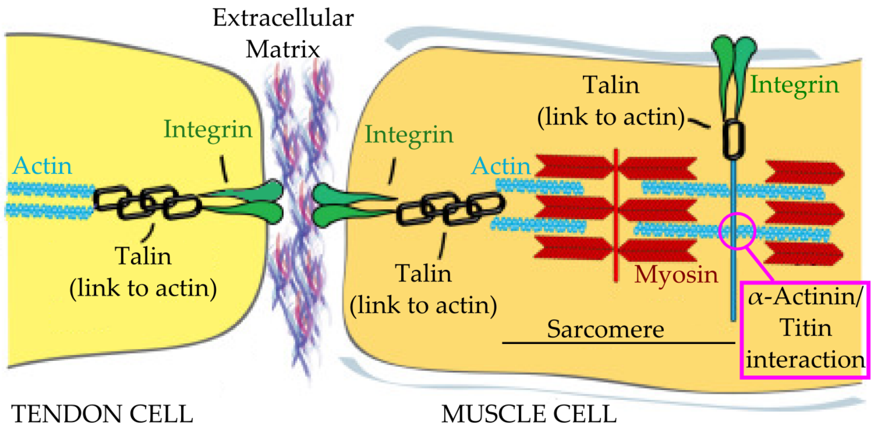

Fig. 2. Myotendinous junction. A tendon cell (on the left) is connected to a muscle cell (right). Talin connects the actin filaments to the extracellular matrix through the interaction with the transmembrane protein integrin. Longitudinal anchoring with tendon cells, as well as the lateral connection between parallel myocytes, are mediated by integrin. The actomyosin organisation within a sarcomere is depicted in the muscle cell, and the location of the α-actinin/titin bond is marked in pink. Adapted from [77].

OUTLINE

This thesis is separated into three parts. A general introduction to the techniques and methods employed is the topic of Part I. Chapter 2 deals with the use of optical tweezers for the application of forces on molecular systems, with a particular focus on protein/protein interactions and on the specifications of the employed experimental setup. The background theoretical framework and the methods for data analysis are discussed in chapter 3.

The next two parts discuss the investigation of the two aforementioned protein/protein interactions. Part II deals with the mechanical stability of the α-actinin/titin interaction. The open questions regarding sarcomere integrity upon muscle stretching are introduced in chapter 4. α-Actinin binds titin in a region formed by up to seven peptide motifs, called *Z-repeats*. Measurements of the interaction between α-actinin and the Z-repeat 7, for which structural data are available, are described in chapter 5. Binding of α-actinin to other Z-repeats was investigated in chapter 6, and a model proposed to account for the concerted action of these multiple interactions in keeping the muscle compact in the presence of stretching forces.

Part III sets the scene for the mechanical study of the talin/integrin interaction. Chapter 7 comprises an introduction to force transduction across the cell membrane—mediated by integrins—which is fundamental to the load propagation from muscles to tendons. This interaction is not muscle-specific, but is involved in many other cellular processes. The mechanical response of the talin/integrin bond under force is studied and presented in chapter 8. In chapter 9, a method for evaluating the competition between different integrin binding partners is presented, and the outlook for future work is given.

Part I

EXPERIMENTAL APPROACH AND METHODS

2

SINGLE MOLECULE FORCE SPECTROSCOPY USING OPTICAL TWEEZERS

The scope of this chapter is to present the methods used in this thesis. To exert loads on isolated molecules, some techniques that can be grouped under the term *single-molecule force spectroscopy* (SMFS) can be used. An introduction to this field is given in Sec. 2.1. Among the possible applications of SMFS techniques, the study of protein/protein interaction mechanics will be discussed in more detail (2.2), being the main topic of this work. The technique applied in the work presented in this thesis, the *optical tweezers*, is further described (2.3), with a focus on the setup utilised (2.4). The last two sections deal with sample preparation (2.5) and measurement protocols (2.6).

2.1 SINGLE-MOLECULE FORCE SPECTROSCOPY

In ensemble measurements, large numbers of molecules are simultaneously monitored, and the average behaviour evaluated, whereas single-molecule experiments enable the observation of the properties of individual components. The ability to measure single molecules has enabled the measurement of the kinetics of processes which are difficult to observe in bulk experiments [21]. The step-wise activity of enzymes [87], the motion of molecular motors [49] and the unfolding behaviours of proteins [98] are some remarkable examples.

Single-molecule force spectroscopy (SMFS) techniques allow the direct mechanical manipulation of isolated biomolecules. This is of particular interest since a range of cellular processes are driven and regulated by mechanical forces. The most common techniques for force application and detection at the single-molecule level are atomic force microscopy (AFM), optical twezeers and magnetic tweezers (reviewed in

[88]). Moreover, a number of manipulation techniques have been recently developed, from acoustic force spectroscopy [105] to DNA-based methods [30, 90]. The following sections deal with the technique used in this work, optical tweezers (OT), in particular their application for the study of protein/protein interactions. OT are particularly suited to the application of low forces—below 60 pN—with a distance resolution in the nanometer range and a force resolution in the sub-pN range.

2.2 PROTEIN/PROTEIN INTERACTION MECHANICS

To study the mechanical properties of the bond between two proteins with SMFS techniques, it is crucial to measure a sample where the two molecules—e. g. a receptor A and a ligand B—are bound in a complex. A possible strategy is to let the two components react in solution and to isolate the complex fraction by size exclusion chromatography [15, 32, 55].

If the unbinding and rebinding kinetics of the proteins A and B are to be investigated, it is necessary to link them in a site other than the one under study, in order to keep the molecules in close proximity even after mechanically-induced rupture of the interaction (Fig. 3). If the only connection between the molecules is the interaction under investigation, breaking this bond leads to the loss of the construct.

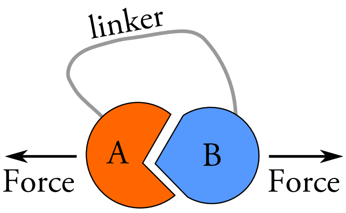

Fig. 3. Schematic of a fusion construct for SMFS measurements. The proteins A and B are expressed together, with a linker connecting the C-terminus of one protein with the N-terminus of the second one. Two pulling positions are chosen, one on each protein, in order to mechanically separate them.

A versatile method to connect small proteins, employed in this work, involves the creation of fusion contructs, namely a single protein chain where A and B are fused together by a linker (Fig. 3) [60, 99, 136]. The linker must be long enough to allow the binding sites of the two molecules to interact with each other. Moreover, it must have a "neutral" sequence, i.e., one that is unlikely to affect the measurments (often a combination of glycine and serine).

2.3 OPTICAL TWEEZERS PRINCIPLES

Over the last three decades, optical tweezers have emerged as an important method for the application of forces to biological samples. While at first entire cells and viruses were trapped [7, 8], soon the capability of this technique was extended to the study of single molecules linked to micro-sized beads. Pioneering experiments ranged from the manipulation of RNA polymerase [125] to molecular motors [16, 27] and DNA [107, 124].

Optical tweezers rely on the interaction between matter and light, in particular on the ability of a highly focussed laser beam to trap dielectric objects. An extensive theory of this phenomenon is not yet completed, even though analytical solutions have been obtained for different regimes and approximations [89]. A qualitative understanding of optical tweezers principles can be achieved in terms of geometric ray optics. Let us consider a spherical bead of diameter d in the path of a standard laser beam with a Gaussian power distribution, of wavelength λ. An optic ray description holds in the regime (called *Mie regime*) where the bead size is significantly larger than the wavelength of the light field ($\lambda \ll d$). If the laser is focussed with a high numerical aperture (NA) lens, it can be shown that stable trapping can be achieved. The only requirement is that the refractive index of the bead is higher than that of the surrounding medium (Fig. 4 and Box 1).[1]

It is possible to trap dielectric particles also in other regimes ($\lambda \gtrsim d$), but the treatment is more complex, and analytical solutions are not always possible [89, 114, 120].

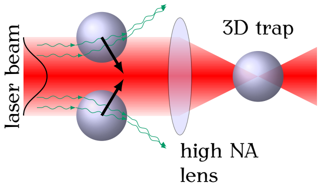

FIG. 4. Optical trapping principles. Photons (green) of a Gaussian laser beam are refracted by the beads. Due to the intensity gradient, more photons are scattered out from the center, thus the net force *on the beads* (black arrows) is directed towards the beam center. Note that part of the photons is also reflected, pushing the bead even more in the beam propagation direction. To obtain a stable 3D trap (right hand), an intensity gradient has to be created also in the third direction. High-NA lenses like objectives can be employed to this end.

BOX 1. TRAPPING BEADS IN THE MIE REGIME

Fig. 4 shows that, in case of displacement of the beads from the center of the laser beam, the scattered light results in a restoring force towards the intensity maximum (left hand side). Photons carry momentum and are refracted from the beads, changing their direction. Hence, equal and opposite forces are applied by photons to the beads. The Gaussian profile causes more photons to be deviated far from the beam center, leading to a net force on the bead *towards* the center. In addition, the beam will push the beads in the direction of light propagation (this effect is amplified by the photons reflected by the beads), along its central axis. To create a three-dimensional stable trap, an intensity gradient has to be created also in the propagation direction, for example using a lens with high numerical aperture such as an objective.

In the plane perpendicular to the propagation direction, the trapping potential can be considered Gaussian. This implies that for small displacements the potential can be approximated with a parabola. The restoring force is thus linear, i.e. the trap is an Hookean spring (Fig. 5).

---

[1] In this regime, the sphere does not need to be dielectric.

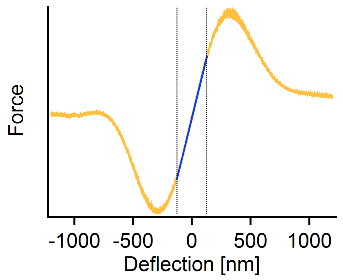

Fig. 5. Restoring force applied on a 1 µm silica bead by a 1064 nm-wavelength laser beam, as a function of deflection, namely the distance between the bead and the trap center. The restoring force has a linear dependency around the center, as shown by the fitting line in blue. The linear dependency comes from the fact that the Gaussian potential can be approximated with a parabola around the center (in this case within ±120 nm), thus in that range the trap behaves as an Hookean spring.

The basic elements of an optical tweezers setup can be summarised as follows, while more details on the instrument employed in this work are given in the next section:

LASER To create the optical trap. The laser typically has a Gaussian intensity profile (TEM00) to increase the lateral gradient, is infrared to reduce photodamage of the samples and is fiber-coupled to reduce pointing deviations.

STEERING DEVICES To move the trap position and modulate the force applied to the molecule. The laser can be mechanically steered by piezo mirrors or deflected using crystals (acousto-optic deflectors).

HIGH NUMERICAL APERTURE LENS To obtain the high 3D intensity gradient needed to trap the beads. Oil-immersion objectives can have a numerical aperture up to 1.45, while water-immersion objective with high NA (1.27) are also available.

DETECTION DEVICES To read out the position of the beads with respect to the laser (termed *deflection*, Fig. 6), thus measuring the forces applied to the molecules. Light-sensitive photodiodes are commonly used, and back-focal-plane detection employed in order to record the relative distance between the trap center and the bead center.

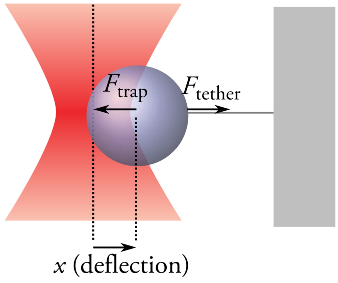

Fig. 6. Schematic of force measurements. The deflection x is measured as the distance between the bead and the trap centers. If a molecule is tethered to the bead and the trap is displaced, the bead is at equilibrium between the force applied by the molecule F_{tether} and the restoring force of the optical trap $F_{\text{trap}} = k_T x$, proportional to the deflection and the trap stiffness k_T.

2.4 EXPERIMENTAL SETUP

The experiments were carried out on a dual-beam optical tweezers setup recently built by Ulrich Merkel. The laser beam is split by polarisation into two paths that form two distinct optical traps in the sample plane. The deflection is recorded using position sentitive devices (PSD) in back-focal-plane detection. In the linear range of the trap (Fig. 5), force is proportional to deflection. The spring constant (stiffness) of each trap, k_T, is calibrated using a method explained in [121], with resulting stiffnesses between 0.15 and 0.25 pN/nm. The error in the trap stiffness, and thus in the measured force, is about 10 %. Data were acquired at a frequency of 150 kHz, averaged and recorded at 30 kHz. The deflection signals of the two traps were first corrected for crosstalk [9], then sumed up to increase the signal-to-noise ratio, and finally multiplied for the effective trap stiffness $k_{\mathrm{eff}} = (k_{\mathrm{T}_1}^{-1} + k_{\mathrm{T}_2}^{-1})^{-1}$ (springs in series).

The design details are almost identical to those described in [47], with the main difference being the ability to steer both traps,[2] one with a two-axis piezoelectric mirror tip/tilt actuator ("piezo mirror", Mad City Labs), the other with acousto-optic deflectors ("AODs", AA Opto Electronic). The AODs are very fast devices, with a response time shorter than 10 µs, making them particularly suitable for rapidly changing the trap position (Fig. 7). AODs deflect light by making use of the interaction between the laser beam and a sound wave travelling through a crystal (more details in Box 2). The transmittance of the crystal slightly depends on the deflecting angle (thus on the trap position), which makes this device unsuitable for the application of force ramps. By contrast, piezo mirrors deflect the laser beam without affecting the transmittance, but the response time is on the order of 1 ms. Hence, they are appropriate for smoothly changing trap position (e. g. for application of force-ramps, Fig. 7), but are not reliable for very rapidly jumping between different positions.

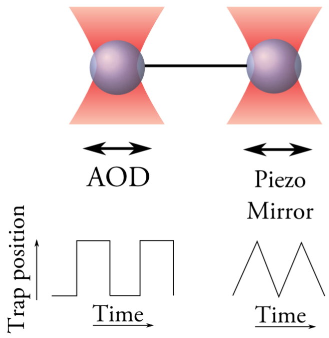

Fig. 7. Dual beam optical tweezers with two steerable traps and a sample connected to both beads. The right trap, controlled by a piezo mirror, is used to apply "slow" loads, such as force ramps. The left trap, controlled by AODs, is moved only when a rapid force change is required.

BOX 2. AOD OPERATION PRINCIPLES

An AOD is formed by a crystal through which a travelling sound wave is sent by a digitally-controlled piezo element. The pressure wave propagates through the crystal in a direction perpendicular to the laser beam, acting as a grid that deflects the incoming light (a more detailed description of AOD principles involves quantum photon/phonon interaction and will not be given here). This device permits rapid movements (∼10 µs) of the trap position by tuning the wavelength of the sound wave. The major drawback is that the transmittance varies with respect of the wavelenght of the sound wave, affecting the force signal. A correction is thus necessary for the analysis of force ramps performed with AODs [111].

The kinetic and mechanical properties of the proteins under investigation were assessed using a number of assays (force ramps and jumps have already been mentioned), which will be the topic of the next section.

---

[2] The double-streerable-beam approach has been designed in order to improve the quality of confocal-fluorescence experiments combined with optical tweezers, since a single mobile trap would displace the protein out of the confocal volume of the exitacion laser. By moving both traps at the same time, the protein can be kept at a fixed position with respect of the sample chamber and the fluorescent laser. The other additional advantage is that the piezo mirror and the AODs can be used for different assay, as explained in the text.

2.5 DUMBBELL ASSAY FORMATION

To be able to apply forces on a protein construct using dual-beam optical tweezers, the protein has to be coupled to the micronsized beads that are trapped in the laser foci (Fig. 8). The main steps of the experiment are summarised below (more details in appendix C):

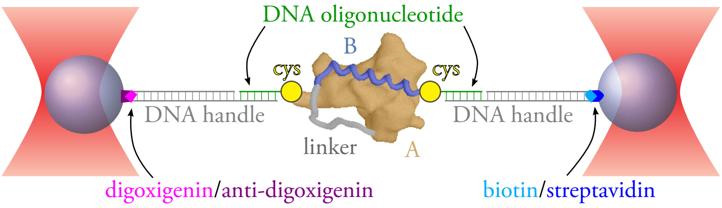

Fig. 8. Schematic of the dumbbell assay employed to apply and measure an external load to single proteins. A fusion construct, where proteins A and B are fused together via a linker, is bound to maleimide-modified oligonucleotides by means of terminal cysteines. The oligonucleotides are coupled to DNA handles with different terminal modifications (digoxigenin or biotin), which in turn bind functionalized (with anti-digoxigenin or streptavidin) beads.

PROTEIN EXPRESSION AND PURIFICATION The first step is the preparation of the protein sample. All proteins in this work were expressed in *E. coli* by means of standard recombinant DNA techniques. The proteins were mutated in order to carry only two cysteine residues in the positions were the force application was necessary. To avoid unwanted conjugation, all internal cysteines have been mutated.

ATTACHMENT OF SHORT OLIGONUCLEOTIDES The purified protein was incubated with short maleimide-modified oligonucleotides termed *oligos* in the remainder of the text (34 bp) to form covalent bonds with the cysteines.[3] This sample was then purified using a size exclusion column to select the fraction containing proteins with two bound oligos, that were aliquoted and shock frozen. The next steps can be performed within a day, after defrosting the sample.

DUMBBELL PREPARATION The protein reacted with oligos was further incubated with long dsDNA molecules called *handles*. At one end, a single stranded overhang complementary to the oligo sequence is present, allowing hybridisation. At the other end, the handles carry a modification, allowing coupling with 1 µm functionalized silica beads. Half of the molecules were biotin modified while the other half were digoxigenin modified. After incubation of the protein-oligo-handles reaction with streptavidin-coated beads, a final reaction was prepared with addition of anti-digoxigenin-coated beads. Since silica beads release free oxygen radicals when irradiated by the laser, a scavenger system was added to this mixture, to avoid damage to the protein.

---

[3] Appendix B deals with other methods for protein-oligo coupling, as alternatives to cysteine modification.

TRAPPING One bead of each type was trapped in a dual-beam optical tweezers setup, and the dumbbell formed by bringing them in close proximity. The two bead types can be distinguished because the anti-digoxigenin beads are fluorescently labelled.

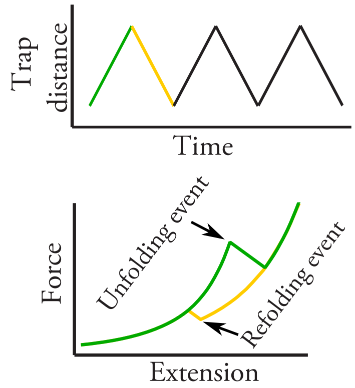

Fig. 9. Force ramps. One trap is moved at a constant velocity with a triangular function (above). The force vs. extension graph (below) shows protein unfolding/refolding events, associated with both a change in force and extension (see Fig. 10).

2.6 EXPERIMENTAL ASSAYS

The ability to obtain a proper description of the binding kinetics of a certain interaction, as well as the folding properties of a protein domain, depends on the precise control of the applied force. A number of measurement protocols are presented, that cover a wide spectrum of solutions for the obstacles encountered while investigating kinetic networks.

The observation of single domain transitions between the folded (native) and unfolded states will be used as a prototype to explain the assays. If two proteins A and B are linked together, as introduced in Sec. 2.2, the same protocols can be used to study the binding/unbinding kinetics, since the breakage of the bond can be treated in the same way as an unfolding event.

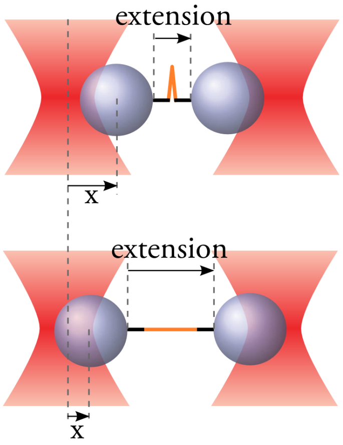

Fig. 10. A protein (orange) betweeen two DNA handles (black) is unfolded in dual-beam optical tweezers. Upon unfolding, the extension of the tether increases, the bead deflection x decreases, and so does the measured force. Note that bead movements are exaggerated, for clarity. In the employed setup, beads never move more than ~10 % of their radii (Fig. 5). Some graphs are plotted vs. the *trap distance*, defined as the distance between the laser foci minus the sum of the beads radii.

FORCE RAMP The basic force-spectroscopy assay consists in the application of load using repeated cycles at constant speed (Fig. 9), obtained by moving one laser beam with a triangular wave while keeping the other trap fixed. In this way the molecule is stretched with increasing forces and the experimenter can locate the force range of the unfolding events. The data are typically displayed as the force on the beads measured as a function of the tether extension. The unfolding of a protein domain leads to a relaxation (decrease of the force signal) together with an elongation (increase of the extension), as illustrated in Fig. 10. Hence, the force/extension trace is a fingerprint of the molecule under study. Moreover, the assay allows protein refolding in the descending part of the cycle, where the force is continuously decreased, usually down to zero load.

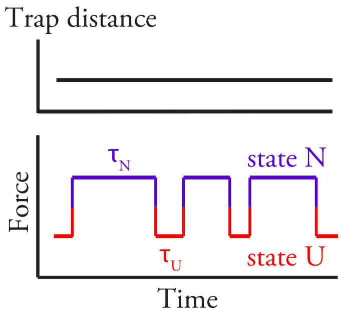

Fig. 11. Passive mode. The distance between the traps is kept constant and the force value recorded over time. Unfolding events are visualised as sudden drops in the force signal, as shown in the lower graph. The data are sorted into native (N) and unfolded (U) states, and the lifetime of each dwell event (τ_N or τ_U) measured.

PASSIVE MODE Although all energetic and kinetic parameters of the system can be extracted by repetitively stretching and relaxing the molecule, it is easier to explore the energy landscape at equilibrium, performing passive-mode experiments. In this case, the two traps are kept at a fixed distance, and the system is able to explore different conformations *at equilibrium*. The force is recorded at a fixed sample rate for a certain time, as shown in Fig. 11. In analogy with force-ramp traces, an unfolding event is associated with a drop in the force signal. If the state transitions are fast enough,[4] this method allows the collection of several folding/unfolding events at the same force level, from which the average lifetime can be extracted. This can be useful for studying the system kinetics at forces of physiological relevance, or, if a number of traces at different pre-tensions are recorded, to precisely track the force dependence of the transition rates.

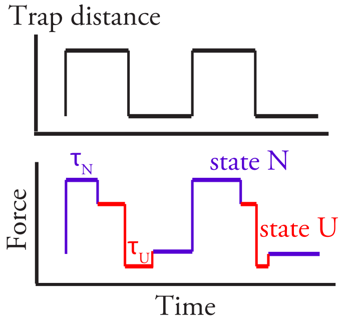

Fig. 12. Jump assay. The trap distance is varied between two positions. Refolding is more likely to take place at the low force level, unfolding at the high one. The high level allows extraction of unfolding rate (from τ_N), the low level of refolding rates (from τ_U).

JUMP ASSAY When slow kinetics are involved,[5] it may require a long time to collect a statistically relevant amount of data at equilibrium. For instance, at high pre-loads, refolding events become more and more rare. In such cases, it is possible to relax the system by keeping it at low force, thus favoring refolding, and then to jump up to high forces to observe the unfolding. (Fig. 12). An elegant approach towards achieving such an effect is the *jump assay*, where the trap distance is abruptly changed from low to high force conditions. For this purpose, it is fundamental to change the trap position—namely the pre-load—as fast as possible, in order to “freeze” the system while moving from one force level to the other. Using the jump assay, the unfolding kinetics can be assessed at high forces, the refolding kinetics at low forces. In the first application of this method [100] the jump frequency was adjusted manually, i. e. the force level was changed after the folding/unfolding event was observed (Fig. 12). A more efficient and automated way of collecting jump data is to rapidly switch between the two positions and later merge together the data obtained in the high force level to extract the unfolding transition, as well as those from the low force level to evaluate refolding kinetics.[6]

---

[4] The stability of a dual-beam optical trap allows the observation of the same molecule for as long as an hour. Folding/unfolding events with slow kinetics, e. g. in the order of a minute, can still be monitored.

[5] This can be due for a example to a high energy barrier between the folded and the unfolded states. An extensive description of state transitions based on energy landscapes will be given in the next chapter.

COMPETITION ASSAY In the protein/protein interaction studies presented in Sec. 2.2, linked molecules allow the combined study of unbinding and rebinding kinetics. The limit of such a system lies in the fact that the rebinding kinetics depend on the linker length, which determines the *effective concentration* of the ligand B. Namely, the longer the linker, the slower the binding. A precise estimation of the on-rates, thus of the affinity, relies on the determination of the effective concentration, which is difficult to obtain based on pure geometrical considerations.

To overcome this limitation, an approach similar to that presented in [99] was employed, where the same tethered ligand was also added in solution. A competition between the fused and the free ligands is established, and the concentration-dependent on-rates can be precisely estimated, due to the known concentration of the solution ligand. The binding of the solution ligand B can occur only while the fused proteins A and B are transiently detached, thus it can be observed at the same force level as that of the unbound state (Fig. 13). In order to distinguish such events from the unbound states, different time scales have to be involved. Namely, the lifetimes of the unbound dwells must shorter than the solution-bound ones. The latter are force-independent, because the solution ligand is not under load, while the former are load-dependent. Hence, the competition assay has to be performed in a force range where the rebinding kinetics (red dwells, Fig. 13) are significantly faster than the zero-force unbinding kinetics (cyan dwells).

The competition assay is a method to observe force-free binding and unbinding, using the original fusion construct as a binding detector. Therefore, it can be

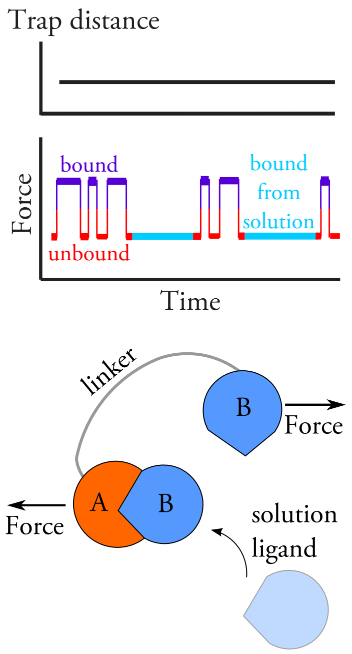

FIG. 13. Competition assay. In a passive-mode trace, the binding/unbinding of the tethered ligand B is observed in competition with a free ligand in solution (above). When the tethered ligand is unbound, the one in solution has the possibility to bind the substrate A, as shown by the cyan events, corresponding to the state depicted in the lower schematic. At the right conditions, i.e. by tuning the preload and concentration of the ligand in solution, the binding from solution (cyan dwells) can be separated from the unbound state (red dwells).

---

[6] This approach is valid if the refolding is negligible at the high force level, and the unfolding negligible at the low force level. This hypothesis can be checked *a posteriori*, as explained in details in Sec. 3.5.

extended to the study of different ligands (other than B) that bind the same substrate A.

3

THEORY AND DATA ANALYSIS

This chapter sets the scene for the analysis procedures, together with the underlying theoretical background. The description loosely follows the four experimental assays of Sec. 2.6, where an introduction to present the purposes and features of each assay was given. The first section (3.1) deals with the framework of energy landscapes, a common view for protein folding interpretation. Afterwards, the analysis of force ramps (3.2), passive-mode traces (3.3), jump (3.4) and competition (3.5) experiments is described.

3.1 ENERGY LANDSCAPE THEORY

To illustrate the folding properties of a protein, the free-energy landscape is a widely accepted concept, since it offers both a visual as well as a quantitative approach to the folding problem [24, 72]. Each point on such a map is a possible three-dimensional conformation of the molecule. In this model, the search for the native (folded) conformation takes place by minimisation of the free energy, as illustrated by the simplest two-state funnel potential of Fig. 14A. A more realistic landscape is the rugged potential depicted in Fig. 14B, where the native state can be reached from different directions, after visiting local minima that correspond to partly folded (although not native) conformations.

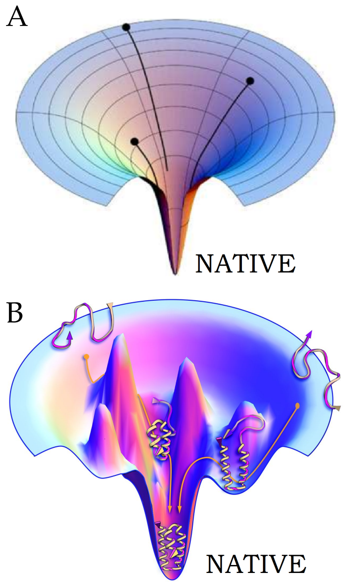

Fig. 14. Funnel theory of protein folding. The energy of each conformation (vertical axis) is plotted vs. the conformation (horizontal plane). Since the the molecule has three-dimensional conformations, four dimensions would be necessary for this plot. The native conformation corresponds to a minimum in the free-energy landscape. (A) Idealised smooth potential of a basic two-state system. (B) Rugged potential, including traps and barriers. Misfolded transitory conformations can be explored in the folding process (local minima), and the native state can be reached by different pathways. Adapted from [72] and [22].

If the protein is constrained in the dual-beam optical tweezers assay described in the previous chapter, it is useful to project the two-state energy landscape of Fig. 14A along a certain reaction coordinate,[1] as shown in Fig. 15. The application of an external force in the reaction coordinate direction yields an additional potential $U = -Fx$, that substantially tilts the landscape [14, 25]. Therefore, the height of the energy barrier varies with force, thus affecting the average time the system needs to overcome the barrier, known as *first-passage time*.

---

[1] In force-spectroscopy experiments, the pulling direction is an intuitive choice for such a coordinate.

This interpretation will be applied throughout this chapter in order to describe the mechanical and kinetic parameters of the system. It is important to note that the theoretical toolkit presented for the analysis of folding/unfolding transitions (N↔U) can also be employed for binding/unbinding of two proteins fused together (A+B↔AB) [76].

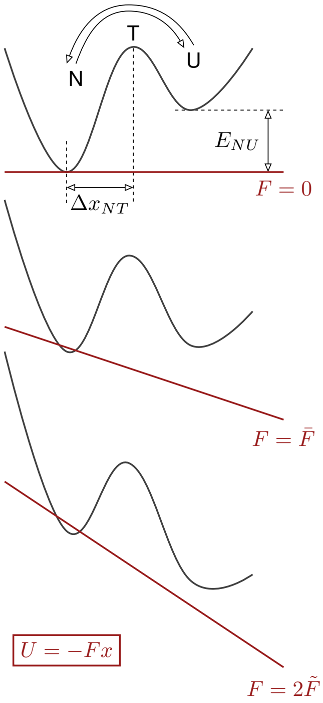

Fig. 15. Energy landscape of the protein folding process. Force-induced tilting of a two-state system projected in one dimension. Native (N) and unfolded (U) conformations are separated by an energy barrier, where the transition state (T) is located. The external potential associated with a constant applied force is shown in red.

3.2 FORCE-RAMP ANALYSIS

The force data recorded during force ramps are displayed as a function of the tether extension (Fig. 10). The stretching and relaxation cycles can overlap or show hysteresis (the latter case in Fig. 17), depending on the pulling speed and the energy landscape.[2] The shape of the force vs. extension curve of elastic polymers such as DNA and proteins can be properly described using *Worm-Like Chain* models (WLC). The system under study is a chain of DNA and protein molecules placed in series.

Let us now consider the stretching cycle in Fig. 17 as an example. At low forces, when the protein is still folded, the shape of the curve is dominated by the DNA mechanics, which can be approximated by the *extensible Worm-Like Chain* model (eWLC) [124]. Beside the typical WLC properties of the polymer, namely the persistence length L_{DNA} and the contour length P_{DNA} (Box 3), the model includes a residual linear term with stretch modulus K.

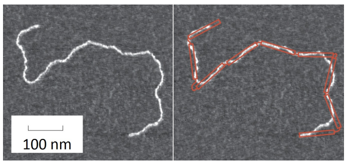

Fig. 16. Separation of a DNA molecule in stiff rods, as stated by the *freely-jointed chain model*. Adapted from [94].

BOX 3. WLC MODEL

Polymers such as nucleid acids and unfolded proteins, can be described in the simplest model as a chain of stiff rods that can rotate against each other—Freely jointed chain—as shown in Fig. 16. A more appropriate description is given by WLC model, where a chain of length L (contour length) is a single rod bent by thermal energy in a continuous manner, as is the case for flexible materials. The persistence length p is the minimal distance between uncorrelated points.

---

[2] For instance, a higher energy barrier will require a higher force to unfold the protein, i.e. more tilting of the energy landscape. For the same reason, refolding will take place at lower forces upon relaxation.

A number of functions have been derived to approximate DNA elasticity, described in [124]. In this thesis, force/extension data before any unfolding occurrence (black dotted line in Fig. 17) are fitted using:

$$F_{\text{eWLC}}(x) = \frac{k_B T}{p_{\text{DNA}}}\left(\frac{1}{4}\left(1-\frac{x}{L_{\text{DNA}}}+\frac{F}{K}\right)^{-2}-\frac{1}{4}+\frac{x}{L_{\text{DNA}}}-\frac{F}{K}\right). \qquad (1)$$

After an unfolding event occurs, the shape of the curve is a combination of the stretching behaviour of the DNA and the unfolded region of the protein. An unfolded peptide chain follows a standard WLC model [80, 98], where the protein contour length L_{prot} and the persistence length p_{prot} are the only parameters:

$$F_{\text{WLC}}(x) = \frac{k_B T}{p_{\text{prot}}}\left(\frac{1}{4}\left(1-\frac{x}{L_{\text{prot}}}\right)^{-2}-\frac{1}{4}+\frac{x}{L_{\text{prot}}}\right). \qquad (2)$$

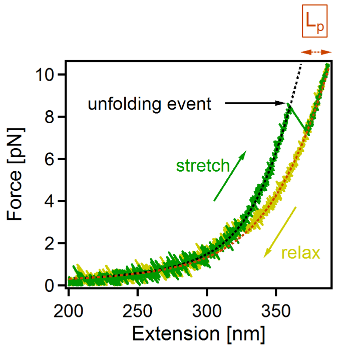

Fig. 17. Example of force/extension graph for a single stretch (green) and relax (yellow) cycle. An unfolding event is marked by an arrow. The fits are obtained according to Eqs. 1 and 2 (see text). L_p is the protein contour length, given by the red fit if the DNA parameters have been already computed from the black fit.

The force/extension curve after protein unfolding is fitted (red curve in Fig. 17) with a combination of Eqs. 1 and 2. Since DNA and protein are in series, they feel the same force. The two equations are thus inverted in $x(F)$ and the sum of the two contributions is used to fit the inverted extension/force plot. In this thesis, p_{prot} is kept fixed at 0.7 nm. Hence, the red fit in Fig. 17 has the contour length of the protein L_{prot} as the only free parameter, since the DNA parameters have already been computed in the first fit. This observation is especially important if the data are subsequently transformed in contour length space (Box 4).

BOX 4. CONTOUR LENGTH (CL) TRANSFORMATION

In a constant-velocity trace, such as that depicted in Fig. 17, it is possible to fit the curve before any protein unfolding has occurred, allowing the extraction of the DNA mechanical parameters. Starting from this fit, the graph can be transformed in contour length space. In practice, the transformation is equivalent to the fit (red curve) obtained by combining Eqs. 1 and 2 (see discussion in the text). Since L_p is the only free fitting parameter, the force value of each point can be converted to contour length. The CL transformation of Fig. 17 is shown in Fig. 18.

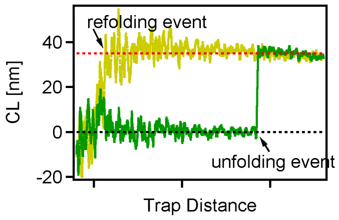

Fig. 18. Contour length transformation of data in Fig. 17. All data following the black fit shown in Fig. 17 are now aligned at zero CL gain. After the unfolding event, the CL increases by a length L_p (the red fit in Fig. 17). In this plot, a refolding event is also visible and marked by an arrow. The CL data are plotted against the trap distance.

Repeated constant-velocity traces make the extraction of the kinetic and energetic constants possible, e. g. using the *Oberbarnscheidt method* [91] or *Crooks' fluctuation theorem* [20]. An alternative way to explore the kinetics is to perform a series of equilibrium experiments, as explained in the next section.

3.3 PASSIVE-MODE ASSAY

Dual-beam optical traps have a high thermal and mechanical stability. Hence, they allow experiments where the distance between the two laser foci is kept fixed over time, and the force monitored, to be performed. The system can explore the energy landscape at different pre-tensions, and unfolding/unbinding events can be detected if a length change is involved.

Let us again consider for simplicity a two-state system, for example a protein that experiences transitions between the folded (native) and the unfolded state, monitored by a single variable, in this case, force (Fig. 19A).

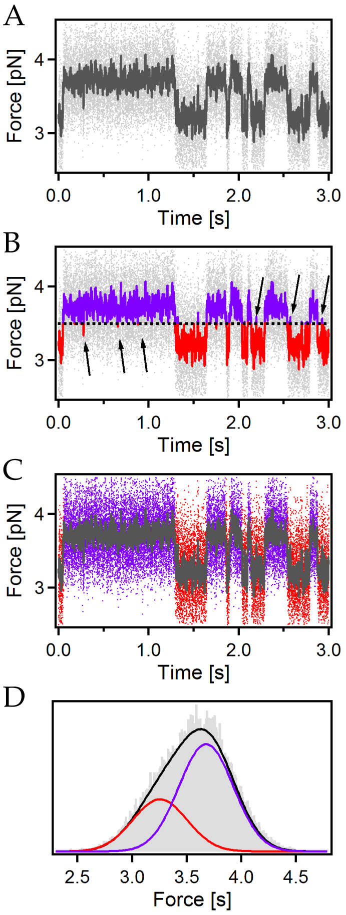

Fig. 19. Data sorting in two states. (A) Raw data (grey) and smoothed trace (black). (B) Sorting of smoothed data by threshold. Arrows mark misassigned events. (C) HMM analysis on raw data. (D) Force distribution of the trace. Double-gaussian fits (purple and red) and sum curve (black).

HIDDEN MARKOV MODEL The first step towards a characterisation of the force-dependent kinetics is the sorting of the raw data into different states . An intuitive way to sort data in two states is to smooth the trace and set a force threshold above which the points are associated with the native state (Fig. 19B). If the raw data heavily overlap as shown in the histogram in Fig. 19D, a high filtering degree is required, to avoid the possibility of incorrectly assigning events, for example those marked by arrows in Fig. 19B. On the other hand, a high filtering leads to a decrease in the temporal resolution, resulting in the loss of short events or possible intermediate states.

A more sophisticated approach to assign states to raw data is the use of *Hidden Markov Models* (HMM) [110]. These methods are based on the hypothesis that the trajectory of a protein through the network of possible states is Markovian, namely a memoryless process.[3] Since recorded data are limited to a certain sampling rate, the discrete-time theory has to be applied. The basic argument is that, between two subsequent observations, the system has a constant probability (first-order decay) of staying in the current state or transitioning into another one (Fig. 20).

The analysis is performed by fixing the number of states and the permitted connections between them. The other prerequisites, adjustable by an iterative process, are the *emission probabilities*—the force distributions of Fig. 19D—and the *transition probabilities* between the states between two subsequent points (called T_{ij} in Fig. 20). The algorithm is based on the calculation of the probability p_{forward} that the system is in state i at time t, considering the trajectory (force values) of all points from 0 to t and *given* the emission and transition probabilities. The analogous probability p_{backward} can be calculated by reverting the time axis,[4] starting from the last point of the time trace and moving backwards. The probabilites p_{forward} and p_{backward} can be multiplied (forward-backward algorithm) in order to assign to each data point the most probable state (more details in [110]).

---

[3] The beads' motion equation is that of an oscillator subjected to an external step force due to the unfolding of the protein. Since the system is in an overdamped condition, the memoryless hypothesis holds.

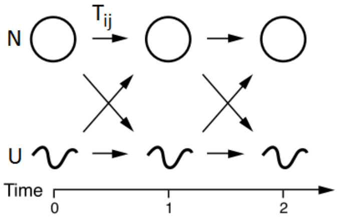

Fig. 20. Schematic of the HMM principle in the discrete-time case. At each time step, the system has constant probabilities T_{ij} of staying in the current state or jumping in the other one. From [110].

A THEORY FOR THE FOLDING FREE ENERGY After the states have been assigned to the data, it is possible to proceed with the extraction of the kinetic and energetic constants. In particular, the free-energy difference between two states i and j in a passive-mode experiment $G_{ij}(F_i, F_j)$ is directly related to the occupancies—or population probabilities—$P_i(F_i)$ and $P_j(F_j)$ by the Boltzmann distribution:

$$\frac{P_j(F_j)}{P_i(F_i)} = \exp\left(-\frac{G_{ij}(F_i, F_j)}{k_B T}\right). \tag{3}$$

The force F_i is the average value[5] of all points assigned to state i, and the occupancy $P_i(F_i)$ is the fraction of points assigned to state i.

In the dumbbell pulling geometry, the length change due to a protein folding/unfolding event is shared among all elastic components of the system, i.e. the portion of protein already unfolded, the DNA handles and the trapped beads (Fig. 10). For this reason, a model was proposed (*Berkemeier-Schlierf model*) to account for the additional energetic contribution of the elastic elements of the system [102].[6] The free energy $G_i(F)$ of the system at force F, when the protein is in the state i, can be written as the sum of the intrinsic energy of that state

---

[4] In passive-mode experiments, the system is at equilibrium, thus it follows the *principle of detailed balance*.

[5] Note that at each state is associated a force value, in Eq. 3 F_i and F_j. In the passive-mode assay, the length of the tether changes upon a transition, so does force (Fig. 19).

[6] The Berkemeier-Schlierf model was developed for AFM experiments, and adapted to optical tweezers experiments in a dumbbell assay by Gebhardt [37].

E_i and the aforementioned contributions of beads, DNA and unfolded protein regions:

$$G_i(F) = E_i + G^{\mathrm{beads}}(F) + G^{\mathrm{DNA}}(F) + G_i^{\mathrm{prot}}(F). \quad (4)$$

The terms related to DNA and protein unfolded regions are simply derived from Eqs. 1 and 2, respectively:

$$G^{\mathrm{DNA}}(F) = \int_0^{x_{\mathrm{eWLC}}(F)} F_{\mathrm{eWLC}}(x')\,\mathrm{d}x', \quad (5)$$

$$G_i^{\mathrm{prot}}(F) = \int_0^{x_{\mathrm{WLC}}(F)} F_{\mathrm{WLC}}(x')\,\mathrm{d}x'. \quad (6)$$

The beads are subject to a parabolic potential in the linear region of the trap, as for an Hookean spring:

$$G^{\mathrm{beads}}(F) = \frac{1}{2}k_{\mathrm{eff}}F^2. \quad (7)$$

Hence, the free-energy difference between the two states i and j in a passive-mode trace is:

$$G_{ij}(F_i,F_j) = E_{ij} + G_{ij}^{\mathrm{beads}}(F_i,F_j) + G_{ij}^{\mathrm{DNA}}(F_i,F_j) + G_{ij}^{\mathrm{prot}}(F_i,F_j). \quad (8)$$

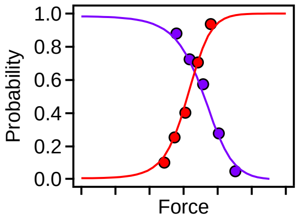

FIG. 21. Population probability vs. force plot, with same colouring as that of the previous graphs (red for unfolded, purple for native). Each point pair corresponds to a different passive-mode trace. Note that a pair is not aligned in force, because the force levels are different for native and unfolded states. This effect also results in the intersect not being at 0.5, but at a higher value. Solid lines are global fits obtained following Eq. 9.

ESTIMATION OF THE FOLDING FREE-ENERGY A single passive-mode trace already allows the extraction of the (force-independent) folding energy E_{ij} in Eq. 8. The force-induced energy difference $G_{ij}(F_i,F_j)$ is given by Eq. 3, by computing the population probabilities. In the example of Fig. 19, the system is under an average load of 3.5 pN and spends the same time in the native (N) and in the unfolded (U) state,[7] meaning that $G_{UN}(F_U = 3.2, F_N = 3.8) \approx 0$. The other terms of Eq. 8 can be computed from the fitting functions of force-ramps and from the trap calibration.

To determine the folding free-energy with higher precision, one possibility is to record different passive-mode traces at varying force, and to average the free-energy values extracted. A more elegant and exact way to obtain a single value for E_{ij} from a number of passive-mode traces is a *global fit* of the population probabilities vs. force plot (an example in Fig. 21). Recalling that the sum of the occupancies of each trace is unity, from Eq. 3 one gets

$$P_i(F_i) = \frac{1}{1+\sum_{i\neq j}\exp\left(-\frac{G_{ij}(F_i,F_j)}{k_B T}\right)}. \quad (9)$$

---

[7] Using the model of force-tilted potential in Fig. 15, this situation would correspond to the middle graph, where force drives the two states at about the same energy level.

All points can be fitted simultaneously (E_{ij} are the only free parameters), which is of particular interest if more than two states are present. The unfolding/unbinding midpoint force can be precisely determined from the fit (Box 5).

Using this method, it is also possible to control whether the data are correctly described by the model. The most relevant error in the free energies comes from the force calibration, and is estimated to be about 10 %, a value that will be used in this work.

BOX 5. MIDPOINT FORCE

A concept widely used within this thesis is the average force of an unfolding (or unbinding) transition. Given the population probability plot of Fig. 21, the *midforce* is the force where the two branches intersect, which is a simple estimate of the average transition force. This number clearly neglects the force dependence of the probability shifts, i.e. the slope of the curves, which is related to the CL difference between the two states. Nonetheless, it is usually a good indicator of the force that the construct can withstand.

AVERAGE LIFETIMES The HMM-based state assignment of a passive-mode trace further allows the extraction of the kinetic parameters, i.e. the rate constants.

A useful way of visualizing the time-scale of dwell events is to create a dwell time scatter plot. Each dwell event (a series of consecutive points with the same colour) can be plotted as the average force value vs. the time length, called *dwell time* (Fig. 22A). In a further analysis, the force axis can be converted to contour length space.

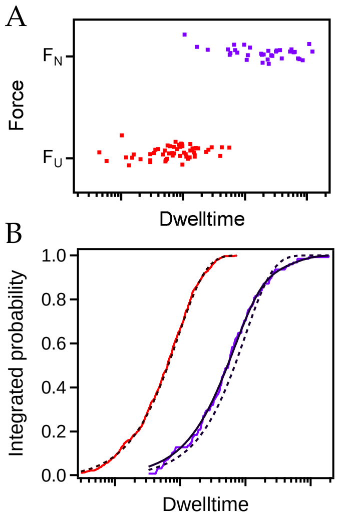

FIG. 22. Average lifetime extraction. (A) Dwell events scatter plot. Each event is a dot, represented as the average force of the event as a function of the dwell time (in log plot). (B) Dwell time integrated probabilities. In red, a single exponential distribution fitted with Eq. 10 (dotted line). In purple, a double exponential distribution fitted using Eq. 10 (dotted line) and Eq. 11 (solid line).

To compute the average lifetime, the dwell times of each state are cumulated in a normalised histogram (Fig. 22B). This plot can be interpreted as the probability $P(t)$ that a random dwell event lasts less or equal than t. For first-order reactions, the distribution is expected to be single exponential. Hence, to interpolate these distributions, an exponential function is employed, corrected with cut-offs for the shortest ($\tau_{\min}$) and the longest ($\tau_{\max}$) detectable events:[8]

$$p(t) = \frac{\exp(-kt) - \exp(-k\tau_{\min})}{\exp(-k\tau_{\max}) - \exp(-k\tau_{\min})}. \tag{10}$$

---

[8] In this thesis, the length of the time trace is used as $\tau_{\max}$, and the temporal resolution for $\tau_{\min}$. The latter depends on the pre-tension and ranges from 0.5 to 1 ms.

The fit returns the force-dependent rate constant $k = k_i(F)$ of state i at force F.

There may be cases where two different conformational states of the system show the same contour length, e.g. a misfolded state with the native CL, or a ligand-stabilised conformation. In such a case, the dwelltime cumulative distribution is expected to be double-exponential,[9] where A_1 and A_2 are the relative occurrences of the two states, and k_1 and k_2 the respective rate constants. The dwelltime integrated probability can be fitted using the following function:

$$p(t) = \frac{A_1(\exp(-k_1 t) - \exp(-k_1 \tau_{\min})) + A_2(\exp(-k_2 t) - \exp(-k_2 \tau_{\min}))}{A_1(\exp(-k_1 \tau_{\max}) - \exp(-k_1 \tau_{\min})) + A_2(\exp(-k_2 \tau_{\max}) - \exp(-k_2 \tau_{\min}))}, \quad (11)$$

corrected as before with the cut-offs. The errors in the rates are calculated using the *Jackknife method* [103].

FORCE DEPENDENCE OF TRANSITION RATES Performing the previous rate analysis for different passive-mode traces offers the opportunity to evaluate the force-dependent kinetics of the system (called a *chevron plot*, Fig. 23). The first theoretical interpretation was provided by Bell and Zhurkov [14], based on the force-dependent tilting of the energy landscape already introduced in Fig. 15. At equilibrium, the Boltzmann equation (Eq. 3) also holds for the transition rates $k_{ij} = k_{i \to j}$, with:

$$\frac{P_j(F_j)}{P_i(F_i)} = \frac{k_{ij}(F_i)}{k_{ji}(F_j)}. \quad (12)$$

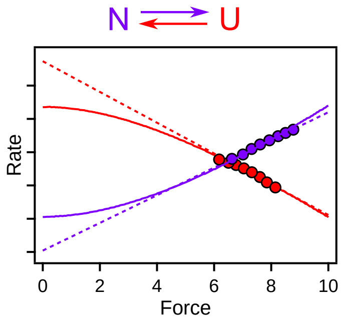

FIG. 23. Example of a rates vs. force *chevron plot* (rates are in log mode). Unfolding (purple) and folding (red) rates, fitted with the Zhurkov-Bell model (dotted lines) and with the Berkemeier-Schlierf model (solid lines). Note that, in log mode, the Zhurkov-Bell fit is a line.

The *Zhurkov-Bell model* considers transitions between a state i and the transition state T, at the top of the energy barrier. It assumes a force-independent distance Δx_{iT} to the transition state, while the free-energy difference $\Delta G_{iT}(F)$ is the only force-dependent term. According to this model, a constant force F modifies the off-rate of state i as:

$$k_i(F) = k_0' \exp\left(-\frac{\Delta G_{iT}(F)}{k_B T}\right) = k_0 \exp\left(\frac{F\,\Delta x_{iT}}{k_B T}\right) \quad (13)$$

where $k_0 = k_0' \,\Delta G_{iT}(F = 0)$ is the zero-force rate constant.[10] A fit of the rate vs. force plot with Eq. 13 returns the two free parameters k_0 and Δx_{iT} (dotted lines of Fig. 23).

---

[9] To experimentally observe different folding/binding modes, the two kinetics must be separated.

[10] To obtain the final form of the rate constant force-dependence, the simple argument employed is that $\Delta G_{iT}(F) = \Delta G_{iT}(F = 0) - F\Delta x_{iT}$.

The Zhurkov-Bell model is not the most accurate interpretation of data obtained with the dumbbell assay. When the system performs a transition from i into T, the contour length of the protein changes. As previously discussed, a change in CL affects the elastic behaviour of all elastic elements of the system, i.e. beads, DNA and unfolded protein regions, as in Eq. 8. To account for the elastic behaviour, a more sophisticated model was introduced by Berkemeier and Schlierf [102], by replacing the energy difference $\Delta G_{iT}(F)$ in Eq. 13 with the comprehensive energy of Eq. 8, with the added external potential $-Fx$. The resulting fitting function is bent, especially at low forces, as shown in Fig. 23 (solid lines).[11]

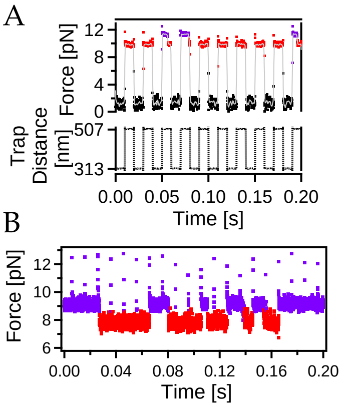

Fig. 24. Jump assay. (A) 200 ms excerpt of a jump trace where the trap position were changed every 10 ms. Colours refer to HMM analysis (folded state in purple, unfolded state in red). (B) Merged data from the upper level of a longer trace.

3.4 JUMP ASSAY

Jump experiments are carried out to obtain the unfolding kinetics at forces higher than those accessible with passive-mode traces. As introduced in Sec. 2.6, the basic experiment involves rapidly driving the system between *low* and *high* force conditions. An example is shown in Fig. 24A, together with the step stimulus obtained by changing position to the AOD-controlled trap. Further analysis relies on the hypothesis that the kinetics at the two forces are well separated, in this case meaning that the unfolding is negligible at the low force level, as it is the refolding at high force conditions. If this hypothesis is satisfied, the high level can be used to extract the unfolding kinetics. To automate the unfolding rate calculation, data collected at the same trap position are merged to form a passive-mode-like trace (Fig. 24B), enabling an HMM analysis.

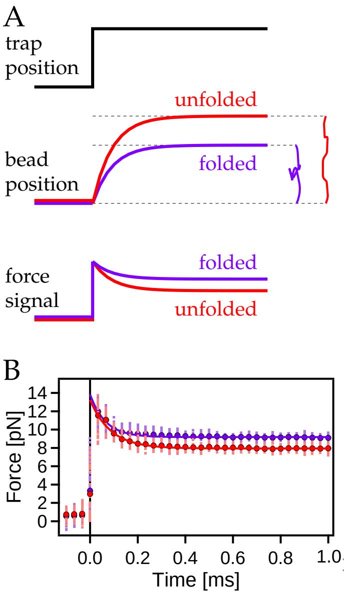

Fig. 25. Hydrodynamic relaxation of the AOD-controlled bead. (A) Schematic of the recorded data for a single jump for a folded (purple) and unfolded (red) protein. Force is proportional to the difference between the trap distance and the bead position. (B) Alignment of 50 jumps ending up in the folded (purple) and unfolded (red) states, where the average of all jumps is shown as big dots and exponential fits to the average data as lines.

The merged data in Fig. 24B show visible spikes in conjunction with the jumps. The origin of this effect can be ascribed to the short rise time of an AOD-driven laser movement ($< 10\,\mu s$), which makes it possible to detect the hydrodynamic relaxation of the bead in the AOD-controlled trap. Fig. 25A depicts a schematic of the recorded data with each jump: The force signal, proportional to the difference between the trap position and the bead position, shows a spike after a jump towards a higher force is applied, although the real force on the tether rises monotonically. The bead position changes in the same way. The spike in the force signal immediately after a change in trap position leads to the incorrect assignment of the hydrodynamic-related spikes as unfolding events, especially if the data analysis is automated with the Hidden Markov algorithm (Fig. 24A).[12]

---

[11] This was first experimentally confirmed in [99].

To evaluate the influence of the hydrodynamic effect, the alignment of the force signal of 50 jumps ending up in either the unfolded or the folded state was plotted (Fig. 25B). A fit of the average force signal with an exponential function[13] returns the relaxation time τ_{bead} of the beads, namely 65 µs for the folded state and 87 µs for the unfolded state. Using a safe upper limit of 100 µs, the signal is expected to settle to the steady-state within about $3\tau_{\text{bead}} = 300\,\mu\text{s}$ (9 points at the sampling frequency of 30 kHz). In this work, after each jump a correction was adopted, where the first 9 data points were substituted by a copy of the following 9 data points.[14]

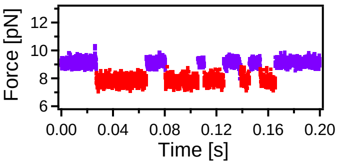

Fig. 26. Merged data as in Fig. 24B, but with the first 9 data points after each jump corrected as explained in the text.

After the correction of the data (Fig. 26), the unfolding rates at high forces can be extracted from the high position level as described for the passive-mode trace analysis.

3.5 COMPETITION ASSAY

In Sec. 2.6 the competition assay was introduced as a tool for the measurement of the binding affinity between two proteins.

In a fusion contruct (see Fig. 3), the interaction between the two proteins can be probed by force. Unbinding/rebinding transitions in passive-mode traces are analogous[15] to unfolding/refolding events in Fig. 19.

---

[12] Some more details relating to the jump assay and the Hidden Markov classifier. Firstly, it may be asked why the HMM succeeds in detecting ∼5-point events (∼ 150 µs), despite the fact that the usual cut-off is at least 3 times higher (> 500 µs). The reason is that the high force level of the spikes makes the algorithm significantly more efficient in assigning the points to the folded state. Secondly, how can one be sure that the system didn't actually refold in the 10 ms spent at zero force, and that the spikes are not short-lived folded events? Here, kinetic arguments can be used to demonstrate that such a high frequency of short events does not fit the single-exponential distribution expected for the dwelltimes.

[13] The relaxation of a bead in a parabolic potential (optical trap) under overdamped conditions is exponential.

[14] Note that the detection of real folded events is not affected, since the cut-off introduced by this correction is 300 + 300 µs, only slightly bigger than the usual minimal cut-off.

[15] To be precise, unbinding kinetics can be accurately studied if the breakage of the bond can be separated from the unfolding of the domains. This is a common case for weak bonds, where the binding/unbinding kinetics is observed at lower forces than those required to unfold the domains, like for filamin ligands

In a classical bimolecular reaction:

$$A + B \underset{k_{\text{off}}}{\overset{k_{\text{on}}}{\rightleftharpoons}} AB,$$

at *equilibrium* the ratio between the concentrations of reactants and products is constant, and equals the ratio between the off- and the on-rates. The dissociation constant K_D is defined as such a ratio:[16]

$$K_D = \frac{[A][B]}{[AB]} = \frac{k_{\text{off}}}{k_{\text{on}}}. \tag{14}$$

A way to interpret the dissociation constant is by using the Langmuir binding model [94], where for simplicity A is considered as a substrate and B as a ligand. Fixing the concentration of substrate A, K_D is the concentration of ligand B at which half of substrate sites are occupied. The probability of a site A being free is:

$$P_{\text{unbound}} = \frac{1}{1 + \frac{K_D}{[B]}}. \tag{15}$$

This equation comes from the definition of $P_{\text{bound}} = [AB]/([A] + [AB])$, the substitution of $[AB]$ with the definition of K_D (Eq. 14), and finally considering the relationship $P_{\text{unbound}} = 1 - P_{\text{bound}}$.

In a single molecule experiment using a fusion construct, a single pair of proteins A and B is employed. In this case, the estimation of the binding affinity depends on the *effective concentration* of the ligand [B], which is difficult to determine with precision (Box 6).

The competition assay overcomes the previous limitations, thanks to the addition of the same ligand to solution at a known concentration [B]. Binding from solution occurs at the same force level as that of the open state of the fusion construct, i.e. when the tethered molecules A and B are detached. The example in Fig. 27 shows that, at sufficiently low preloads, binding from solution is distinguishable from the open state by lifetime.

The off-rates can be simply extracted from the average lifetime of the cyan states, namely $\tau_{\text{bound}} = k_{\text{off}}^{-1}$.

---

[99]. If unfolding-upon-unbinding occurs, for example in the titin/telethonin complex [15], it is difficult to separate the two kinetics, and what is discussed below does not hold anymore.

[16] Note that the units of the on- and off-rates are different. $[k_{\text{off}}] = \text{s}^{-1}$ is concentration independent, because the unbinding purely depends on the strength of the bond. On the other hand, $[k_{\text{on}}] = \text{s}^{-1}\text{M}^{-1}$, because the binding is dependent on the concentration of the ligand.

BOX 6. AFFINITY FROM FUSION CONSTRUCTS

Using a fusion construct, the dissociation constant can be estimated using Eq. 15. The probability of finding A and B unbound P_{unbound} is the zero-force value of the occupancy vs. force plot, extracted from the fit of the graph (Eq. 9 and Fig. 21). This estimation of K_D relies on the knowledge of the concentration of ligand [B], which may seem a contradictory concept, since only one ligand is present in the experiment. In fact, the linker between the molecules sets the concentration of the ligand. Fixing one molecule A in space, the ligand B is constrained by the linker to a finite volume, that determines its *effective concentration* [B]. This value is difficult to measure or calculate, thus leading to a high uncertainty in the extraction of K_D. In analogy, the estimate of the binding affinity from the rates (Eq. 14) suffers from the same limitations. The average lifetime of the unbound state, accessible to the experiments, is related to the pseudo-first order rate $\tau_{\text{unbound}} = \tilde{k}_{\text{on}}^{-1}$, which is in turn dependent on the effective concentration of the ligand [B], $\tilde{k}_{\text{on}} = k_{\text{on}}[\text{B}]$. Again, the data obtained from a fusion construct are linker-dependent, as longer linkers will lead to a smaller effective concentration, thus to slower rebinding. The competition assay introduces a new state in the kinetic network, but the concentration of the ligand [B] in solution is known.

To estimate the on-rates, it has to be recalled that only the open conformation (green) of the fusion construct is able to bind the ligand from solution, since in the closed conformation (purple) the binding site is occupied by the tethered ligand. Hence, the dwell time of a binding event is evaluated by summing up the total time spent in the open state (yellow dwell), between two subsequent appearances of cyan events. The pseudo first-order on-rate $\tilde{k}_{\text{on}}$ is obtained from a single exponential fit of the cumulative yellow dwell time distribution. The dissociation constant is

$$K_D = \frac{k_{\text{off}}}{\tilde{k}_{\text{on}}}[\text{B}]. \tag{16}$$

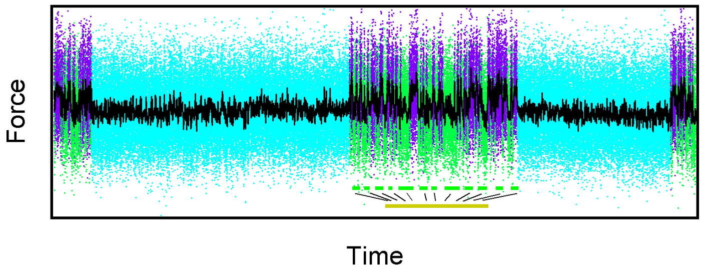

FIG. 27. Competition assay. The binding from solution (cyan) quenches the rapid transitions between the open (green) and closed (purple) conformation of the fusion contruct. To estimate the on-rates, the time spent by the system in the open conformation between two consecutive cyan events is summed up (yellow dwell event).

Note that by combining the Boltzmann equation to Eq. 15, the dissociation constant can be linked to the binding free-energy E_{binding}:

$$K_D = [\mathrm{B}] \exp\left(-\frac{E_{\text{binding}}}{k_B T}\right). \tag{17}$$

Part II

α-ACTININ/TITIN INTERACTION

4

TITIN ANCHORING IN THE Z-DISK

Striated muscle sarcomeres are formed by a network of proteins that retain a semi-crystalline organisation over years, while being repeatedely subjected to high strains.

The main players that contribute to the astonishing regularity of the sarcomere, besides the well known thick (myosin) and thin (actin) filaments, are three giant, muscle-specific proteins, titin (3–4 MDa), nebulin (0.6–0.8 MDa), and obscurin (0.7–0.9 MDa), whose studies were hampered for a long time by their large size.[1]

The minimal contractile unit of muscles is the sarcomere, which is not only able to apply active forces during contraction (Sec. 4.1), but also to resist elongation like a spring (4.2). The major contributor to this so-called "passive" stiffness is titin, which spans half of the sarcomere and provide restoring forces upon stretching. To this purpose, a tight anchoring of titin both in the middle of the sarcomere and at its edge, in the Z-disk, is required (4.3). The distal anchoring is still under debate, and the interaction with the actin crosslinker α-actinin has been identified as a promising candidate (4.4), which is the subject of the experiments of chapters 5 and 6.

4.1 THE SARCOMERE IS THE BASIC CONTRACTILE UNIT OF STRIATED MUSCLES

The understanding of the molecular processes underlying the muscle functioning was obscure until the second half of the 20th century. Thanks to the development of novel imaging techniques such as electron, phase-contrast or interference microscopy, as well as the refinement of existing ones such as X-rays, it was possible to study in more detail the organisation of the sarcomere, the smallest independent contractile unit of all striated muscles.

At first sight (Fig. 28), a myofiber, formed by many sarcomeres, appears as a regular alternation of regions

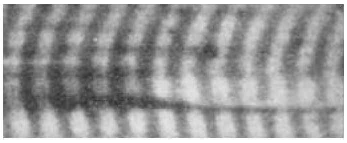

Fig. 28. Muscle fiber image obtained with interference microscopy in positive contrast (A-bands are dark). From [50].

---

[1] Obscurin was discovered only in 2001 [134].

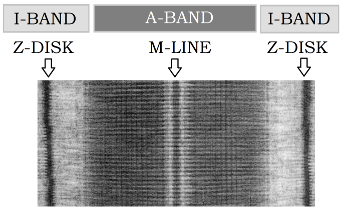

FIG. 29. Electron-microscopy image of a single sarcomere, and division into different zones. Due to the increased resolution, dark lines are visible. Termed Z-disk, they are the regions where adjacent sarcomeres overlapped and interact with each other. Adapted from [74].

with high refractive index (termed A-bands) as opposed to ones with lower refractive index (I-bands). Electron microscopy (EM) images of a single sarcomere (Fig. 29) [51] confirmed the proposed filamentous nature of actin and myosin. Moreover, they made it possible to observe the alternation of thin (actin) and thick (myosin) filaments, and their partial overlap. The knowledge of the filaments arrangement ruled out many proposed mechanism of muscle contraction, paving the way to the sliding filaments hypothesis [51], by H. Huxley and J. Hanson. This model states that, upon contraction, myosin motor bind to actin filmanents pull them toward the center of the sarcomer, shortening the basic contractile unit. Nowadays many more detailes regarding the active contraction process are well understood [38].

To achieve a contraction of the whole muscle, it is necessary that each sarcomere is linked to the adjacent ones. This task is accomplished by α-actinin (Box 7), a protein that is able to crosslinks two actin filaments from adjacent sarcomeres (Fig. 30). A number of α-actinin layers are present in the Z-disk, the distal region of the sarcomere, very dark in the EM image of Fig. 29 because of the high protein density. Here actin filaments coming from different sarcomere overlap with each other and anchoring is achieved by α-actinin crosslinking (Fig. 30).

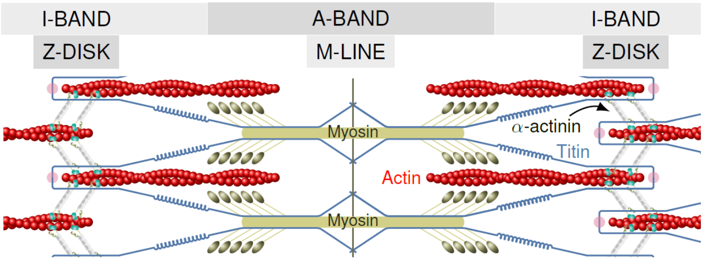

FIG. 30. Schematic of the sarcomere. The actin and myosin filaments are shown, together with the actin crosslinker α-actinin (only two copies are depicted) and the huge titin molecule.

4.2 THE ROLE OF TITIN IN MUSCLE ELONGATION

While the contraction process has been now clarified in great detail, the inverse process, i.e. muscle elongation, is still poorly understood. The property of muscle fibers to generate a non-linear restoring force was observed and evaluated in 1881 [101]. It is already expected for muscles to have some internal springs which restore their initial position after elongation: The cardiac muscle alternates between contraction (systole) and relaxation (diastole) on the timescale of seconds, and skeletal muscles are are ofter coupled in "agonistic-antagonistic"

BOX 7. α-ACTININ-2

α-Actinin-2 is an antiparallel homodimer formed by 104 kDa monomer and present in the Z-disk of striated muscles. Four isoforms of α-actinin have been identified, two non-muscle calcium-regulated, 1 and 4, and two muscle calcium-insensitive, 2 and 3 [106]. Each subunit consists of an Actin Binding Domain (ABD) at one edge, four Spectrin-like Repeats (SR) in the central part and two EF-hands Calmodulin-like Domains (CaMD) at the other edge (Fig. 31A). The distal domains (ABD and CaMD) are the functional regions, while the central SR of the two monomers form a rigid rod domain, providing the right spacing between actin filaments. A region called the neck separates the ABD from SR1. The current regulatory model of α-actinin suggests that EF3-4 of one subunit can bind to the neck region of the opposite subunit (closed conformation, Fig. 31A). In the Z-disk, activation of α-actinin is mediated by PIP2, that reduces the affinity between the neck the EF3-4 (open conformation, Fig. 31B) [97, 132]. The latter can thus interact to different binding partners, in particular to the giant protein titin. Depending on the muscle type and on the species, there can be from 2 to 6 α-actinin layers [75].

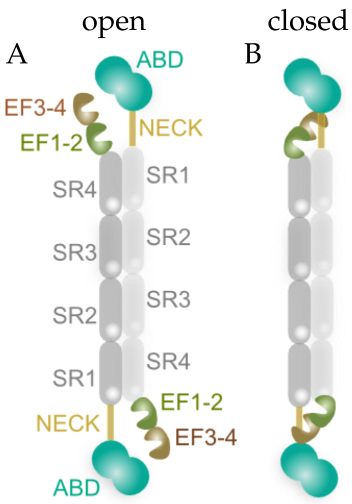

Fig. 31. Schematic of α-actinin quaternary structure. Abbreviations as in the text. (A) Open conformation activated by PIP2 in the Z-disk, where EF3-4 can bind titin. (B) Closed conformation, where EF3-4 of one subunit binds the neck of the juxtaposed subunit, thus inhibited interaction with titin.

pairs, that enhance the coordination and the smoothness of the movements.

Upon stretch actin and myosin are not bound anymore, thus some other internal or external element has to generate such a restoring force. Initially the extracellular collagen was considered the best candidate to provide the muscle with passive stiffness, until in 1977 Maruyama *et al.* [81] discovered an elastic intrasarcomeric filament connecting the central region of the sarcomere (M-band) with its distal part (Z-disk). This elastic element was composed of a single protein, initially called *connectin* and soon renamed *titin* because of its titanic size (3–4 MDa) [123]. Since that discovery, the generation of passive forces has become the focus of many studies, in particular after the complete titin sequence was revealed in 1995 [64]. Titin has been proved to provide the passive stiffness of the muscle at low muscle extentions, while at high elongations the contribution of the extracellular collagen gets more and more prominent [129] (Fig. 32). Titin is also involved in signaling processes and disease[43, 54]. More details on how titin is partitioned along half a sarcomere are given in Box 8.

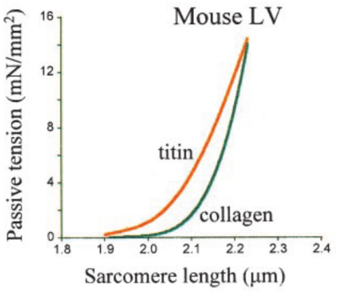

FIG. 32. In mouse left ventricular (LV) myocardium, contribution of titin and collagen to passive stiffness. Physiological sarcomere length ranges from 1.9 to 2.2 μm. For small elongations, titin provides with 90% of the total stiffness, while the two contributions gets equilibrated at large stretch. Data from [43].

BOX 8. TITIN

To date, titin is the largest known protein. It's length is about 1 μm, and it contributes to up to 0.5 kg of our body weigh[65]. Titin has a modular molecular structure, that can be divided in three parts, depending on the location of the domains in the sarcomere. In the A-band, an array of immunoglobulin-like (Ig) and fibronectin-3-like (fn3) interacts with myosin filaments, affecting contraction efficiency [70] and providing titin anchoring. The extensible region is entirely situated in the I-band, where three elements can elongate and contribute to titin stiffness: tandem Ig domains, the PEVK domain and the N2B unique sequence [67, 126]. The Z-disk region is composed of a short sequence (135 amino acids) called Zq, up to seven modular units (45 amino acids) called Z-repeats, and two Ig-like domains. The Zq region and the Z-repeats have been shown to bind α-actinin [35, 133], while the Ig domains of two titin molecules are crosslinked at the N-terminal by telethonin [45, 138] (Fig. 33).

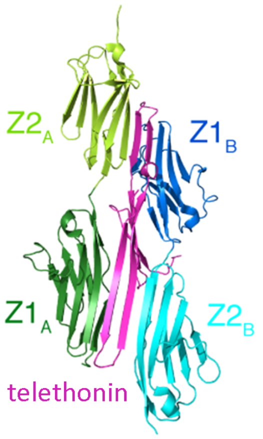

FIG. 33. Titin/telethonin complex (PDB 1YA5) [138]. The two N-terminal Ig-like domains Z1 and Z2 of two different titin molecule (A and B) form a palindromic sandwich structure with the protein telethonin.

4.3 TITIN ANCHORING IN THE SARCOMERE

To elongate like a spring and provide a restoring force, titin needs to be tightly anchored both in the A-band and in the Z-disk. In the A-band, the interaction of titin with myosin via C-proteins and with obscurin at its C-terminus seems to provide a firm attachment [28, 48, 70, 86, 93]. However, a detailed understanding on where and how titin is fixed at its N-terminus, embedded in the Z-disk, is still lacking.

The streching force to which titin is subject under muscle elongation has been estimated in a number of studies [1, 67, 126], by dividing the tension on the whole myocite (red curve in Fig. 32) for the number of sarcomeres and the number of titin molecules per sarcomere. In the physiological range of sarcomere elongation 1.9–2.2 μm, the force should not exceed ~ 5 pN.

Many binding partners of titin have been identified in the Z-disk. The interaction of titin with telethonin has been initially proposed as a promising candidate for titin anchoring in the Z-disk [45]. Two titin molecules are linked together at the N-termini by telethonin, in a palindromic structure [138] (Fig. 33) that forms one of the most stable non-covalent bonds measured so far ($\sim$ 800 pN)[15]. Nonetheless, some knock-out studies performed on different species showed that the integrity of the muscle is not drastically affected by telethonin depletion [53, 137]. Moreover, it is still not clear how this complex can bind to actin (see Box 9 for details).

BOX 9. REQUIREMENTS FOR Z-DISK TITIN ANCHORING

To look for possible candidates, it is worth to focus on the direction of load propagation. After the muscle elongates, force propagates through titin molecules of adjacent sarcomeres. Titin relaxation restores sarcomere rest length and brings the actin filaments back toward the A-band. To this purpose, a connection between titin molecules of neighbouring sarcomeres is required, in analogy to actin crosslinking. While a direct titin/titin interaction is not very likely at the actual state of knowledge, it is sufficient that titin is somehow tightly bound to an actin filament, in order to take advantage from the aforementioned actin crosslinking mediated by α-actinin.

Apart from a direct [71] and an indirect [133] binding with actin, the main candidate is the interaction of titin with the EF-hands 3 and 4 of α-actinin [33–35, 70] (Fig. 34), which will be described in detail in the following section.

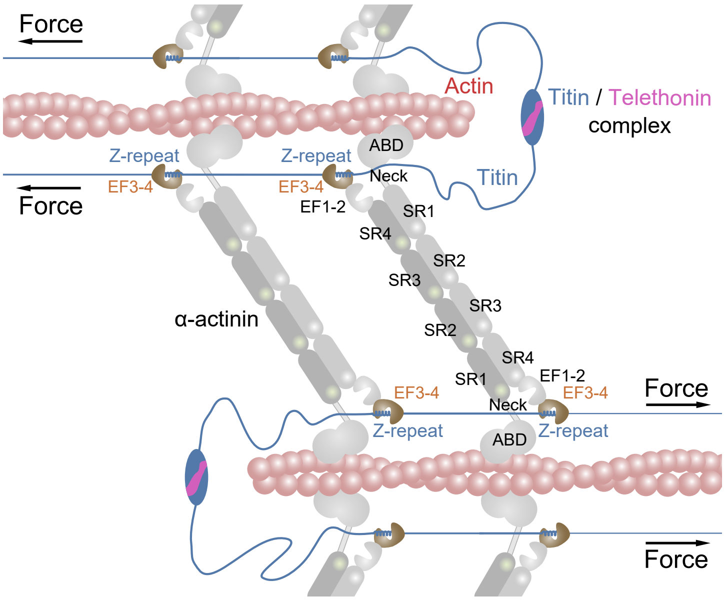
Force
Actin
Titin / Telethonin
complex
ABD
Z-repeat
Z-repeat
Neck
Titin
EF3-4
EF3-4
Force
EF1-2
SR1
SR4
SR2
SR3
SR3
α-actinin
SR2
SR4
SR1
EF1-2
EF3-4
EF3-4
Force
Neck
Z-repeat
Z-repeat
ABD
Force

Fig. 34. Schematic of the Z-disk arrangment of actin, titin, α-actinin and telethonin (only two crosslinkers are shown), and direction of force propagation upon muscle stretching.

4.4 α-ACTININ/TITIN INTERACTION

The region of titin that binds α-actinin EF3-4 is formed by up to seven repeated motifs called Z-repeats (Fig. 35A) that can be differentially spliced. The number of Z-repeat depends on the species, on the muscles and on the development stage of the muscle (Fig. 35B), and is thought to determine the thickness of the Z-disk

[35, 108]. For example, titin from human adult cardiac muscle has the whole sequence, from T1 to T7 (45 kDa).

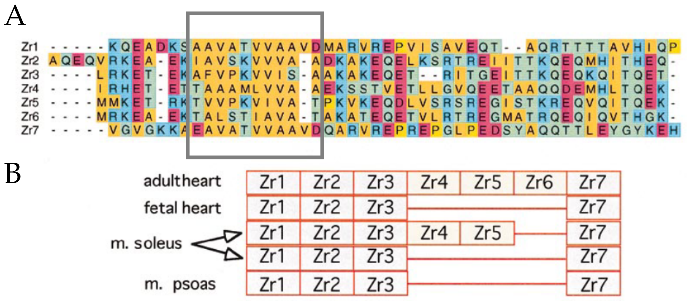
A
Zr1 ------KQEADKSAAVATVVAAVDMARVREPVISAVEQT--AQRTTTTAVHIQP
Zr2 AQEQVRKEA-EKIAVSKVVVA-ADKAKEQELKSRTREIITTKQEQMHITHEQ-
Zr3 -----LRKET-EKAFVPKVVIS-AAKAKEQET--RITGEITTKQEQKQITQET-
Zr4 -----IRHET-ETTAAAMLVVA-AEKSSTVETLLGVQEETAAQQDEMHLTQEK-
Zr5 -----MMKET-RKTVVPKVIVA-TPKVKEQDLVSRSREGISTKREQVQITQEK-
Zr6 -----MRKEA-EKTALSTIAVA-TAKATEQETVLRTREGMATRQEQIQVTHGK-
Zr7 ------VGVGKKAEAVATVVAAVDQARVREPREPGLPEDSYAQQTTLEYGYKEH
B
adultheart
Zr1 Zr2 Zr3 Zr4 Zr5 Zr6 Zr7
fetal heart
Zr1 Zr2 Zr3 Zr7
m. soleus
Zr1 Zr2 Zr3 Zr4 Zr5 Zr7
Zr1 Zr2 Zr3 Zr7
m. psoas
Zr1 Zr2 Zr3 Zr7

Fig. 35. Alignment of Z-repeats (here termed Zr) and their differential expression. (A) Amino acid sequences of the seven Z-repeats present in the rabbit cardiac titin (hydrophobic residues in orange). The grey square mark the region that binds to α-actinin. (B) Z-repeats isoforms present in different muscle, showing how T1-T3 and T7 are always present, while T4-T6 can be differentially spliced. From [108]

The Z-repeat 7 has been shown to form an α-helical structure if bound to the hydrophobic pocket of α-actinin EF3-4 (Fig. 36), a typical binding scheme for Calmodulin-like domains [10].

The affinity of all titin Z-repeats with EF3-4 has been evaluated in bulk experiments [56]. Three classes of repeats have been identified: the distal repeats T1 and T7, showing reasonable binding, with affinities in the submicromolar range. Repeat T3 has a weaker interaction with EF3-4, while the other repeats did not show detectable binding, e. g. gain in helical signal under far-UV circular dichroism measurments.

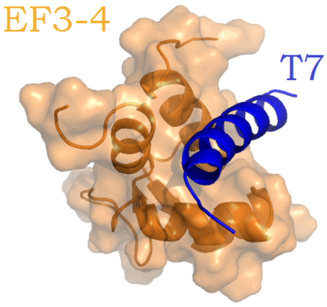

Fig. 36. NMR structure of the complex formed by α-actinin EF3-4 and titin Z-repeat 7 (T7) [10]. 18 amino acid over a total of 49 are involved in the α-helical secondary structure of T7.

4.5 SUMMARY

The smallest contractile unit of the skeletal and cardiac muscles is the sarcomere, an intricate network of proteins organised in a semi-crystalline manner. A single sarcomere is able to exert active forces upon contraction, as well as restoring (passive) forces if streched. The huge protein titin has been found to provide the majority of the sarcomere stiffness under muscle elongation. For this task, titin needs to be tightly bound at both termini, in two sarcomeric regions termed the I-band and the Z-disk. The molecular determinants of titin anchoring in Z-disk are still under debate, and the interaction with the EF3-4 domain of α-actinin has been selected as a promising candidate. This multi-valent bond was experimentally investigated in this thesis, and the results described in chapters 5 and 6.

5

α-ACTININ BINDING TO TITIN Z-REPEAT 7

To study the mechanics of the α-actinin/titin interaction, the EF hands 3 and 4 of α-actinin were fused to the 23 residues of Human titin T7 resolved in the NMR structure (Fig. 37, complete sequences in appendix C.3), via a 4× `(GGS)` linker. The cystein residues for force application were placed at the N- and C- termini, separated from the fusion construct by ubiquitin domains. This construct was called PullA-T7, because the force is transduced through both proteins.

The first section (5.1) deals with the typical fingerprint of the fusion construct under force-ramps. The unfolding pathway is then explored (5.2) by means of equilibrium measurments. A jump assay is employed to extend the force range of the unbinding kinetics (5.3), and occupancies and rate-constants are collected (5.4). The affinity of the interaction is extracted using a competition assay (5.5). The physiological relevance of the measured data is discussed (5.6) and another construct with different pulling positions is introduced and measured (5.7).

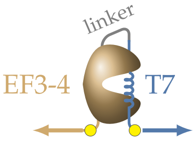

Fig. 37. Fusion construct of α-actinin EF3-4 and titin T7.

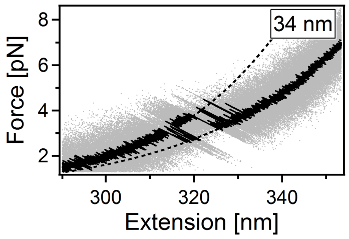

Fig. 38. Constant velocity trace of the PullA-T7 construct obtained at the pulling speed of 10 nm/s. Dotted lines are WLC fits (see Sec. 3.2).

5.1 CONSTANT VELOCITY TRACE

By increasing the tension on the PullA-T7 complex at a constant velocity (Fig. 38), the unbinding of titin from α-actinin starts at surprisingly low forces. At the low pulling speed of 10 nm/s, the system undergoes rapid transitions, apparently between two states. WLC fits shown in Fig. 38 reveal a contour length increase of 34 ± 1 nm, which corresponds to both unbinding of T7 from the EF3-4 as well as unfolding of both domains. While the T7 α−helix is expected to fold together with the binding,[1] the EF hands 3 and 4 may fold indipendently, potentially allowing an intermediate state in the unfolding pathway (Fig. 39). Nonetheless, the resolution

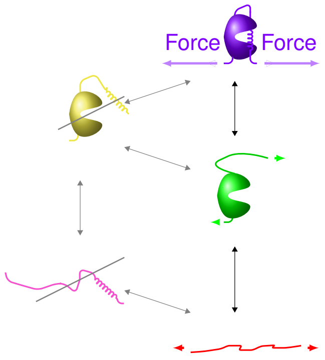

Fig. 39. Unfolding pathway of the PullA-T7 construct. Since the unbound T7 peptide is unfolded, the states involving a folded and unbound peptide were not expected to be observed (left column).

---

[1] Single helical peptides are rarely structured in absence of their binding partners. Although they may transiently fold, their mechanical and thermal stability is usually negligible.

of force ramps is not sufficient to determine the existence of such an intermediate state.

5.2 UNFOLDING PATHWAY

To get a better insight into the binding kinetics under load, a series of passive-mode experiments was carried out, like the one depicted in Fig. 40A.

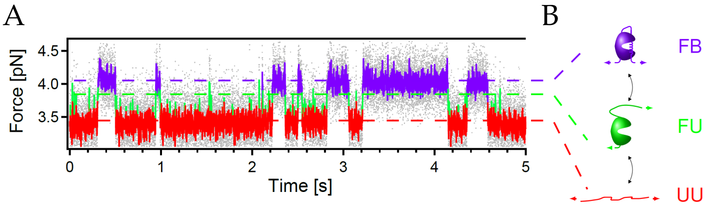

Fig. 40. Passive-mode analysis of PullA-T7 construct. (A) Time trace of pullA-T7 (5 s extract). The colours corresponds to the three states represented in *B*, assigned to the data by means of HMM analysis. (B) State network of the PullA-T7 construct.

Each trace was analyzed using the Hidden Markov Model algorithm (Sec. 3.3) to assign states to data points. For this analysis it is required to set the number of intermediate states, as well as the transition rates and the force values. Following the premises of the previous section, the system was allowed to explore the three-state network of Fig. 40B. Beside the completely unfolded/unbound state (called UU and drawn in red) and the folded/bound state (FB, purple), an intermediate on-pathway conformation was assumed, where the EF3-4 domain is folded and the T7 peptide unbound and unfolded (FU, green).[2] The initial force value of the FU state was chosen in a way that the contour length gain (Box 4 in Sec. 3.2) from the FB state was 12 nm, which is the value calculated from the structure. From each passive-mode trace, the kinetic and energetic parameters were extracted, as explained in the next sections.

5.3 KINETICS AT HIGH FORCES: JUMP ASSAY

The range of forces accessible with passive-mode experiments is very narrow for the PullA-T7 construct. Already at the average force of 4.5 pN, the FB events become very rare, as shown in Fig. 41, and it is necessary to acquire very long traces to collect a significant statistic of binding events.

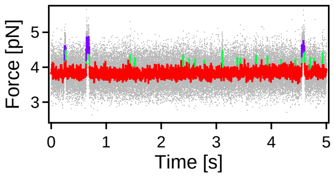

Fig. 41. Passive-mode trace at the average force of 4.5 pN.

---

[2] Some lines of evidence that the green events correspond to the FU state (EF3-4 folded and T7 unbound) are discussed in appendix A.2. In particular, the same state shows up in a construct where force is applyed on the pure EF3-4 domain (PullA construct). The alternative hypothesis that FU is not an on-pathway intermediate is discussed in the same section of the appendix.

In order to estimate the force-dependent unbinding kinetics of T7 on a larger force scale, a jump assay was performed (see methods and Fig. 42), by rapidly steering the AODs trap between a high force level (7 to 15 pN) and a low force level ($\sim$ 0 pN).

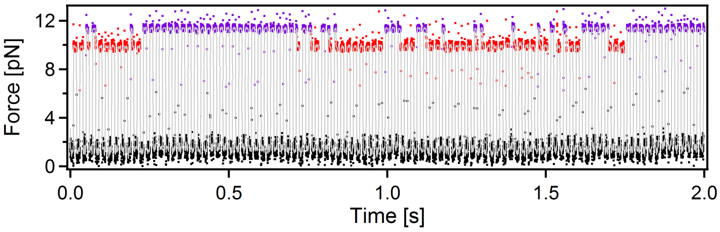

Fig. 42. Time trace of pullA-T7 probed with the jump assay (2 s extract). The position of the mobile trap was changed every 10 ms. The trace was analyzed with a two-state HMM algorithm to better visualise the FB (purple) and UU (red) configuration (the FU state is too short-lived at these forces to be detected).

Using this tool it is possible to collect a high statistics in a reasonable amount of time, since driving the system to low forces allows rapid refolding of the EF3-4 and rebinding of the T7 peptide. The data were sorted in low- and high-force level and merged to form passive-mode-like traces, as explained in (see section 3.4). These merged traces were analyzed with the HMM algorithm, and the extraction of FB→FU transition rates carried out using the standard procedure. With the jump assay, the unbinding rates were measured until 15 pN, with a notable increase of the force range.[3]

5.4 FORCE-DEPENDENT KINETICS AND MECHANICS

In Fig. 43 the population probabilities of the three states at different forces are plotted. The free-energy differences between the states were obtained using a global fit of these data. The binding energy of the T7 peptide is 4.2 $k_{\mathrm{B}}T$, whereas the folding energy of EF3-4 is only 0.5 $k_{\mathrm{B}}T$, meaning that the domain itself does not have a high mechanical stability.

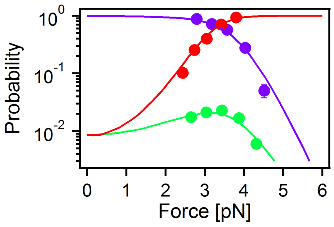

Fig. 43. Population probability vs. force for the PullA-T7 construct. Each point corrponds to the occupancy in a passive-mode trace. Solid lines are fit obtained as explained in Sec. 3.3.

The midforce of the unbinding/unfolding processes is the force at which the graphs intersect (Box 5). In such a three-state system, the unbinding force of T7 is 6 pN (intersection of the green and purple fits), and the unfolding force of the EF3-4 is 0.5 pN (intersection of the red and green fits).

---

[3] As mentioned in section 3.4, merging the upper level instances results in neglecting the time spent at zero-force. Hence, the dwell-times of the FB state are measured in the hypothesis that at zero-force the unbinding of the peptide is negligible compared to that at high preload. In this case, the low force dependence (see fits of Fig. 44B) does not lead to a huge difference between unbinding rates at high and low forces. Nonetheless, the rates were at least a factor of 4 faster at the high forces probed with the jump assay.

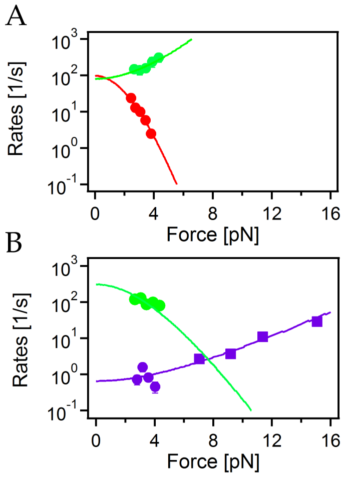

Fig. 44. Transition rates for pullA-T7 and fit (solid lines). A, rate constants for the transition UU↔FU. B. Rate constants for the transition FU↔FB. Square dots are obtained using the jump-assay.

The force-dependent folding and unfolding transition rates of the EF3-4 domain (transition UU↔FU) are plotted in Fig. 44A, together with fits obtained using the Berkemeier-Schlierf model.[4] At $F = 0.5\,\text{pN}$, where the transition rates fitting function intersect, the EF3-4 domain spends half of the time folded and half unfolded, with a fast exchange rate of $\sim 100\,/\text{s}$.

Fig. 44B shows the binding/unbinding kinetics of the T7 peptide (FU↔FB), where the purple unbinding rates are extended until 15 pN thanks to the jump-assay (square dots). The zero-force rate constants are $0.6 \pm 0.1\,\text{s}^{-1}$ for the unbinding and $302 \pm 17\,\text{s}^{-1}$ for the rebinding. The force dependence of the unbinding rate is extremely weak: the rates increse of one order of magnitude within about 10 pN. This is a direct consequence of the small distance (2 nm) between the FB state and the transition state.

5.5 BINDING AFFINITY: THE COMPETITION ASSAY

The measurements presented up to this point comprehend a mechanical characterisation of the protein complex, but are lacking the estimation of the binding affinity between the two proteins. As introduced in sections 2.6 and 3.5, the competition assay can overcome this limitation.

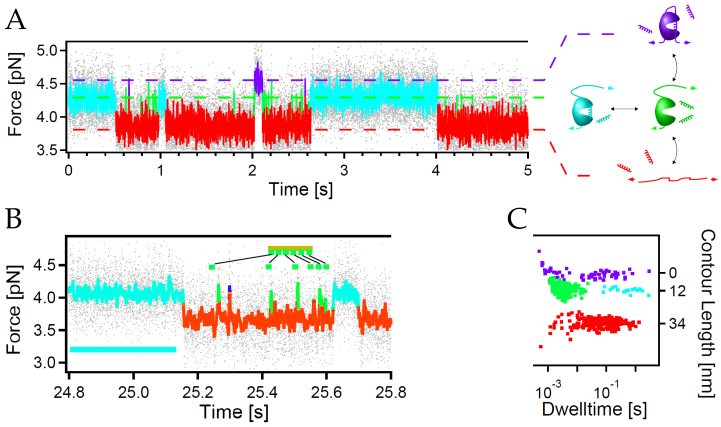

Fig. 45. Competition assay. (A) Passive-mode experiment with 52 µM of free peptide T7long in solution, and schematic of the binding pathway (right hand side). (B) Zoom of 1 s and dwell times estimation. (C) Contour length vs. dwell time scatter plot. The separation of green and cyan events was obtained introducing a time threshold at 0.06 s.

---

[4] From the scatter plot of CL vs. dwell time it is possible to extract the transition rates between the different states (Sec. 3.3). While the UU and FU states are exponentially distributed, the FB state exhibits a double exponential behaviour, both in passive-mode and in jump experiments. The slow (more stable) kinetics are plotted in Fig. 44B, and a detailed discussion of this effect is presented in appendix A.1.

The PullA-T7 construct was kept under load in passive mode with the addition of $52\,\mu\mathrm{M}$ of the T7 peptide in solution. A competition between the tethered and the free peptides was established (Fig. 45A). Given the assumed pathway of Fig. 40B, the binding of the peptide in solution occurs via the obligatory FU state, but contrary to the tethered peptide, it does not lead to any change in contour lenght. Nonetheless, the binding from solution can be monitored, because it stabilises the EF3-4 domain, increasing the dwell times of the FU state. A new cluster of events is now present in the CL vs. dwell time plot, corresponding to the binding of the peptide in solution. The cluster can be separated from the FB states using a time threshold (cyan dots in Fig. 45C).

The average lifetime of the cyan state directly leads to the zero-force unbinding rate $k_{\mathrm{off}} = 1.3 \pm 0.5\,\mathrm{s}^{-1}$, a factor of two faster than that extrapolated from the slow phase of the passive-mode traces. The pseudo first-order on-rate was obtained from the distribution of the binding events. A binding event (in yellow in Fig. 45B) is calculated by summing up all the FU events in between two subsequent cyan events,[5] and the distribution leads to $\tilde{k}_{\mathrm{on}} = 17 \pm 6\,\mathrm{s}^{-1}$. The binding affinity, calculated using Eq. 16, is $K_D = 4 \pm 2\,\mu\mathrm{M}$.[6]

5.6 A BETTER ESTIMATION OF THE MIDPOINT FORCE

The PullA-T7 construct presented up to this point exhibits interesting features necessary for the mechanical characterisation of titin anchoring in the Z-disk. It is clear from the data how the EF3-4/T7 interaction has very fast kinetics: even in absence of external load, the bond has a lifetime shorter than 2 s. Moreover, the midpoint force of this construct is very low: Owing to the low occupancy of the FU green state, the midforce is the intersection between the purple and red branches of

---

[5] To be precise, each binding event from solution is a sequence of three events that cannot be separated, (1)FU (2)peptide bound (3)FU. This observation implies that each unbinding dwell time is overestimated, while each binding dwell time is underestimated. Hence, a correction was performed, where the average lifetime of the FB green states was subtracted twice from the cyan lifetime and added twice to the yellow lifetime.

[6] Given the affinity, the effective concentration of the tethered peptide can be estimated. This calculation, together with a direct measurement of the effective concentration obtained with the jump assay, is presented in appendix A.3.

Fig. 43, that is 3.5 pN. This value is within the range of physiological loads a single titin molecule may experience, i. e. 0–5 pN (Sec. 4.3).

While the N-C-termini pulling geometry properly simulates the force propagation through the two molecules, thus providing a realistic estimate of the T7 unbinding force dependence, it is not a good system to evaluate the rebinding kinetics. From the Z-disk schematics of Fig. 34 it becomes clear that, after unbinding of T7, the EF3-4 gets released from load, in this way not undergoing forced unfolding. In the PullA-T7 geometry, on the other hand, both molecules are still under load after unbinding of T7, because of the inserted linker. The consequence is a rapid unfolding of the EF3-4, which greatly slows down the rebinding of the peptide (refolding is necessary before binding can occur). The passive-mode trace of Fig. 40 shows this effect: The FB state is populated about half of the time because of the long time spent by the system in the UU state.

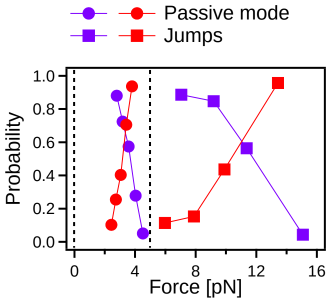

Fig. 46. Population probabilities obtained using the PullA-T7 constructs. Circle dots represent passive-mode equilibrium experiments, square dots come from jumps.

BOX 10. ESTIMATION OF THE MIDPOINT FORCE WITH THE JUMP ASSAY AND THE PULLA-T7 CONSTRUCT

A possible way to mimic the unforced refolding of the EF3-4 would be to jump to zero force after each unbinding. The jump assay presented in section 5.3 performs a similar task, since every 10 ms the system is driven to zero-force. Whenever at high force the rapid stepwise unbinding of T7 and unfolding of EF3-4 takes place, jumping at zero-load facilitates refolding and rebinding. The time trace shown in Fig. 42 already gives an idea of how the midpoint force could be shifted to higher forces in the physiological situation: at 11 pN the FB state is still poupulated half of the time (if the jumps are fast enough, one can assume that the black dots at zero-force have the same occupancies as the coloured dots at high forces). Fig. 46 compares the population probabilities obtained by passive mode and jump mode, from which it is possible to appreciate how the midpoint force shifts from 3.5 pN to 11 pN.

A better estimate of the midforce can be obtained by rapidly jumping to zero-force, in order to mimic force-free rebinding (Box 10). The limit of this assay is that both the EF3-4 and the T7 are released from load while jumping to zero force. In the physiological case (Fig. 34) it is possible that other bonds keep titin stretched even if a single Z-repeat detaches. Hence, releasing titin from load—as in the jump assay—may not be the best simulation of the real force propagation. A direct measure of the rebinding kinetics in a situation where the mere T7 is under load is dealt with in the next section.

5.7 PULLING ON TITIN T7 ONLY

To better assess the rebinding kinetics, it would be ideal to mantain the T7 peptide under load after unbinding, while releasing the EF3-4 from force. A possible way to mimic this situation—maintaining the linkage betweeen the two molecules—is to modify the PullA-T7 construct by exchanging one pulling site from the N-terminal domain of the α-actinin to the N-terminal of titin Z-repeat 7. In this construct, called PullT7 (Fig. 47), force is applied exclusively on the T7 α-helix. Such a system is expected to behave as a two-state system, where the only accessible transition is that between the FB and the FU states. The expected contour length increase corresponding to the unbinding and stretching of the T7 α-helix is only 4 nm.

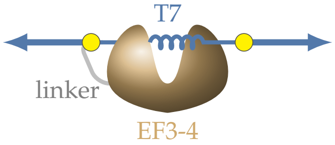

Fig. 47. PullT7 schematic. The pulling positions, marked as yellow dots, were changed in order to maintain only the T7 peptide under force.

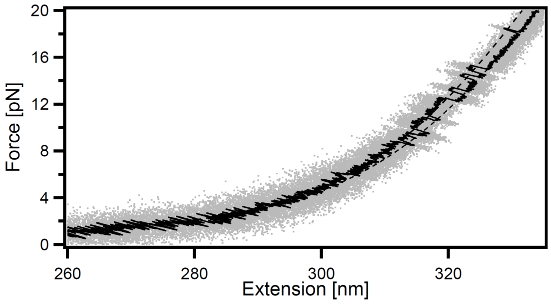

Fig. 48. Force ramp on the PullT7 construct at the constant speed of 20 nm/s. The unbinding and rebinding of T7 has a higher midpoint force. From this trace, WLC fits return a contour length gain of 3.8 nm.

Data coming from force ramps (Fig. 48) exhibit a marked increase of the unbinding forces, with detectable rebinding events until 18 pN. The measured CL gain is 4 ± 1 nm, perfectly compatible with the expected stretching of the α-helix.

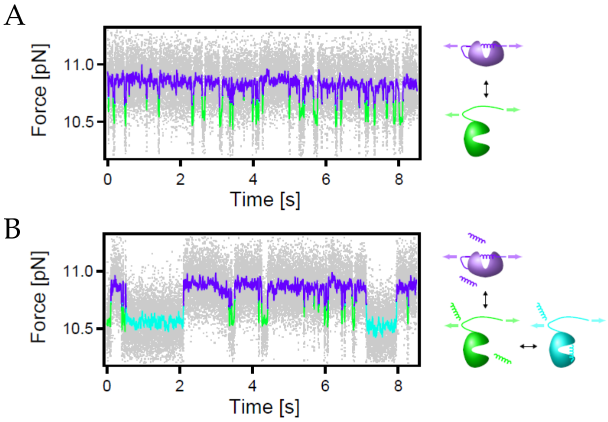

Fig. 49. Equilibrium experiments with the PullT7 construct, with the state network and the same colour coding as in Fig. 40. (A) Passive-mode trace, analyzed a two state system. (B) Competition assay, where binding from solution is separated from the FU state by dwell time threshold.

A wide force range (10 pN) was accessible to passive-mode experiments, an example of which is displayed in Fig. 49A. The state assignment was successfully carried out by applying a two-state HMM analysis, despite a separation of only 0.4 pN. The extracted rate constants and population probabilities as a function of force are plotted in Fig. 50.

The extrapolated zero-force transition rates are $0.6 \pm 0.3\,\mathrm{s}^{-1}$ for the unbinding and $216 \pm 106\,\mathrm{s}^{-1}$ for the rebinding, in good agreement with those measured with the PullA-T7 construct (Table 1). Moreover, the unbinding kinetics (purple branch in Fig. 50A) are compatible within errors with data coming from the N-C-termini geometry (Fig. 44B), importantly, in the whole force range. This observation justifies the acceptance of the midpoint force of the PullT7 construct (13 pN) as a good estimate of the physiological binding/rebinding equilibrium force.

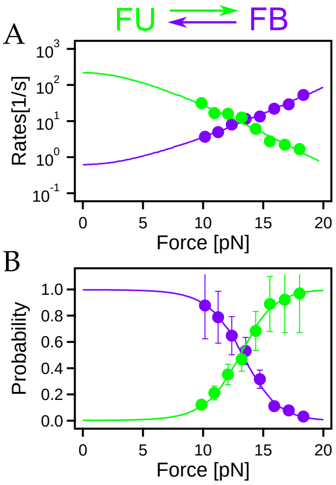

FIG. 50. Kinetics and occupancies for the PullT7 construct. (A) Rate constants vs. force, with the colour coding as in the schematic above the figure. (B) Occupancies vs. force. From a global fit, a binding free energy of $5.8\,k_\mathrm{B}T$ was obtained.

The competition assay can be carried out also with this construct. The binding from solution should appear at the same contour length of the unbound FU state. At sufficiently low forces the FU dwell times are short enough to be separate from the solution-binding events, as shown in Fig. 49B. The dissociation constant measured in this case is $8 \pm 4\,\mu\mathrm{M}$.

The kinetic and energetic values obtained from the different constructs, together with a correction discussed in appendix A.4, are summarised in Table 1.

TABLE 1. Zero-force rates and affinities obtained from the two different pulling geometries. A correction of the PullT7 data has been obtained as explained in appendix A.4.

Construct	K_D[μM]	k_off [1/s]	$\tilde{k}_\mathrm{on}$ [1/s]
PullA-T7	4.3 ± 2.1	302 ± 17	0.64 ± 0.06
PullT7	8 ± 4	216 ± 106	0.6 ± 0.3
PullT7 corrected	4 ± 2	432 ± 212	0.6 ± 0.3

5.8 SUMMARY

In this chapter the binding of the α-actinin EF3-4 domain and the titin Z-repeat 7 has been characterised, using two different pulling geometries in order to provide a consistent picture of how forces can be trasmitted in the Z-disk. The dynamics of this bond are very fast: Even in absence of external load, the bond has an average lifetime of less than 2 s. Nonetheless, the force dependence of the unbinding rates is very weak, due to the short distance between the bound state and the transition state (2 nm both in Fig. 44B for PullA-T7 and in Fig. 50A for PullT7). In the physiological range of forces to which a single titin molecule is subject (0–5 pN), the unbinding rates are almost constant.

The N-C-terminal geomtry (PullA-T7), despite correctly assessing the force-dependence of the unbinding rates, led to a very low estimation of the midpoint force (3.5 pN) for the EF3-4/T7 bond. The reason of such low unbinding forces has been identified in the non-physiological forced unfolding of the EF3-4 domain, which is subject to load even after unbinding of the T7 peptide. The slow refolding of the EF3-4, a necessary step to obtain rebinding of T7, slows down the overall rebinding kinetics, being completely unefficient at forces higher than few piconewtons.

This apparent contradiction of the bond not being able to substain physiological forces is resolved by a pulling geometry where the pure titin is stretched. The midpoint force for the PullT7 geometry is more than three times higher (13 pN), furthermore showing an almost constant rebinding kinetics in the physiological force range.

Despite the midpoint force increase obtained by changing the pulling geometry, a question persists: how can such a dynamic bond contribute to a long-term stability of the Z-disk? Every second, titin T7 is released from α-actinin, and a single bond clearly cannot provide anchoring for a sufficiently long time. In the next chapter, the mechanical stability of other titin Z-repeats will be treated. A kinetic model including the combined action of several titin/α-actinin interaction will be also discussed, in light of a possible long-term stability of this cluster of bonds.

6

α-ACTININ/TITIN INTERACTION: A CLUSTER OF BONDS

The measurements performed in this chapter aimed to understand whether the concerted action of many α-actinin/titin bonds could provide long-term anchoring of titin in the Z-disk.

The interaction between titin and α-actinin is not limited to the Z-repeat 7. As introduced in Sec. 4.4, other Z-repeats are able to bind one of the multiple α-actinin layers present in the Z-disk. Section 6.1 deals with the mechanical and kinetic characterisation of such bonds, by means of fusion construct similar to the PullA-T7 (see previous chapter). Thanks to these new data, it was possible to propose an avidity model, in order to explain the long-term anchoring of titin (6.2). Finally, some analogies with other muscles systems are discussed, in order to provide a more general picture for such networks, where a rapid exchange of the single components can be compatible with a long-term stability of the whole cluster (6.3).

6.1 INTERACTION OF α-ACTININ WITH OTHER TITIN Z-REPEATS

In human titin up to seven Z-repeats are present, whose affinity with the calmodulin-like domain of α-actinin has been already estimated in bulk [56]. The proposed spacing of α-actinin layers obtained by electron microscopy allows only each second titin Z-repeat to bind an α-actinin molecule [75]. Since the repeats T1 and T7 have been identified as the strongest binders, it is reasonable to assume that T3 and T5 are also good candidates to strengthen titin anchoring. In analogy with T7, described in chapter 5, fusion constructs resembling PullA-T7 have been prepared.[1] In the new constructs,

---

[1] In sections 5.6 and 5.7 the physiological relevance of the two different probed pulling geometries is discussed. The N-C terminal one (PullA-T7), employed for the other Z-repeats, is especially suited

Peptide	Sequence measured	ΔG [k_BT]	K_D[μM]	k_{off} [1/s]	k_{on} [1/s]
T7	`GKKAEAVATVVAAVDQARVREPR`	4.7	$4.3 \pm 2.1^{\#}$	302 ± 17	0.64 ± 0.06
T1	`ADKSAAVATVVAAVDMARVREPV`	5.9	$1.3 \pm 1.1^{\dagger}$	509 ± 97	0.46 ± 0.05
T3	`GTEKTFVPKVVISAAKAKEQET`	3.5	$14 \pm 11^{\dagger}$	158 ± 13	11 ± 10
T2	`EAEKIAVSKVVVAADKAKEQELK`	$<0.5^{*}$	$> 287^{\dagger}$	–	–
T5	`ETRKTVVPKVIVATPKVKEQDLV`	$<0.5^{*}$	$> 287^{\dagger}$	–	–
neck	`AEQAETAANRIVKVLAVNQENERLME`	0.7	$235 \pm 160^{\dagger}$	137 ± 6	40 ± 13

TABLE 2. Binding kinetics and free energy for different Z-repeats. Red amino acids in the sequences mark key hydrophobic binding positions of the Z-repeat α-helix, aligned as in [56] (in appendix C.3 the complete constructs sequences). In order to obtain the same effective concentration, every tethered peptide has been separated from the EF3-4 with the same number of amino acids. All binding energies come from fits to the probability vs. force plot, and the following symbols mark different methods: * = the folding free-energy of the EF3-4 sets a threshold for the detection of the binding events in the constructs where binding is not detectable. $^{\#}$ = from competition assay. † = calculated using Eq. 18. The interaction of the EF3-4 with the α-actinin neck (last row) is discussed in Sec. B.7.

the original T7 was substituted with either T1, T3, T5 and T2, the last one as a representative of (putatively) non-binding repeats. An overview of the results obtained with T1, T3 and T5 is given in Fig. 51, and the parameters are summarized in Table 2.

Fig. 51A depicts representative constant velocity traces. The visible transitions are FB → UU, i.e. combined unbinding of the peptide and unfolding of the EF3-4 domain, as for the PullA-T7 construct (Fig. 38). While T1 has a similar behaviour as T7, T3 shows lower unbinding forces, and T5 does not even show any observable binding. The repeat T2 shows the same exact behaviour of T5, i. e. no binding to the EF3-4 could be detected with this method. For T1 and T3, rapid refolding/rebinding transitions are also visible at the low pulling speed employed.

A closer look at passive-mode traces (Fig. 51B) reveals the same unbinding/unfolding pathway discussed for T7 (Fig. 40). Again, graphs referred to T1 resembles those obtained with T7, whereas T3 detaches more rapidly from the EF3-4. The kinetics of the PullA-T5 construct under passive-mode (last column) are perfectly compatible with transitions between UU and FU, i.e.

---

for the extraction of the correct force-dependent unfolding kinetics. Moreover, the extrapolated zero-force binding kinetics are in agreement with a second geometry (PullT7) where force is applied on titin only, technically more correct in evaluating the rebinding rates.

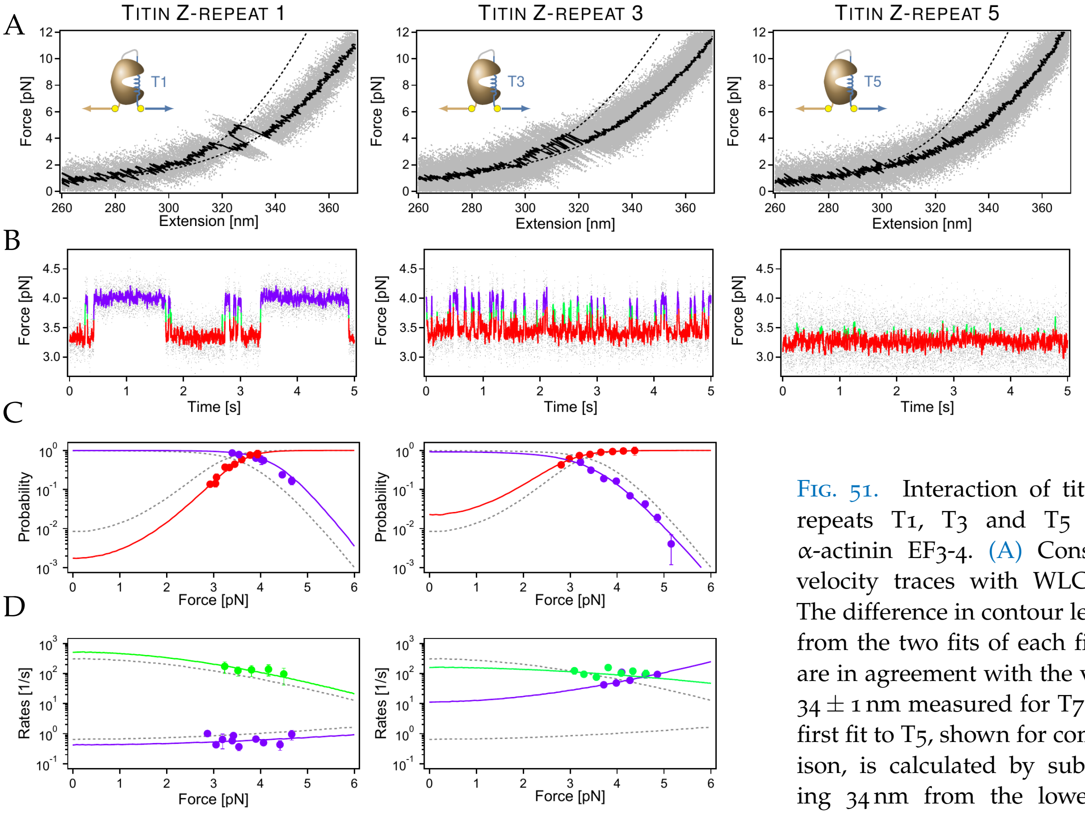

FIG. 51. Interaction of titin Z-repeats T1, T3 and T5 with α-actinin EF3-4. (A) Constant-velocity traces with WLC fits. The difference in contour length from the two fits of each figure are in agreement with the value 34 ± 1 nm measured for T7. The first fit to T5, shown for comparison, is calculated by subtracting 34 nm from the lower fit, the only one possible on this data set. (B) Passive-mode time traces excerpts of 5 s. (C) Population probability of the states UU and FB as a function of force. Solid lines are fit to the data, dotted grey lines are data from T7, for comparison. (D) Transition rates from FU to FB, depicting the binding (green) and the unbinding (purple) kinetics. As above, grey dotted lines come from T7.

mere folding/unfolding of the EF3-4 (for comparison, see data of the PullA construct in appendix A.2).

The analysis of several traces at different forces allows the extraction of the force-dependent population probabilities (Fig. 51C) as well as rate constants (Fig. 51D). The energy difference between the FB state and the UU state, as well as the zero-force rate constants, can be obtained from the plotted fits (Table 2). Overall, T1, T3 and T7 bind to the EF3-4 with similar mechanical strengths. The population probabilities of UU and FB (Fig. 51C) are slightly shifted toward higher forces for T1 (midpoint force of ~4 pN) and toward lower forces for T3 (~3 pN). The binding affinities K_D of the new peptides can be obtained by comparison with T7, for which both the free energy and the dissociation constant have been estimated in the previous chapter. Providing that the effective concentration of peptides is the same for all fusion constructs, the free energy of the repeat Ti, defined here as $\Delta G^0_{\mathrm{Ti}} = G_{\mathrm{UU}} - G_{\mathrm{FB}}$ can be related to the dissociation constant K_D^{Ti}, using Eq. 17:

$$\Delta G^0_{\mathrm{Ti}} - \Delta G^0_{\mathrm{T7}} = \ln\left(\frac{K_D^{\mathrm{T7}}}{K_D^{\mathrm{Ti}}}\right) \tag{18}$$

6.2 TITIN ANCHORING LIFETIME ESTIMATION

The experiments presented in the previous section include two more Z-repeats —T1 and T3— in the set of possible titin anchoring regions in the Z-disk. Together with T7, up to three Z-repeats are able to bind simultaneously to multiple α-actinin crosslinkers. This observation is compatible with the fact that several titin splicing variants are present in the different muscles of the body, and in humans T1, T2, T3 and T7 are always present.

From the collected data, a kinetic model can be obtained using an avidity argument (Box 11), in order to take into account the concerted efforts of these three regions. Titin will be bound to the Z-disk as soon as at least one bond is present. The arrangement of the involved molecules (Fig. 53) can help to understand the idea behind the cluster concept. The different α-actinin molecules are linked together by the actin filament; in analogy, titin Z-repeats are also connected, being part of the same molecule.

BOX 11. THE AVIDITY CONCEPT

The concept of avidity, or *multivalency*, has been introduced to explain how low-affinity inhibitors or antibody fragments ($K_D \sim \text{mM} - \mu\text{M}$) could cooperate and become high affinity ligands ($K_D \sim \text{nM}$) [62]. The ligands can be composed of multiple copies of the same sub-units (homo-multivalency) or of different sub-units (hetero-multivalency, Fig. 52). An example of homo-multivalency is the IgM, a pentameric antibody present in early stages of the immune response. The affinity of each fragment with the receptor is low, but the binding energies sum up, due to the multivalency of the cluster. The hetero-multivalency is certainly more general than homo-valency, but since the underlying principles are the same, the latter have been employed in the following estimations.

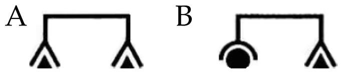

Fig. 52. The simplest multivalent system is formed by a bivalent ligand and two receptors. (A) Homobivalent ligand, which binds to the same kind of receptors. (B) Heterobivalent ligand, which binds to two different receptors.

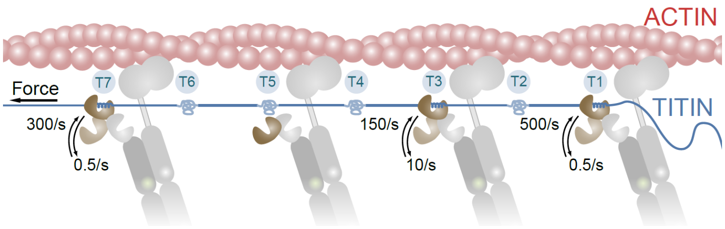

Fig. 53. Schematic of the molecules arrangement. Up to four Z-repeats can simultaneously bind to different α-actinin layers, but only T1, T3 and T7 have been found to have considerable binding affinities. Since α-actinin molecules are linked together via the actin filament, the cluster of bond may reach a long-term stability.

Let's first consider the zero-force situation. Each interaction has an unbinding rate of 0.5 to 10 /s and a rebinding rates of 150 to 500 /s. For simplicity, an average value will be assumed $\tau^{\text{off}} = 1\,/\text{s}$ for unbinding and $\tau^{\mathrm{on}} = 100\,/\mathrm{s}$ for rebinding. With these values, the probability of being unbound at any time is the ratio between the rates, that is $P_{\mathrm{unbound}} = 10^{-2}$. Considering only two Z-repeats, the first of them unbinds once per second from the EF3-4. Before rebinding takes place, the probability of finding the second unbound[2] is 1/100, meaning that on average 100 attemps (thus 100 s) are necessary to observe both Z-repeats unbound simultaneously. With n Z-repeats, the average lifetime of titin anchoring becomes

$$\tau^{\mathrm{off}}_{\mathrm{titin}}(F) = \frac{\tau^{\mathrm{off}}(F)}{\left(P_{\mathrm{unbound}}(F)\right)^{n-1}}, \tag{19}$$

where the dependence of force F is already included.

For $n = 3$ Z-repeats at zero force, the average lifetime would be 10 000 s, i. e. about 3 h. The tight titin/telethonin complex, despite not being strictly necessary for the Z-disk integrity (Sec. 4.3), links together two titin molecules, in this way increasing the number of connected Z-repeats up to $n = 6$. Even under the physiolgical upper force limit of 5 pN, the probability of being unbound as well as the off rate of a single repeat do not vary drastically (Fig. 50), and the cluster can hold for a long time.

In addition, other titin binding regions can cooperate to the anchoring of titin in the Z-disk. An example is the Zq region, that is positioned at the distal part of the Z-disk and interacts with the α-actinin rod [35, 133].

6.3 DISCUSSION AND OUTLOOK

Data from several FRAP (*fluorescence recovery after photobleaching*) experiments are available, that estimated the exchange rate of different Z-disk proteins. The majority of Z-disk components have a turnover of less than 1 minute [97, 112, 122], while the giant titin exchanges on average every 14 h [104]. The avidity concept is a intriguing hypothesis to explain how a long-term binding of titin can be achieved, while individual binding components can be dynamically exchanged.

Nature offers many other examples of systems where the accumulated strength of highly unstable interactions can lead to a stable cluster of bond. Without moving too far, the interaction of filamin with the von Willebrand receptor GP1b involves several dynamical bonds of linked sites, that can act together to provide a stable binding [99]. The anchoring of titin C-terminal in the sarcomeric M-band is also mediated by a pattern of 11 C-proteins regularly spaced over the myosin bundle. Altough no studies have been carried out on the dynamics of this bond, it is well known that titin is inextensible in the A-band [23, 50], meaning that an anchoring shared over many binding sites is a reasonable hypothesis.

---

[2] To avoid a continuus description, it is possible to think at 10 ms discrete time steps. Every 100 steps the first repeat detaches, and one time every 100 the second is also detached in the same time step.

Finally, the discussed model could be eventually applied to the specular contractile process. Upon active force generation, the scheme is completely symmetric to that of Fig. 34, but now force propagates through the actin filaments and α-actinin crosslinkers. Also a single α-actinin/actin bond is highly dynamic, with lifetimes in the order of a couple of seconds [26, 41, 84]. In the titin anchoring model, upon strech actin keeps α-actinin molecules at the right place after a single titin Z-repeat detaches. In a similar manner, it is possible that during contraction titin (not under load anymore) keeps α-actinin molecules in close proximity to the actin filament after they transiently detach. This could be another example of how fast kinetics can be compatible with stable crosslinking.

This study presents the first mechanical and kinetic results on the α-actinin/titin interaction. It would be interesting to validate some of the idea proposed here with *in vivo* experiments, e. g. using mouse knock-out mutants where the Z-repeats are removed. If the predictions discussed above are correct, the muscle is expected to developed uncorrectly, and eventually fall apart because of the absence of the titin restoring force.

6.4 SUMMARY

In the present chapter, a mechanical model of titin anchoring in the Z-disk is attempted. Up to seven Z-repeats can bind to α-actinin crosslinkers, only four simultaneously considering the spacing between the α-actinin layers. Other than T7, the four repeats T1, T2, T3 and T5 have been investigated in fusion constructs. T1 was shown to have a slightly higher mechanical stability than T7, while T3 a bit lower. T2 and T5 instead were not observed to bind the EF3-4 domain of α-actinin.

The concerted action of T1, T3 and T7 can lead to a long term anchoring of titin N-terminal, in the Z-disk. Owing to the linkage between the α-actinin crosslinkers, an avidity argument could be used. The binding energies sum up, and a simple formula for the overall titin unbinding rate can be obtained. Using only the three aforementioned binding regions, the calculated average lifetime of titin anchoring would be in the order of a few hours. Other interactions may help to increase the overall stability and match the measured titin turnover of about 14 h.

Part III

TALIN/INTEGRIN INTERACTION

7

INTEGRIN-MEDIATED FORCE TRANSDUCTION ACROSS THE CELL MEMBRANE

The correct force propagation between molecular components at the cell membrane is fundamental in many processes, such as cell migration, platelet aggregation and shape maintainance. These mechanisms rely on the spatiotemporal control of the connection between the cytoskeleton, the cell membrane and the extracellular matrix (ECM).

The key players in force transduction across the membrane are integrins, that need to be "activated" in order to simultaneously bind the cytoskeleton and the ECM (Sec. 7.1). The inside-out signalling pathway is thought to be initiated by the interaction with the cytosolic protein talin (7.2). A number of different isoforms of both talin and integrin allow the spatiotemporally controlled differentiation of tasks, but the binding constants never drop below tens of micromolar (7.3). How such a low-affinity interaction can promote reliable mechanotransduction across the cell membrane is still an open question (7.4).

7.1 INTEGRINS TRANSDUCES FORCE ACROSS THE MEMBRANE

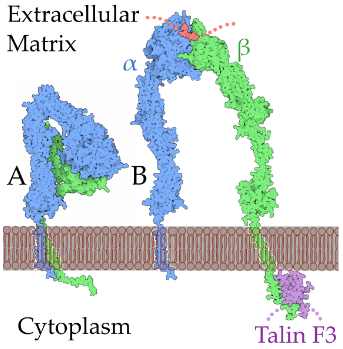

Fig. 54. Hypothetical illustration of the integrin activation process, by David Goodsell. Integrin α subunit is shown in blue, β subunit in green. (A) Closed/inactive structure of integrin. (B) Open/active state, in which the hetero-dimer can bind simultaneously cytoplasmic proteins, e. g. talin (whose N-terminal F3 domain is shown in purple), and extracellular proteins, e. g. a short peptide from fibrinogen (in red). The active structure was created by combining together the following pdb entries: 2vdo, 3fcs, 2k9j, 2h7d.

Integrins are heterodimeric proteins placed across the cell membrane, involved in the inside-out and outside-in mechanical communication. They are composed of two subunits α and β, for their majority formed by extracellular globular domains. The membrane-spanning part adopts an α-helix conformation, prolonged in the first 15 amino acids of the short cytoplasmic tail [3].

To regulate the interaction of the cell with the extracellular matrix, large conformational changes of integrin are involved, in a process named *integrin activation* (Fig. 54). The integrin αβ complex can exist in at least two conformations, an inactive/closed one (Fig. 54A), curved towards the membrane, and an active/open one (Fig. 54B), where the protein can bind both cystoplasmic and extracellular proteins. This process can arise from either the outside of the cell, e. g. in response to changes in the ECM mechanical properties [12], or from a signal inside the cell, e. g. to initiate platelet aggregation and promote blood clots [69]. The two short integrin α and β tails play a key role in the inside-out activation process: The integrin activation is thought to be initiated inside the cell, where the interaction between the tails is disrupted, leading to their separation and subsequent structural rearrangment outside the cell [3].

7.2 INTEGRIN/TALIN INTERACTION

Although a range of binding partners have been identified, including filamin and kindlin, the inside-out activation of integrins is achieved by the binding of talin [115], a big cytoplasmic protein (250 kDa) which tethers the actin network to the membrane (Box 12).

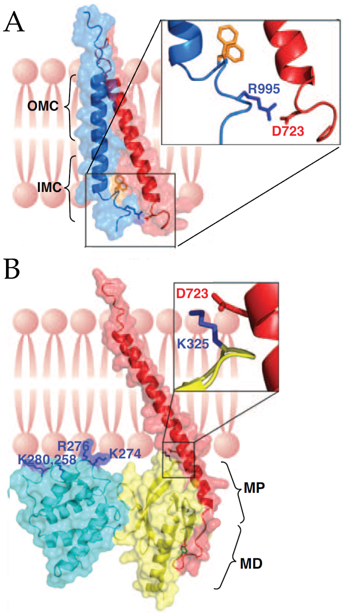

Fig. 55. Structural basis of integrin interaction. Adapted from [3]. (A) the α (in blue) and β (in red) tails can form a salt bridge in the closed conformation of integrin. (B) Binding of talin (F2 in cyan, F3 in yellow) to the β tail can disrupt the salt bridge and initiate integrin activation. The F2 domain stabilises talin anchoring, thanks to four charged amino acids that bind to the membrane.

BOX 12. TALIN

Talin is an ubiquitous cytosolic protein that is part of the *focal adhesion* macromolecular assembly. The main task of talin is to connect the membrane-spanning protein integrin with the cytoskeleton, in particular to actin. Talin can be divided into two parts, an N-terminal head region and a C-terminal rod region, at the end of which there is an actin-binding domain. The head region is a FERM domain composed of four subdomains (F0–F3). The N-terminal one (F3) is the minimal subunit able to activate integrin [17], probably disrupting a salt bridge between the α and β tails (Fig. 55A). The talin FERM domain can directly bind the cell membrane, through a positively charged patch on the surface of F2 [57]. The mutation of four charged amino acids in F2 (Fig. 55B) is sufficient to disrupt this bond [4].

The cytoplasmic tail of integrin binds the N-terminal talin F3 domain in two regions, the membrane proximal (MP) part—which is the prolongation of the transmembrane α-helix—and the membrane distal (MD) part, in particular at the NPxY motif (Fig. 55B).

Structural studies on the integrin/talin complex were lacking until a few years ago, mainly because of the weak nature of the binding [4]. The available data have been obtained thanks to workarounds which increase either the effective local concentration—by linking the proteins via a coiled-coil [31]—or the affinity—by creating chimaeric peptides [127]— until the discovery of high-affinity isoforms allowed a better understanding of the integrin activation process [4].

Other proteins may be involved in integrin interaction and the overall stability of the integrin/talin complex, by anchoring talin at the membrane. The talin F2 domain has been shown to bind the membrane by means of four charged amino acids [57]. Moreover, a RAP-mediated protein called RIAM binds both talin F3 and the membrane, which may assist talin anchoring [130]. Another membrane protein, kindlin, binds to the last 10 amino acids of integrin tails, cooperating with talin in the integrin activation process [118].

7.3 INTEGRIN AND TALIN ISOFORM SPECIFICITY

A variety of integrin isoforms are present in our bodies, together with two talin isoforms [85]. In mammals, the integrin α and β subunits are expressed in 18 and 8 different isoforms respectively and assembled in 24 unique αβ dimers [52]. Each combination has a variable specificity for different substrates, fine-tuned by small differences at the sequence—and hence structural—level. The complexity is increased considering spliced variants. β1, for example, has 4 splice variants, β1A–D.

Many of these isoforms have been studied in bulk experiments. The highest affinity was found between β1D and Talin 2, isoforms predominantly expressed in striated muscle cells. In particular, they co-localise in myotendinous junctions [13, 128], where high forces are involved during muscle contraction. Talin 1 instead pref-

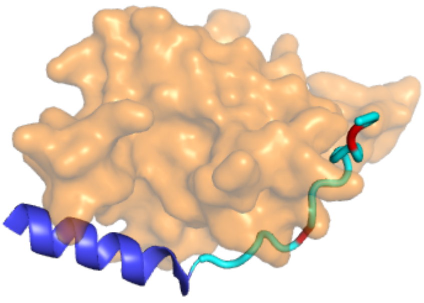

```
β1D   HDRREFAKFEKEKMN AKWDTQENPIYKSPIN NFKNPNYGRKAGL
β1A   HDRREFAKFEKEKMN AKWDTGENPIYKSAVT TVVNPKYEGK
      |               |     |       |
      758             773   778     786
```

Fig. 56. Structure of the talin F3 domain (orange) in complex with the integrin β tail (MP in blue, MD in cyan) [4]. Below, difference in sequence between integrin cytoplasmic tails β1A and β1D. The non-structured region is depicted in grey, the non-conserved residues are underlined and the two crucial residues are marked in red.

erentially binds the splice variant β1A, although with very low affinity (Table 3).

It is interesting to note that the splice variants β1A and β1D have substantially different binding affinities with talin, although the main differences in the sequences are in the C-terminal region, involved in kindlin binding (Fig. 56). To explain this observation, a set of site-directed mutageneses have been performed together with structural and affinity analyses [5]. Anthis *et al.* showed that the `E778` (`G` in β1A) residue alone accounts for 35 % of the difference in affinity between β1A and β1D, while the rest is almost entirely (56 %) provided by the `P786` residue (`A` in β1A).

	talin1	talin2
β1A	490 ± 10	652 ± 20
β1D	95 ± 4	36 ± 2

TABLE 3. Binding affinities between talin 1 and 2 isoforms and β1A and β1D integrin splicing variants. [4].

7.4 OPEN QUESTIONS

A comprehensive understanding of the integrin activation process has been hampered by the low affinity of the talin/integrin bond, in combination with the intrinsic difficulties in studying transmembrane proteins.

The recent review of Sun *et al.* summarizes the main open questions regarding the integrin activation process [113]. From a mechanistic point of view, the most intriguing mystery is "how the low affinity of the talin-integrin tail interaction is able to transmit [. . .] forces" [113]. A fascinating phenomenon that may answer this question is the counter-intuitive increase of the bond lifetime upon load, called *catch bond*. Such a behaviour has been observed in a number of adhesive proteins [119], including integrins [61]. A common motif in catch-bonds is the presence of some additional binding site, hidden in the structure and exposed when force is applied.

The kinetic and mechanical quantities involved in talin/integrin bonds have not been investigated to date. The MP region of the integrin tail does not seem to contribute to the stability of the bond, since it is shared by the β1A and the β1D isoforms, but the former has a weak sub-millimolar affinity with talin. Nonetheless, the binding of the MP region with talin is supposed to separate the α and β subunits in the integrin activation process. Direct mechanical measurements can be used to study the force-dependence of the bond lifetimes, in order to test the possibility of avidity or catch-bond effects, and assess the mechanical stability of the different integrin regions.

8

TALIN/INTEGRIN INTERACTION

Among the number of different isoforms of talin and integrin, of particular interest is the comparison between β1A and β1D, two splice variants of the β1 subunit (Sec. 7.3). β1D binds the talin 2 muscle isoform with the highest reported affinity (Table 3), while β1A preferentially binds talin 1. In this chapter, the talin 2/β1D and the talin 1/β1A interactions are investigated, using the tools presented in the methods (Sec. 2.6).

Fusion constructs were prepared (Sec. 2.2), named T1-β1A and T2-β1D, in order to evaluate the binding mechanics and kinetics.[1] The pulling position has been chosen in order to simulate the load propagation in the cell. Upon anchoring of talin at the membrane—mediated by integrin tail binding—the force is transduced through the N-terminal of talin on one side, and on the N-terminal of integrin on the other side. In order to enable force to be applied at these two sites in the experimental setup, cysteine residues (Sec. 2.5) were placed at the two positions shown in Fig. 57. Sections 8.1 and 8.2 deal with the force response of the aforementioned fusion constructs. To explain the measured noncanonical force dependence of the unbinding rate constants and the binding energies, two lines of research were followed, the first in 8.3 and 8.4, the second in 8.5 and 8.6. The acquired data are discussed and summarised at the end of the chapter (8.7).

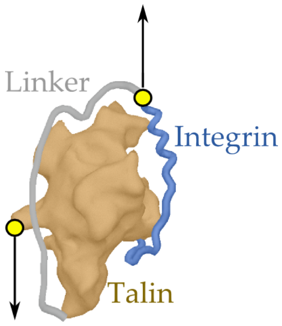

Fig. 57. Structure of the fusion construct. Talin F3 domain and integrin β1 are based on [4]. A linker is added, whose structure was modeled with the software Coot. Yellow dots mark cysteines, inserted for load application.

8.1 T2-β1D AND T1-β1A FORCE RESPONSE

Upon load application, the two constructs T1-β1A and T2-β1D show remarkably different behaviours. Force-extension traces of T2-β1D (Fig. 58A) depict rapid near-equilibrium transitions at 5–10 pN, and a second event at about 20 pN. Worm-like chain fits (Sec. 3.2) reveal a contour length gain of 8.2 ± 0.3 nm for the first transition, in good agreement with unbinding and rebinding

---

[1] The sequences of all constructs presented in this chapter can be found in appendix C.4.

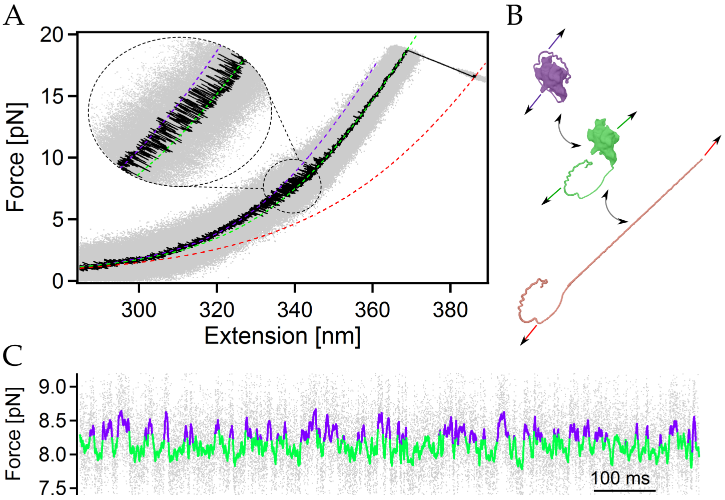

Fig. 58. T2-β1D under force. (A) Force-extension curve, showing two unfolding events. The flipping at 5–10 pN (zoom in the inset) corresponds to unbinding/rebinding of β1D, and the high-force event to talin unfolding. (B) Kinetic network expected in this pulling geometry. (C) Passive-mode trace excerpt of 1 s at an average preload of 8.3 pN. HMM analysis (always applied on unfiltered data) allows assignment of the data points to bound (purple) or unbound (green) states, according to the schematic in *B*. Smoothed trace is coloured, for clarity.

of the integrin tail from the talin domain (expected CL gain of 8.5 nm), while the high force event can be interpreted as the unfolding of talin (measured CL gain of 32.5 ± 0.4 nm vs. expected value of 33.0 nm). The kinetic network of Fig. 58B shows that, in the chosen pulling geometry, it is not possible to force unfolding of the integrin tail. Hence, the absence of signal hampers any evaluation of the folding behaviour of integrin when detached from its substrate.

On the other hand, only a single event can be detected in T1-β1A force vs. extension data (Fig. 59), with a CL gain compatible with talin 1 unfolding. In this case, the talin/integrin bond is too weak to be properly detected. Nonetheless, a single WLC curve does not fit the graph in the low-force region, suggesting the presence of a "shoulder" in the signal at forces about 3–5 pN. The two close fitting lines in Fig. 59 are obtained by fixing the expected CL gain to a value of 8.5 nm.

To get more insights into the fast low-force kinetics, a standard deviation analysis has been performed, as suggested in [6]. Fast transitions between two states increase the standard deviation of the signal, if compared to the behaviour of pure DNA (inset of Fig. 59). A small peak is present in the data of the T1-β1A construct, suggesting fast binding/unbinding kinetics at about 5 pN. However, it is hard to extract more information from such a weak bond.

The rest of the chapter deals with a more detailed investigation of the talin 2/β1D interaction.

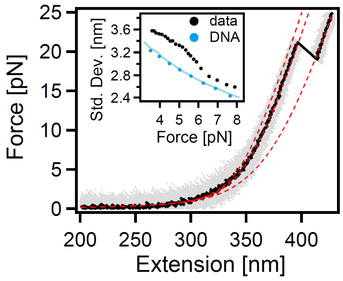

Fig. 59. Constant-velocity trace of the T1-β1A construct. The first WLC curve is not a real fit, but is calculated to obtain the expected CL gain of 8.5 nm, to guide the eye. (*inset*) Standard deviation analysis. Each dot corresponds to a passive-mode trace, whose SD is plotted as a function of the average force. Black dots are data of T1-β1A, while the cyan dots and the cyan line come from a pure DNA molecule, without any protein contribution (a slightly different trap stiffness was used for that measurements) [6]. The increase in SD at 5 pN in T1-β1A data indicates possible ultra-fast binding/unbinding transitions, that cannot be separated by the HMM analysis.

8.2 T2-β1D FORCE-DEPENDENT KINETICS

Using preloads in the range of 5–12 pN in passive mode (Sec. 3.3) and of 12–18 pN with the jump-assay (Sec. 3.4), the force-dependent kinetics of T2-β1D could be evaluated with better precision.

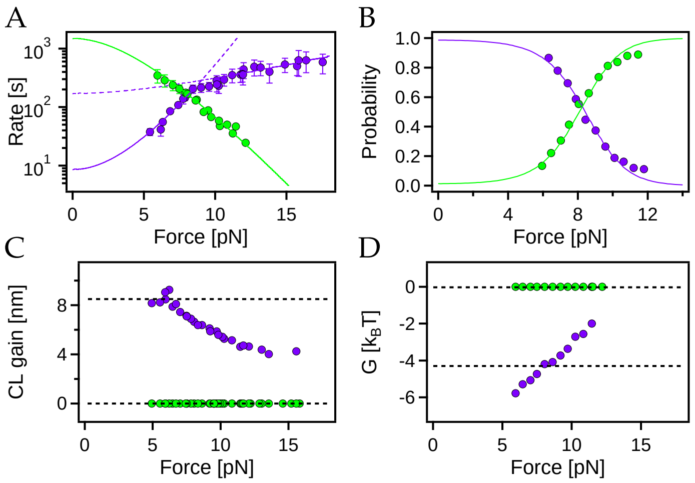

Fig. 60. Binding energy and kinetics, from T2-β1D. (A) Unbinding (purple) and rebinding (green) rates. Two different fits (Berkemeier-Schlierf model) have been performed, resulting in k_{off} of $(1.7 \pm 1.0) \times 10^2$ /s and 8.4 ± 1.6 /s, before and after 9 pN. A single fit describes the rebinding kinetics, with $\tilde{k}_{\text{on}} = (1.5 \pm 0.2) \times 10^3$ /s. (B) Occupancy vs. force plot, whose global fit returns a binding free energy of $4.3\,k_B T$. (C) Force-dependent CL gain. A dotted line marks the expected 8.5 nm gain. (D) Binding free energy. A dotted line marks the value of $4.3\,k_B T$ extracted from the occupancies.

A two-state system HMM analysis can be performed (Fig. 58C) in order to assign the data to the bound or unbound states, coloured respectively in purple and green in Fig. 58B. The unbinding rate, plotted vs. force in Fig. 60A (purple dots), has a non-canonical force dependence: A single fit with the Berkemeier-Schlierf model (Sec. 3.3) does not properly interpolate the data in the whole force range, because of a kink around 9 pN.

Even more exceptionally, the binding free energy, as well as the contour length gain, vary monotonically with the preload (Fig. 60C–D).

The reason for such a divergence from a typical two-state kinetic network can lie in several effects. Two lines of research will be discussed in the next sections.

8.3 TWO-BINDING-MODE HYPOTHESIS

The first hypothesis that can be proposed to explain the data shown in Fig. 60 is that the unbinding of integrin from talin (and/or the rebinding) takes place in two steps, namely a two-state system is not suited to describe such a protein/protein interaction. The force dependence of the unbinding rate has been shown to be bimodal for the biotin/streptavidin bond [83] (Fig. 61), as well as for the digoxinenin/anti-digoxigenin one [105]. The reason for such behaviour has been ascribed to a three-well potential, i.e. to a two-step unbinding pro-

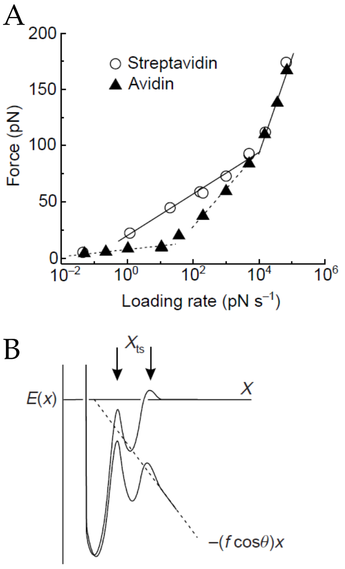

Fig. 61. Unbinding of the biotin/streptavidin bond [83]. (A) Unbinding force of two different avidin bonds as a function of the loading rate, in constant-velocity AFM experiments. The expected exponential dependence (a line in the log scale) is broken, with one (streptavidin) or even two (avidin) kinks. (B) Two-barrier energy landscape, which can explain the variation of the force/rate slope at different loading rates.

cess. A similar argument can be used to explain why at different preloads the slope of the rate vs. force plot varies.

To support this hypothesis for the talin/integrin complex, a structure-function analysis [127] suggested a two-step binding where the α-helical MP region of integrin is recruited only after the MD part has bound talin (Fig. 62). A test of this hypothesis could be performed with a three-state HMM analysis of the passive-mode traces (Fig. 58C), but the fast kinetics and the small force separation between the bound and unbound states make such an analysis very challenging. In the next section, a more reliable strategy is presented.

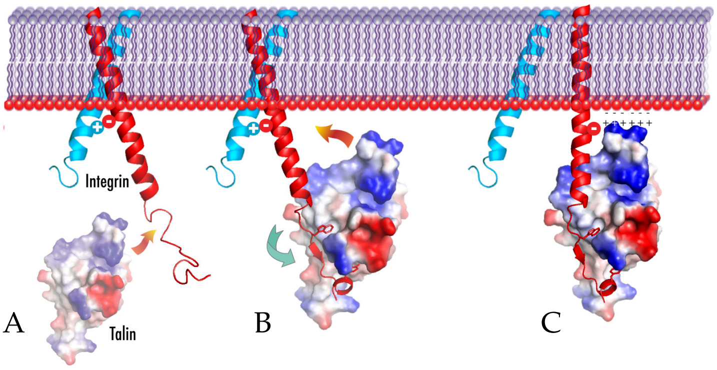

Fig. 62. Model of two-step talin anchoring at the cell membrane [127]. (A) Unbound talin F3 gets in proximity of the surface. (B) The talin F3 is first recruited by the membrane distal (MD) part of the integrin tail. (C) Afterwards he interaction with the membrane proximal (MP) α-helix is established, distrupting the salt bridge between the α and β monomers of integrin.

8.4 A CONSTRUCT LACKING THE MP α-HELIX

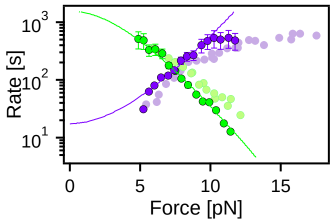

Fig. 63. Binding (green) and unbinding (purple) rates of the T2-β1D_noMP construct, lacking the MP part of integrin. Light-coloured rates are those reported in Fig. 60A (native integrin), for comparison. The binding rates are well described by the Berkemeier-Schlierf model, with $\tilde{k}_{\text{on}} = (1.5 \pm 0.2) \times 10^3\,/\text{s}$ in agreement with the native construct. The unbinding rates are still bent, as in the native construct. For comparison, a fit from point 3 to 13 has been carried out, resulting in $k_{\text{off}} = 17 \pm 2\,/\text{s}$.

To test the hypothesis that two binding steps are involved in the talin anchoring process, a mutant was designed (T2-β1D_noMP), where the first 15 amino acids of the integrin tail—the α-helical MP region—were substituted with a non-interacting sequence, i. e. a combination of glycines and serines. If the binding of the MP and MD integrin regions are independent and of comparable mechanical stability, a single binding step should be observed, since in the mutated construct the second binding step (Fig. 62C) should be absent.

The mutant lacking the α-helix does not show any relevant difference with the T2-β1D construct. The force dependence of unbinding rates (Fig. 63), the CL gain and the binding free energy are compatible with the wild-type β1D. This results clearly shows that the MP region does not have a high mechanical stability, and the binding energy is entirely provided by the MD part.

However, the two-step hypothesis cannot be completely ruled out. Stepwise binding can still take place in two different parts of the MD region.

8.5 LINKER-EFFECT HYPOTHESIS

A second possibility to explain the non-canonical force dependence of the kinetics is an incorrect estimation of the force applied to the bond. The linker between the proteins employed in the fusion contructs—whose structure was modeled in Fig. 57—has a contour length of 9.8 nm and an end-to-end distance at rest of 5.5 nm. From Eq. 2, the force necessary[2] to stretch a protein backbone by a distance half of its CL is 10 pN, meaning that, even in the absence of any external load, the bond is subjected to a high tension, applied from the entropic linker spring. Moreover, the mutant explored in the previous section showed that the α-helical MP part of the integrin tail does not tolerate high forces, thus it will be likely unfolded considering such high pretensions.

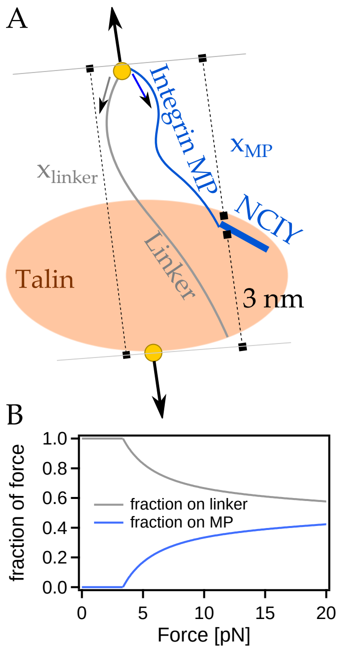

FIG. 64. Simulation of the effective force applied to the bond in the T2-β1D construct. (A) Schematic of fusion construct (colour coding as in Fig. 57). The integrin MP part is supposed to be unstructured in the current conditions, while the binding to talin is entirely provided by the NCIY motiv. The contour lengths are $CL_{linker} = 9.8$ nm and $CL_{MP} = 5.5$ nm, while the distance between the linker anchoring point and the NCIY motif is 3 nm. The persistence length was fixed to 0.7 nm. (B) Fraction of the total force applied on the linker and on the MP (thus on the bond), for a one dimensional model.

BOX 13. SIMULATION OF THE LINKER STRETCHING

Fig. 64A depicts a sketch of the fusion construct, with the MP α-helix unfolded. A simple one-dimensional model can be developed to calculate the fraction of force applied to the linker and to the bond. Each flexible region follows the force-extension WLC model in Eq. 2. Given the contour length of the linker and the MP, it is possible to calculate the fraction of force carried by the MP, thus acting on the bond, plotted in Fig. 64B as a function of the total applied force.

The most interesting feature of the graph is that the fraction of force on the MP (blue curve) has a high force dependence in the 5-10 pN range, while it gets flatter at higher forces. The force applied to the bond is underestimated in the whole force range, but the error is significantly more pronounced at low forces. Interestingly, the curve has the same concave shape as that of the unbinding rates (Fig. 60A), indicating that the strong force dependence at low forces could be related to the high slope of the plot in Fig. 64B. Although the present model does not fully account for the bending of the data, it points towards the right direction, showing how the linker can play a critical role in the study of a protein/protein interaction.

One of the basic conditions that allow the investigation of a protein/protein interaction with fusion contructs is that the linker must not hold any load (Sec. 2.2). If the applied force is shared between the linker and the bond under study, the force values of Fig. 60 are not corrected, because only a fraction of that force is really applied to the bond. A simple model to explain this effect is described in Box 13.

---

[2] For this estimation, a persistence length of 0.7 nm was employed.

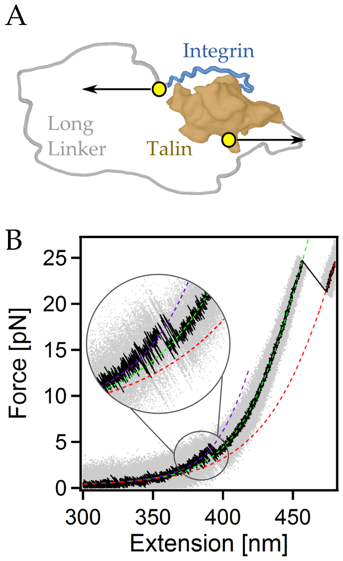

Fig. 65. Long-linker construct T2-β1D_LL. (A) Schematic of the long-linker fusion construct. (B) Force-ramp trace. The binding/unbinding transitions are below 5 pN, while talin unfolding is visible at high forces. The CL gain of the flipping is 25.1 ± 0.7 nm, close to the expected value of 24.3 nm.

8.6 A CONSTRUCT WITH A LONGER LINKER

In order to cancel the influence of the linker, a new construct was designed—named T2-β1D_LL—where a longer linker sequence[3] was employed to connect talin 2 and β1D (Fig. 65A). A force-extension trace obtained at the constant velocity of 50 nm/s is shown in Fig. 65B. The bond breaks apart at lower forces compared to the short-linker construct, about 4 pN, while the unfolding forces of talin are unvaried.

The shift to lower forces can be explained by the combination of two effects. The first, affecting the on-rates, is the drop of the effective concentration of the ligand, due to the longer linker length.[4] The second is a pure energetic consideration. The energy is proportional to the force times the length change. If similar binding energies are involved, the longer the length increase, the lower the equilibrium force.

The analysis of passive-mode traces enables the tracking of the force dependence of the kinetic and energetic quantities, as done in Fig. 60 for the short-linker version. The data of the long-linker variant are summarised in Fig. 66. Both extracted on- and off-rate constants (Fig. 66A) are now well described by the Berkemeier-Schlierf model. The on-rate have a higher slope because of the longer linker, while the extrapolated zero-force value is compatible with the short-linker construct. The off-rates deviate from the short-linker rates below 7 pN, while at high forces they are compatible.

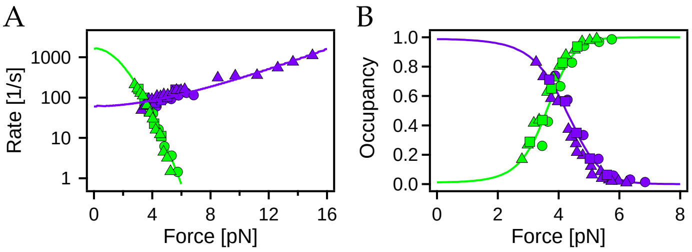

Fig. 66. Binding energy and kinetics T2-β1D_LL construct (data from three different molecules are overlaid). (A) Unbinding (purple) and rebinding (green) rates. Both the unbinding and the rebinding kinetics can be described with a canonical two-state system ($k_{\text{off}} = 60 \pm 2$ /s and $\tilde{k}_{\text{on}} = (1.6 \pm 0.4) \times 10^3$ /s). Above 7 pN, the unbinding rates were obtained with the jump assay (Sec. 3.4). (B) Occupancy plot, whose global fit returns a binding energy of $3.8\,k_{\text{B}}T$ (the error on the free energy is about 10 %, see Sec. 3.3).

---

[3] The long linker has 78 amino acids, thus is almost three time longer than the previous one, which involved only 27 amino acids.

[4] If the linker length is doubled, the effective concentration roughly drops by a factor of $2^3 = 8$, since it is a volume-filling effect (see Sec. A.3).

The binding energy, extracted from the occupancies of Fig. 66B, is $3.8\,k_{\mathrm{B}}T$, slightly lower than that obtained with the short-linker construct. The zero-force rate constants can be used as a control for the binding energy, since $\ln(\tilde{k}_{\mathrm{on}}/k_{\mathrm{off}}) = \Delta G/k_{\mathrm{B}}T$ (Eqs. 3 and 12). The value obtained from the rates is $3.4 \pm 0.9\,k_{\mathrm{B}}T$, compatible within error with the previous estimation. The force dependence of the CL gain and the binding energy are constant in the whole probed force range.

An analogous fusion construct of talin 1 and β1A connected by a long linker has been tested, but no binding/unbinding signal could be detected, as in the short-linker version T1-β1A.

8.7 DISCUSSION

In this chapter, the first evaluation of the binding properties of the C-terminal domain of talin to the cytoplasmic tail of integrin was performed. Two pairs of isoforms has been tested, the weak talin 1/β1A interaction, involved in many cell motility processes, and the strong talin 2/β1D bond, specific for the myotendinous junctions. Both interactions have been previously studies in bulk, and the affinities evaluated. A set of point mutations revealed how a few differences in the β1A and β1D sequences could lead to a tenfold increase in affinity.

A first pair of fusion constructs, T1-β1A and T2-β1D, was tested. The binding energy of talin 1 and β1A was too weak to extract quantitative kinetic or energetic information, since the unbinding takes place in a force range below the resolution of the setup. However, talin 2 and β1D showed fast transitions between the bound and unbound states, with a midforce of 7 pN. The fact that the talin 2/β1D complex can resist higher forces is consistent with the need of connecting myocytes with tendons, where forces are higher compared to non-muscle cells. The binding kinetics could not be described by a canonical two-state systems, thus two lines of study were carried out to understand this effect.

The first hypothesis was a two-step binding process, corroborated by previous structural studies that suggested a later binding of the integrin membrane proximal α-helix. A mutant lacking the MP region was created and measured, but no noticeable difference could be observed compared to the wild-type tail. This result is interesting by itself, as it shows that the α-helix, which is supposed to play a key role in the integrin activation process is not binding tightly to talin. This is in agreement with the fact that the MP region of integrin has the same sequence in β1A and in β1D, but β1A has a much lower affinity to talin. Hence, the MP part does not have a measurable mechanical stability, raising the question of how talin can compete with the α tail of integrin and disrupt the salt bridge between the α and β tails.

The second hypothesis was an influence of the linker connecting the two proteins in the fusion construct. The length of the linker was too short to safely assume that the force applied by the trap was the same as the one felt by the bond. A mutant with a longer linker was designed, showing canonical two-state kinetics. The midpoint force dropped to 4 pN, because of the lower effective concentration, which is a direct consequence of the longer linker. The unbinding rates are fast ($\sim$ 100 /s) across the whole force range explored, meaning that a single bond cannot last longer than a fraction of a second even in the absence of force. In analogy with the α-actinin/titin interaction discussed in chapters 5 and 6, it is intriguing how such a dynamic bond can tightly connect myotendinous junctions. Most likely, other interactions between the talin/integrin complex and the membrane could stabilise this bond, and an avidity effect may be involved also in this case.

The standard two-state behaviour of the long-linker construct also rules out the hypothesis that a catch-bond behaviour is involved in the talin F3/integrin β1 interaction. The addition of other talin domains to the fusion construct could increase the probability of observing a catch-bond.

8.8 SUMMARY

In accordance with the low affinities measured in bulk for different talin and integrin isoforms, the mechanical stability of this complex is very low. Only the talin 2 and the integrin β1D tail isoforms showed detectable binding when a load is applied to a fusion construct, as expected for their role in connecting neighbouring cells in muscle fibers. However, even the strongest interaction cannot last more than a fraction of second, showing that additional elements must contribute to the tight anchoring of the cytoskeleton at the membrane. Additional experiments prove that the membrane proximal region of the cytoplasmic integrin tail is not able to resist significant load, thus diminishing the key role assigned to this region in the integrin-activation process.

9

BINDING AFFINITY AND OUTLOOK

The experiments performed in the previous chapter do not allow the extraction of the binding affinity, nor the binding kinetics. The pseudo first-order $\tilde{k}_{\text{on}}$ obtained from the fusion construct—thus the measured binding energy—depends on the effective concentration of one molecule, in this case integrin, which is related to the linker length, thus are not a good estimate of the binding kinetics. To circumvent this limitation, a competition assay can be employed to determine the dissociation constant K_D and the on-rate k_{on} (Sec. 3.5).[1]

In Sec. 9.1 the binding affinity of an integrin β1D mutant with high affinity for talin is evaluated,[2] as a control for the competition assay. An important issue for the evaluation of the competition data is further discussed (9.2). The native peptide β1D is further employed in the same assay (9.3) Some of the possible experiments, that can be performed with the toolkit presented in this and in the previous chapters, are listed in the outlook (9.4).

9.1 AN INTEGRIN MUTANT HAS A HIGH AFFINITY WITH TALIN

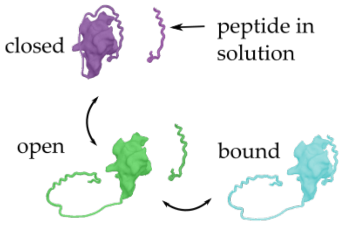

Fig. 67. Kinetic network of a competition experiment. If the same binding site is shared by the tethered and the solution peptides, competition is established, and the open state is an obligatory on-pathway intermediate for all exchanges.

An interesting mutant, called β1D_V, was employed as a control for the robustness of the competition assay. Thanks to the subsitution of three amino acids (`D776–Q778`) with a single valine residue, the integrin tail has a 1000-fold higher affinity with talin 2 ($K_D = 0.02\,\mu\text{M}$) [5].

If a competition experiment is performed, the expected kinetic network is the one shown in Fig. 67. The previous two-state system composed of the bound and unbound states of the tethered peptide (Fig. 58C) is now extended to account for the binding of the solution peptide. Since the fusion construct is only used as a detector, the original states were renamed as *open* and *closed*, and from now on binding is always intended to occur from solution.

---

[1] Since the fusion construct is used as a pure detector, the outcome of these experiments should not be affected by the linker length. The T2-β1D construct (Fig. 58) was employed for the following experiments.

[2] The sequences of all constructs presented in this chapter can be found in appendix C.4.

The addition of 1 µM of the β1D_V peptide to solution (Fig. 68) leads to long-lived events (coloured in cyan) at the same force level as that of the open state. These dwell events correspond to binding of β1D_V from solution, since this peptide shares the same binding site as the tethered peptide, and can bind only if the fusion construct is open (see Fig. 67 and Sec. 3.5). The whole passive-mode trace (150 s) is depicted in Fig. 69B, where for simplicity only two phases were considered, the high-noise unbound phase (purple) and the low-noise bound phase (cyan), as in the schematic of Fig. 69D.

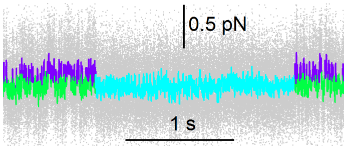

Fig. 68. Short excerpt of a passive-mode trace (preload about 8 pN) in presence of 1 µM β1D_V peptide in solution. The colour coding corresponds to the kinetic network of Fig. 67.

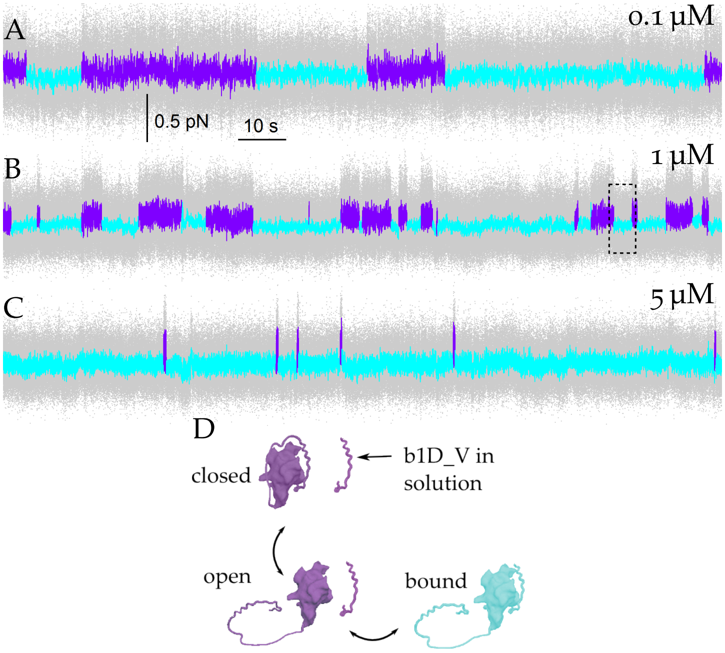

Fig. 69. Competition assay with the peptide mutant β1D_V, at a preload of 8 pN. (A–C) Passive-mode traces of 150 s (full-length traces can last as long as an hour) with the addition of 0.1 µM (in *A*), 1 µM (in *B*) and 0.1 µM (in C) of the β1D_V peptide in solution. The colouring have been manually applied to high (purple) and low (cyan) noise regions. The dotted box in *B* is the region zoomed in Fig. 68. (D) Kinetic network in the presence of solution peptides. The binding from solution takes place in the open state, since the tethered (β1D) and the solution (β1D_V) peptides share the same talin binding site.

The average lifetime of the bound cyan state directly leads to the off-rate of the β1D_V, whereas to calculate the on-rates one has to consider that the sole open state is competent with binding the peptide from solution. In Fig. 69B, the preload is such (8 pN) that the open and closed states have the same occupancies (zoom in Fig. 69D). Hence—as first discussed in [99]—to obtain the pseudo first-order on-rate $\tilde{k}_{\text{on}}$, the purple dwell events τ_{on} of Fig. 69B must be multiplied by the open probability P_{open} measured in absence of solution peptide, i. e. only considering the flipping open↔closed

(Fig. 69D, in this case about 50 %). The on-rate k_{on} can be calculated as

$$k_{\mathrm{on}} = \frac{1}{\tau_{\mathrm{on}}(F, [\beta 1\mathrm{D\_V}]) \cdot [\beta 1\mathrm{D\_V}] \cdot P_{\mathrm{open}}(F)}. \tag{20}$$

Tuning the concentration of the β1D_V in solution at the same preload (Fig. 69A,C) leads to similar dwell times for the bound state (cyan dwells) and variable dwell times for the unbound state (purple dwells), as expected from the fact that the bound lifetime only depends on the bond strength, while the binding time gets shorter at higher concentrations. Also the applied preload is expected to influence the binding time, since it affects the open probability P_{open} (Eq. 20 and Fig. 70B), while the off-rates are also force insensitive (Fig. 70A).

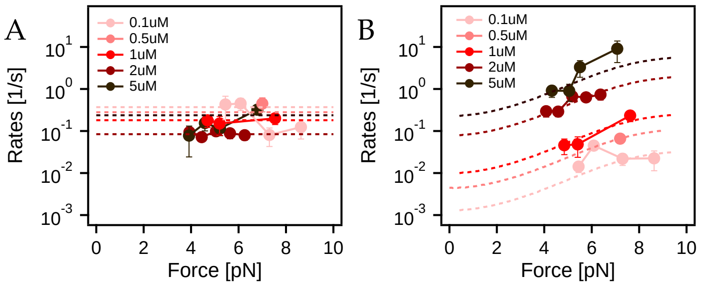

Fig. 70. Binding and unbinding rates of the β1D_V. (A) The unbinding rate k_{off} is constant at all probed concentrations and forces. Dotted lines mark the average value of all traces at the same concentration. (B) The plotted pseudo first-order rates are obtained by the pure distribution of the purple dwell events of Fig. 69A–C, thus they vary with the applied preload and with the concentration of the solution peptide. Dotted lines are fits with the function $1/\tau_{\mathrm{on}}(F)$, obtained by inverting Eq. 20, where the only free parameter is the on-rate k_{on} (the open probability $P_{\mathrm{open}}(F)$ is measured from the flipping regions, and the peptide concentration is known).

Once the on- and off-rates are known, the affinity can be calculated (Eq. 14). The average value of the affinities obtained with [β1D_V] = 0.5, 1 and 2 µM is 0.15 ± 0.09 µM, a factor of 7 higher than that measured using NMR [5].[3]

9.2 THE "DEAD STATE" ISSUE

A limitation of the previous measurements is the presence of low-noise, bound-like dwell events even in the absence of solution peptides. A passive-mode trace at the same average preload of Fig. 69 with the T2-β1D is shown in Fig. 71. On average, every 62 ± 45 s the interaction between integrin and talin is somehow compromised, and the system lies in the open state for (on average) 8 ± 3 s.

---

[3] An alternative and more elegant method to extract the affinity would be a global fit of the data. If the ratio $\tilde{k}_{\mathrm{on}}/k_{\mathrm{off}}$ is plotted vs. [β1D_V], the dependence is expected to be linear (Eq. 16), with the slope being $1/K_D$. The average was preferred over a global fit because the extreme points would have a higher weight, while in this case they are the less precise. At high concentrations the short $\tilde{k}_{\mathrm{on}}$ leads to a higher probability of missing events, with the risk of everestimating the lifetime of the bound cyan state. At low concentration, the presence of so-called *dead-states* would compromise the correct assignment of the bound state. This effect is discussed in the next section (9.2). For these reasons, the data at [β1D_V] = 0.1 and 5 µM were excluded from the affinity average.

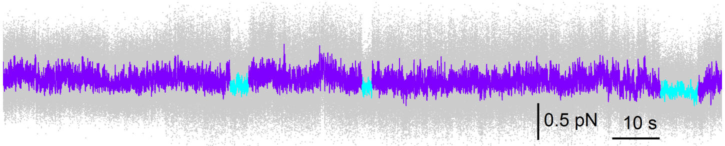

Fig. 71. Dead states. In the absence of peptides in solution, the system The pseudo first-order on-rate is $\tilde{k}_{\mathrm{on}} = 0.016 \pm 0.011$ /s and the off-rate is $k_{\mathrm{off}} = 0.13 \pm 0.05$ /s.

A couple of experiments have been performed to investigate the reason of this behaviour, which is also present in the T2-β1D_LL construct.[4] In particular, two control experiments were performed to rule out the possibility that some components used in the experimental protocol (Sec. C.2) interfere with the measured system. First, the bovine serum albumin used to passivate the surface was removed, and no difference was observed. Afterwards, the glucose oxidase-catalase scavenger system was substituted with the alternative protocatechuic acid-protocatechate 3,4-dioxygenase system [66], and also in this case the frequency and the lifetime of the dead states were unaffected. Similar effects have been observed over a broad range of proteins, for example in the EF1-2 domain of calmodulin [111].

It has to be noted that, in the experiments shown in the previous section with the stable variant β1D_V of the integrin β1D tail, the frequency of the bound state appearances (cyan dwells) was always faster than that of the dead states, apart from the lowest probed concentration of 0.1 µM. All data contain some putative binding events that are instead dead events, but this effect gets more and more prominent at low concentrations. At the concentration of 0.1 µM, the τ_{on} are comparable to those between two dead events, hence the estimation is not reliable anymore, and these data were excluded from the affinity average of the previous section.

9.3 COMPETITION WITH THE NATIVE β1D INTEGRIN TAIL

In a second set of experiments, the β1D peptide with the native sequence was added to solution, in analogy to Sec. 9.1. Because of the lower affinity ($K_D = 36$ µM, see [5]) compared to the β1D_V mutant, a higher concentration of the peptide in solution was employed.

---

[4] For the kinetic analysis shown in Fig. 60 and Fig. 66, these events were not considered.

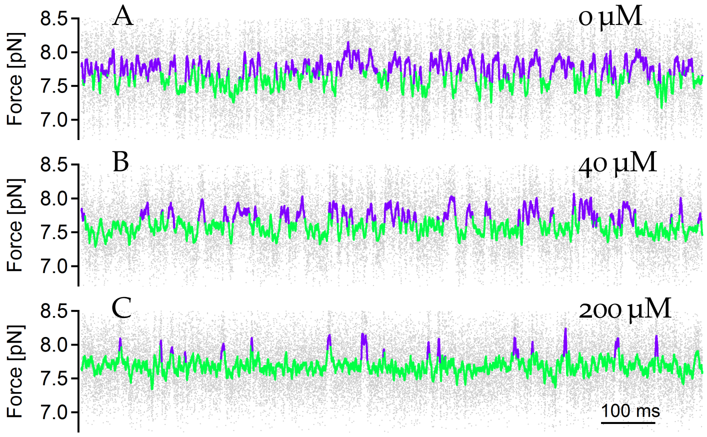

Fig. 72. Competition assay with the peptide β1D. (A–C) Passive-mode traces of 1 s with the addition of no peptide (in *A*), 40 µM (in *B*) and 200 µM (in *C*) of the β1D peptide in solution. All traces were recorded at similar preloads, and were analyzed with the HMM algorithm, using a two-state system.

A passive-mode trace with the addition of 40 µM of β1D in solution is shown in Fig. 72B. Although the overall kinetics may seem similar to those in the absence of solution peptides (Fig. 72A), the occupancy of the open state is higher if β1D was added. The addition of more peptide in solution (200 µM) leads to a even higher occupancy at the same preload of the open state (Fig. 72B). The reason of this effect is that the open state is a mixture of open and bound states (Fig. 73), the separation of which is more challenging compared to the β1D_V variant, because in this case the exchange between these two states is fast. The lifetime of the bound state is expected to be in the order of 20 ms, which is the inverse of the zero-force unbinding rate extracted from the tethered peptide (60 /s, see Fig. 66B). Given the short bound dwells, the separation of the bound and open dwells with a time threshold (as described in Sec. 3.5) is not possible anymore.

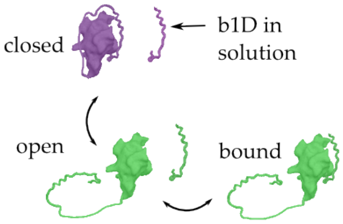

Fig. 73. Kinetic network of the competition assay, in presence of the β1D in solution. Given the fast kinetics between the open and the bound states, they were merged for the HMM analysis of Fig. 72 into a single state, in green.

However, from the shift of the occupancies (Fig. 74A) an estimation of the dissociation constant can be obtained. Let us consider the midpoint force F_{mid} in the absence of solution peptides.[5] With increasing concentration of the peptide, *at the same preload* the closed state occupancy decreases. At $F = F_{\text{mid}}$, the relationship between P_{closed} and the concentration of the peptide in solution $[\beta 1\mathrm{D}]$ is[6]

---

[5] The midpoint force is normally defined as the force where the two occupancy branches intersect (see Box 5). In each passive-mode trace the open and closed states have different forces. As a consequence, the occupancy at the midpoint force is higher than 50 %. Eq. 21 holds at a force where the closed occupancy in absence of solution peptide is 50 % (8.1 pN), thus this was the force employed as F_{mid} for the following estimations.

$$P_{\mathrm{closed}} = \frac{1}{\frac{[\beta 1\mathrm{D}]}{K_D} + 2}. \tag{21}$$

A fit of the data (Fig. 74B) returns $K_D = 8.7 \pm 0.9\,\mu\mathrm{M}$, a value which is a factor of 4 lower than that published in the literature. If this number is inserted in Eq. 14 together with the off-rate at zero-force extrapolated from the rate vs. force plot (60 /s), the on-rate for the talin 2/β1D interaction can be estimated to be $6.9 \pm 0.8\,/\mathrm{s}\,\mu\mathrm{M}$. From Eq. 16, using the zero-force rates of the fusion construct (Fig. 66B), the effective concentration of the tethered peptide can be calculated to be $0.24 \pm 0.08\,\mathrm{mM}$.

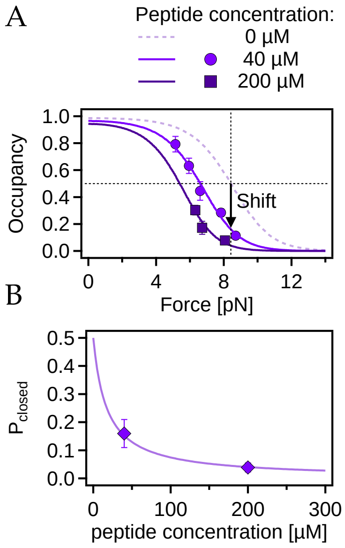

FIG. 74. Affinity of the talin 2/integrin β1D interaction measured with the competition assay. (A) Occupancy of the closed state at different forces and peptide concentrations. The horizontal dotted line marks the 0.5 closed probability in the absence of peptide. The vertical line marks the midforce F_{mid}. (B) Occupancy of the closed state vs. peptide concentration, at $F = F_{\mathrm{mid}}$ (vertical line in *B*). The errors on the points are calculated as 10 % of the values, which is given by calibration errors.

The data analyzed in this section were taken from regions that do not include any "dead" events, which are present in all experiments. A strange observation in the presence of 200 µM of the β1D is that the frequency of dead events increases by a factor of three.[7] Whether these additional events are due to some strong bond formed by talin and multiple β1Ds, or the presence of many peptides in solution somehow inhibits the binding of the tethered peptide, cannot be said at this stage.

9.4 OUTLOOK

The combination of fusion constructs with the competition assay offers a versatile toolkit for the investigation of the anchoring of talin at the membrane, as well as the integrin activation process. From the presented data, it is clear that the lifetime of the talin 2/β1D bond—which is the most stable isoform combination found in our body—does not exceed a hundred of milliseconds, a time too short to provide long-term anchoring of the cytoskeleton at the membrane.

The role of additional interactions has to be investigated to give a better picture of the integrin-activation process. In particular, the role of the membrane in stabilising the talin/integrin bond is still unexplored, mainly because of the difficulties in combining affinity measurements with lipids. Molecular dynamics simulations showed that even in the absence of embedded integrin, the talin F2–F3 domains can be recruited by the membrane [57], but experimental evidence is still lacking.

---

[6] This formula can be obtained considering that, at equilibrium, $K_D = (P_{\mathrm{open}}/P_{\mathrm{bound}})[\beta 1\mathrm{D}]$, and, at F_{mid}, $P_{\mathrm{closed}} = P_{\mathrm{open}}$. In addition, one has to note that the sum of the occupancies P_{closed}, P_{open} and P_{bound} is unity.

[7] This was not an isolated case, as the measurement was repeated multiple times.

The recent development of synthetic cell-free membranes, called *nanodiscs*, has paved the way for the study of membrane-like lipid/protein interactions. A nanodisc is a system composed of a lipid bilayer, whose hydrophobic site is masked by *membrane scaffolding proteins*, as shown in Fig. 75. Nanodiscs have been successfully employed in different applications such as NMR [40] or Raman Spectroscopy [78]. Furthermore, different lipids can be combined, thus mimicking the effective charges of cell membranes.

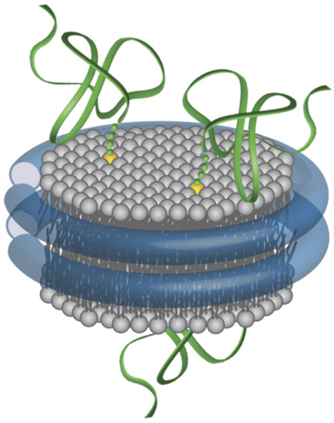

FIG. 75. Schematic of a nanodisc. A lipid bilayer (in grey) is kept soluble by two membrane scaffolding proteins (in blue), whose size determines the radius of the nanodisc. Transmembrane proteins can be embedded in the membrane (in green), and studied in bulk experiments.

A fascinating outlook for the previous experiments is the application of the nanodisc technology to the competition experiments described in the previous sections. If a complete integrin can be embedded within a nanodisc, the combined effect of the cytoplasmic tail and the membrane surface on the binding of talin could be explored. A tighter binding should appear as an increase in the open probability, if the native β1D sequence is employed (Sec. 9.3), or of the bond lifetime, if the β1D_V mutant is employed (Sec. 9.1).[8] The established competition experiment is thus a powerful tool to further investigate binding kinetics, hopefully also in presence of membrane-embedded proteins.

A second possible application is the study of how talin and kindlin compete for the binding of integrin. Although different binding sites were found on the integrin tail for talin and kindlin, it is still under debate whether they can simultaneously bind the same β tail, and in that case, to what degree the affinities are influenced. A new fusion construct and solution domains could help to get more insights about the compatibility of the different integrin substrates.

---

[8] In principle, it is not known if a higher affinity results in slower unbinding rates, in faster binding rates or in a variation of both rate constants, but the hope is that the bond lifetime will be found to be affected by the presence of the membrane. The use of the β1D_V mutant embedded in the surface can have several advantages. The high affinity allows the use of lower concentration in solution, on the order of a µM, which could be more feasible for optical tweezers applications. Moreover, the longer lifetime (well separated from the dwell times of the open state) permits a more precise estimation of the binding/unbinding kinetics.

9.5 SUMMARY

Thanks to the addition of free peptides to solution, the affinity of the β1D integrin tail with talin 2 could be measured. A dissociation constant of $\sim 10\,\mu\text{M}$ was found, a factor of 3 lower than that estimated in previous bulk experiments. A mutant of the β tail with 1000-fold affinity was also employed as a control. The competition assay serves as an exciting addition to the toolkit for possible future experiments.

Part IV

APPENDIX

A

SUPPLEMENTARY EXPERIMENTS ON α-ACTININ/TITIN INTERACTION

In this chapter, some additional experiments on the α-actinin/titin interaction (chapters 4, 5 and 6) are presented and discussed.

Sec. A.1 deals with the bimodal stability of the FB state in the PullA-T7 and PullA-T1 constructs. Afterwards, some validations of the structural interpretation of the FU state will be discussed (A.2). Moreover, a direct measurement of the effective concentration of the fused ligand is presented (A.3). Finally, a correction of the rebinding kinetics for the PullT7 construct is addressed (A.4).

A.1 BIMODAL STABILITY OF THE FB STATE

In sections 5.1 and 5.2 the typical unfolding pathway of the PullA-T7 construct was discussed. In constant-velocity experiments at the low pulling speed of 10 nm/s, the system has the time to refold/rebind at low forces (Fig. 38), even if the force is monotonically increased. Conversely, at higher pulling speed a single unbinding/unfolding event can be observed, while rebinding under force is very rare (Fig. 76A). Remarkably, the unfolding force distribution over many cycles of the same molecule is double peaked, pointing toward two different binding modes of the T7 peptide (Fig. 76B).

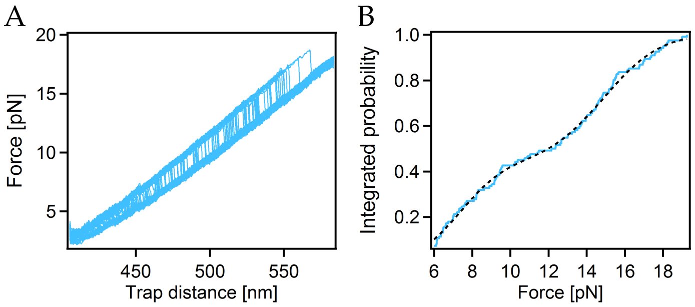

Fig. 76. Unfolding force distribution of the PullA-T7 construct. (A) Filtered unfolding traces ($N = 150$) at the pulling speed of 600 nm/s displayed vs. trap distance for clarity. (B) Integrated histogram of unfolding force distribution, fitted with a double sigmoid function (black dotted line). The real force distribution is a skewed Gaussian, but for this integrated distribution a simple sigmoid function (the integral of a Gaussian is a sigmoid) is employed.

Also passive-mode traces depict a similar behaviour. Fig. 77A shows a contour length vs. dwell time scatter plot of a long passive-mode trace (the same from which Fig. 40 was excerpted). The cumulative normalised distributions of the dwelltimes were calculated and fitted with single exponential functions (Fig. 77B). The UU and FU states (red and green) were exponentianlly distributed, whereas the FB state (purple) distribution was better fitted by a double exponential function, at all measured forces (Fig. 77C), including the unbinding rates at high forces coming from the jump assay. The two unbinding rates extracted from each trace have a similar slope in the rate vs. force plot, indicating a similar distance from the transition state (Fig. 77D). The difference in the zero-force unbinding rates between the two branches is about a factor of 10.

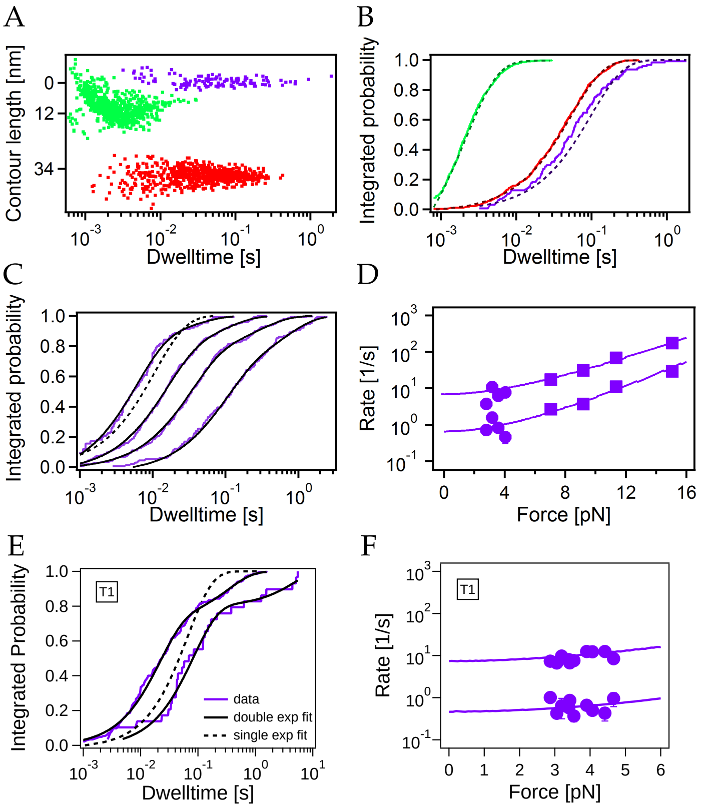

Fig. 77. Dwelltime analysis of PullA-T7 (A–D) and PullA-T1 (E–F) passive-mode traces. (A) Contour length vs. dwelltime plot of a 55 s trace. (B) Integrated distribution of the dwelltimes depicted in *A*, and single exponential fit functions (dotted lines, Eq. 10). (C) Integrated distribution of the dwelltimes relative to the F states, at different forces (each curve corresponds to a passive-mode trace), with double exponential fits (solid lines, Eq. 11). The dotted line is the single exponential fit of the trace at the left, as an example. (D) Rate constants extracted at different forces from the double exponential fits. Square dots are obtained using the jump-assay. Rates from each phase was fitted to extract the zero-force rate constant (solid lines). (E) Same as in *C*, but for the PullA-T1 construct. (F) Same as in *D*, but for the PullA-T1 construct.

The double exponential distribution of the FB state in passive-mode assays, as well as the double peak distribution of the unbinding forces, indicate a model where the tethered T7 peptide has a bimodal stability. Interestingly, the dwell times of the peptide-bound state FB follow a double exponential behaviour at all forces also for T1 (PullA-T1 construct, Fig. 77E–F), while a single exponential distribution is observed for the binding of

T3 and the neck. Also the PullT7 construct exhibit a single binding mode of the T7 peptide.

A possible explanation of the bimodal stability of the T7 peptide in the PullA-T7 construct (and T1 in PullA-T1) is the presence of two different binding sites on the EF3-4 with different stabilities, or, alternatively, two different binding modes on the same site. An example for the latter hypothesis is shown in Fig. 78, based on geometrical considerations. The length of the linker between the EF3-4 and the titin Z-repeats permits two different binding configurations, shown in Fig. 78B–C. Depending on the position, the linker entropy—related to the stretching degree— is different, affecting the binding energy.

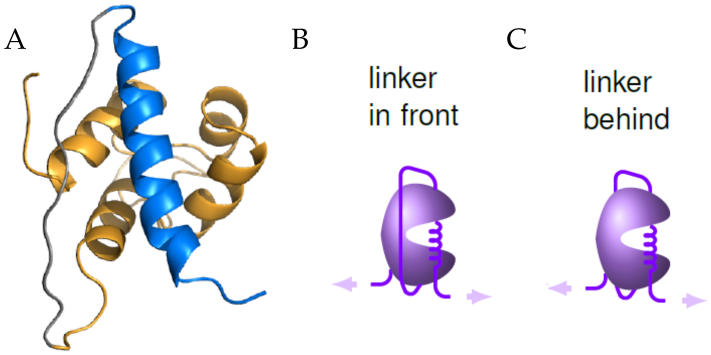

Fig. 78. Example of bimodal binding stability in fusion constructs. (A) NMR structure of α-actinin EF3-4 and titin T7 (see Fig. 36), with the addition of the 4×`(GGS)` linker. The structure of the linker was simulated using the software Coot. (B–C) Two possible arrangments of the linker are allowed (in front or behind the complex), leading to different end-to-end lengths, thus entropies. The measured binding energy is affected by the energy needed to stretch the linker.

This hypothesis seems to be supported from the competition assay, where no linker is present and the binding of the peptide from solution is unimodal. The weak binding peptides T3 and neck may still have two binding modes, but owing the lower binding energy, the weaker branch could be too fast to be detected. In the PullT7 construct, where three amino acids have been added to the linker in order to separate the cysteine and the T7 α-helix, the linker may be long enough to have similar entropic energies in both configurations.

In Fig. 44 and in Table 2, the stable phase of the double exponential distribution was employed. The main reason for that choice is that the extracted zero force off-rates of PullA-T7 coming from the stable branch are compatible (within a factor of two) with the force-free unbinding rates from solution (competition assay) and are identical to those extracted with the PullT7 construct.

A.2 THE PULLA CONSTRUCT AND THE FU STATE

There are mainly two lines of evidence to support the statement that the short green events observed in the fusion constructs correspond to a configuration where the EF3-4 is folded and the tethered peptide is unbound (FU state). The first, and most important one, is given by a construct (named PullA) where the only EF3-4 domain is subjected to load. The force data obtained with PullA are summarised in Fig. 79. Since the unfolding starts at very low forces (already at zero load, the domain is expected to spend half of the time unfolded, Fig. 44A) no transitions can be observed using force ramps (Fig. 79A), but in passive-mode experiments the short green spikes can be detected (Fig. 79B). The frequency and lifetime of the green dwell events is compatible with data coming from the PullA-T7 construct, at the same preload.

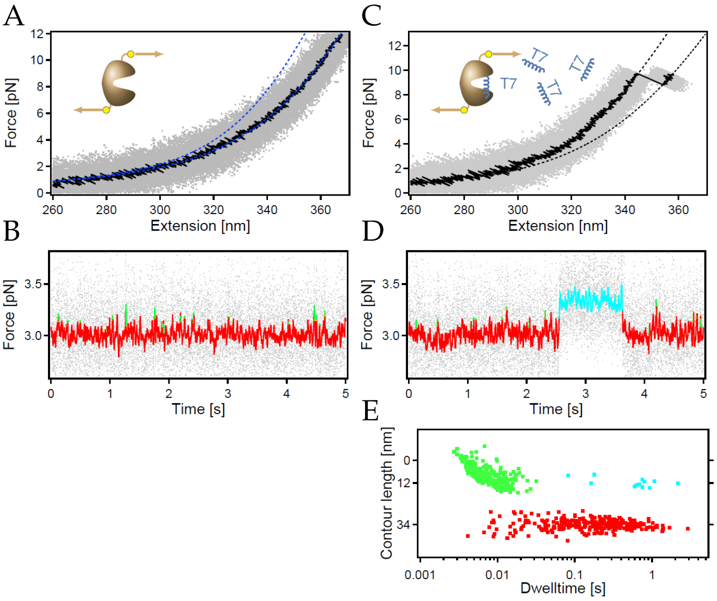

Fig. 79. Data from the PullA construct, alone (first column) and in presence of T7 in solution (second column). (A) Constant-velocity traces at the speed of 20 nm/s. A blue WLC curve was calculated and plotted to obtain the expected CL gain of 22 nm. This curve is not a real fit and has the only purpose to guide the eye. (B) Passive-mode traces with colour coding as in Fig. 40A. (C) Constant-velocity traces with T7 in solution at the speed of 100 nm/s. (D) Same as in *B*, with the binding from solution depicted in cyan. (E) Contour length gain vs. dwell time, with T7 in solution. An offset of 12 nm is applied, to help comparison with Fig. 77A.

Adding the T7 peptide to solution leads to a stabilisation of the FU state upon binding, observable in force ramps (Fig. 79C) and passive mode (Fig. 79D–E). The measured affinity was in agreement with that measured using the PullA-T7 construct. The presented data rule out the hypothesis that the green spikes are some kind of intermediate unstable configuration, where the peptide forms a non-native structure with part of the EF3-4 domain.

Another confirmation to this model is the fact that the UU↔FU transitions had similar kinetics in all fusion construct, even with different tethered peptides.

Moreover, competition assays with T7 in solution performed using tethered T1, T3 and T5, always led to similar affinities of T7 to EF3-4, indicating the same functionality of the EF3-4.

It has to be noted that, altough a kinetic network with FU as an *obligatory on-pathway intermediate* was employed, in principle the folding of EF3-4 may occur upon binding of T7. Even considering such a possible direct pathway between UU and FB, the kinetics would not change drastically, as well as the titin anchoring lifetime estimated in Sec. 6.2 (Eq. 19). In fact, the unbinding rates of T7 do not depend on FU being on- or off-pathway, while the rebinding kinetics is better depicted by the PullT7 construct, where the UU and the FU states cannot be separated.

A.3 EFFECTIVE CONCENTRATION OF THE TETHERED PEPTIDE

It was shown in Sec. 5.5 that the competition assay allows the extraction of the affinity between the EF3-4 domain and the T7 peptide. Once the affinity K_D is known, the effective concentration of the tethered peptide $[P_{\text{tethered}}]$ can be obtained by inverting Eq. 16. Inserting the rates $\tilde{k}_{\text{on}}$ and k_{off} of the T7 peptide extrapolated from the fusion construct (Fig. 44B and Table 1), the resulting effective concentration would be 2 mM. This value is not very different from that estimated from basic geometrical considerations (Box 14).

BOX 14. A ROUGH ESTIMATION OF THE EFFECTIVE CONCENTRATION

A rule of thumb for the evaluation of the effective concentration would suggest to consider that the linker of length L connecting EF3-4 and T7 limits the diffusion of the peptide to a sphere of radius L (Fig. 80). The concentration can be calculated by dividing the number of particle (one ligand) by sphere volume. The linker length is related to the number of amino acids and the backbone length of each amino acid, in this case $L = 12\,\text{aa} \times 0.365\,\text{nm} = 4\,\text{nm}$. The concentration of the tethered peptide can be estimated as 3 mM. This rough approximation works in the hypothesis that the linker anchoring point on A is in close proximity to the binding site, namely $D \ll L$ in Fig. 80.

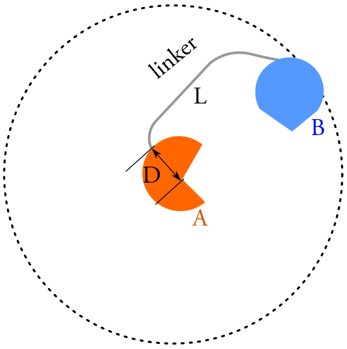

FIG. 80. Effective concentration calculation. Fixing the position of the molecule A, the effective concentration of B can be calculated considering the presence of one molecule in the volume allowed by the linker. This estimation is valid if the linker length L is significantly longer than the distance D between the linker attachment point on A and the binding site on A.

To obtain a more precise estimate of $[P_{\text{tethered}}]$, a new assay was introduced, combining the competition and the jump assays. The idea is to calculate the concentration of the tethered peptide using a known concentration of T7 peptide in solution, and comparing the pseudo first-order on-rates. In practice, the number of binding n of the tethered vs. the free peptides in a time trace are linked by

$$\frac{n_{\text{tethered}}}{n_{\text{free}}} = \frac{[P_{\text{tethered}}]}{[P_{\text{free}}]}, \tag{22}$$

derived from Eq. 16, with $k_{\text{on}} = n/t_{\text{experiment}}$.

One would be tempted to apply this method to the passive-mode trace of Fig. 45A, but in that case the tethered peptide is disadvantaged, because a transition FU→FB is against force. More technically, the pseudo first-order on-rate of the tethered peptide (under force) is not the same of the free peptide (force-free). In that experiment ($P_{\text{tethered}} = 52\,\mu\text{M}$), one would find only a factor of 3 between the number of appeareances of the tethered and free peptides. However, if the competition could be performed at zero force, Eq. 22 would hold, but at zero load the resolution does not allow the separation of the different states.

To bind the peptides at zero force and be able to discriminate which peptide (free or tethered) has bound to the EF3-4, rapid jumps were performed, between zero force (binding level) and ~9 pN (detection level). In addition, after the detection level a third jump at the high force of ~21 pN (unbinding level) was introduced, to reset the system in the UU state. Fig. 81 shows a 1 s extract of a 100 s trace: By tuning the time spent at each level, it is possible to obtain 10 events/s. The concentration of the tethered peptide obtained with Eq. 22 is 0.64 ± 0.07 mM.

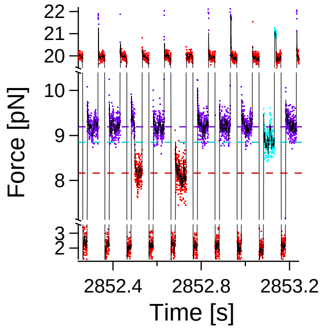

Fig. 81. Three-jump assay. The system is driven from a low-force level (~2 pN), where refolding of EF3-4 and rebinding of T7 is promoted, to a middle-force (~9 pN), where binding of tethered or solution peptides could be distinguished, and finally to a high force level (~21 pN), where the system is reset to the unfolded/unbound state. The waiting times are respectively 20, 50 and 30 ms.

A.4 CORRECTION OF PULLT7 REBINDING RATES

To analyze the passive-mode traces of the PullT7 construct (Fig. 49A) a two-state system was assumed, since this pulling geometry enables only the the FB↔FU transition. This hypothesis holds only if the EF3-4 spends a negligible time in the unfolded state, which is not the case. As discussed in the Sec. 5.4, the EF3-4 domain has a very low stability: even at zero-load, it spends about 50 % of the time in the unfolded state. In the PullT7 geometry, the monitoring of the EF3-4 unfolding is suppressed, since it is not associated to any contour length change (Fig. 82). The UU state, hidden in this construct, slows down the rebinding of the T7 peptide, while the unbinding lifetimes are unaffected.

A correction of the PullT7 data can be applied on the base of the zero-force population probabilities and rate constants extrapolated using the PullA-T7 construct. In particular, the zero-force exchange rate between UU and FU, which is ∼100 /s in both direction (Fig. 44A), can be used to correct the rates and the dissociation constant.

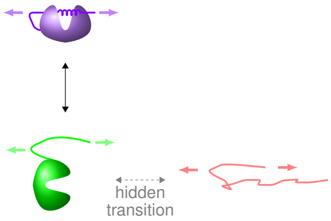

Fig. 82. Schematic of the correct kinetic network of the PullT7 construct.

BINDING RATES The uncorrected binding rate constants of T7 are shown in Fig. 50A (green dots), and lie in the range of 1–30 /s. The exchange rate UU↔FU of 100 /s implies that the EF3-4 domain undergoes a few folding/refolding transitions before every peptide rebinding. Hence, it is reasonable to assume that the analyzed green dwell events are an equal mixture of FU and UU events. It follows that all binding rate constants of Fig. 50A are half of the real ones. The zero-force extrapolated binding rates has to be accordingly corrected for a factor of 2 (Table 1).

DISSOCIATION CONSTANT The dissociation constant measured in the competition assay can be corrected considering a factor of 2 in the binding rates. Intuitively, the time spent by the system in a state competent of binding the peptide in solution is half of the one calculated. If the real binding rate is twice the measured one, the dissociation constant has to be halved, as it follows from Eq 14. The corrected value is $K_D = 4 \pm 2\,\mu\text{M}$, in perfect agreement with that obtained from the PullA-T7 geometry.

B

ALTERNATIVE BIOCONJUGATION TECHNIQUES FOR THE DUMBBELL ASSAY

In this chapter new bioconjugation approaches to create a dumbbell assay in a dual-beam optical trap (Fig. 8) are discussed. In particular, the critical step is the coupling of the protein construct with the DNA oligonucleotides, especially without employing mutated cysteines. The first part of the chapter contains a general introduction to bioconjugation techniques (B.1) and a list of requirements for choosing an effective conjugation strategy in a dumbbell assay (B.2). Afterwards, the typical method based on cysteine modification is discussed (B.3) followed by an alternative approach based on protein tags (B.4). The last four sections deal with two different tag-based approaches to create a cysteine-free dumbbell assay. A strategy using the HaloTag is presented (B.5) and progressively applied first to a known protein construct (B.6) and then to a new protein/protein interaction involving a cysteine in the native sequence (B.7). In the last section, the ybbR tag labelling is investigated as a versatile method for protein coupling with oligonucleotides (B.8).

B.1 INTRODUCTION

Bioconjugation techniques are the key ingredients of each biochemical and biophysical measurement. The identification and tracking of sub-micrometer-sized biological structures heavily relies on sample labelling with radioactive isotopes, heavy metals or fluorescence dyes.

Depending on the requirements, different labelling specificities have to be achieved. In separation techniques such as agarose or SDS-PAGE gels, all DNA or protein molecules of the sample are stained. More often, it is crucial to label specific proteins, like the different cytoskeleton filaments (Fig. 83), or even a single aminoacid, like in FRET measurements, where the en-

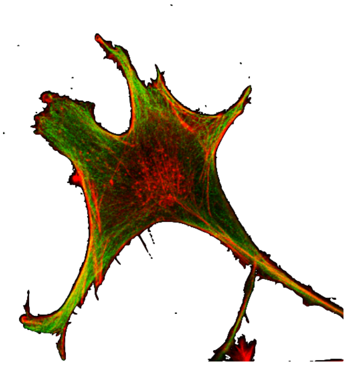

Fig. 83. Cell image with fluorecently labelled actin (in red) and microtubules (in green). Image courtesy of Leone Rossetti.

ergy transfer between two fluorophores is used to monitor the dynamics of protein/protein interactions or protein conformational changes (Fig. 84).

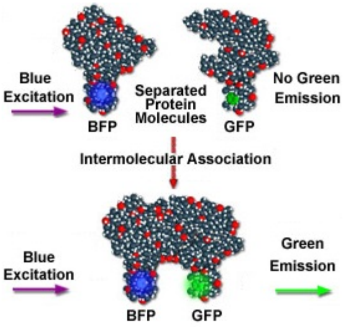

Fig. 84. Observation of protein/protein interaction by FRET. Under excitation with blue light, energy transfer between the two dyes results in green light emission when they are in close proximity, i.e. when the two molecules associate. Since the FRET efficiency strongly depends on the distance of the dyes in the bound conformation, the labelling position is critical in this case.

Single-molecule force spectroscopy relies as well on the ability to precisely define the pulling geometry, possibly without affecting the mechanical behaviour of the components under study. The PullT7 construct presented in Sec. 5.7 is a good example of a non-standard pulling geometry[1] that helped to better understand the force propagation of a protein complex under physiological conditions. Another example is a recent study on the π-π stacking between DNA base pairs, which was only possible by using rigid DNA origami nanostructures, in order to adopt a face-to-face geometry of the aromatic rings [59]. In the last twenty years, AFM studies have been pioneering in bringing new bioconjugation techniques to the SMFS field [63, 92, 116, 117].

B.2 REQUIREMENTS TO GET A WORKING DUMBBELL ASSAY

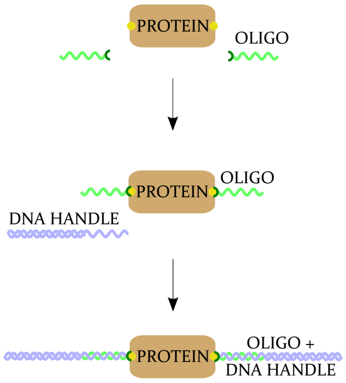

Fig. 85. Coupling of oligonucleotides and DNA handles to the target protein. First, the protein is incubated with modified-oligonucloetides to form a covalent bond. In a second step, the DNA handles are added, that hybridise to the oligonucleotides.

The procedure used to conjugate the protein to the trapped beads was described in Sec. 2.5. To summarise, the protein is first coupled to short DNA oligonucleotides (oligos) in the two points where the application of force is required (Fig. 85). From this step on, the assembly of the dumbbell is straightforward, since the hybridisation of the oligos with the DNA handles, as well as the binding to the functionalized beads, are fast and reliable processes. Therefore, the main challenge is to bind the desired protein to the oligos, possibly with the following requirements:

SPECIFICITY The attachment positions of the oligos are the points where the force will be applied. Hence, it is fundamental that exactly two binding sites can be placed within the protein construct.

EFFICIENCY Although the reaction can be prolonged over night, the binding has to be fast enough at room temperature, or even better at 4 °C. Some proteins may survive a long exposure at 37 °C, but a protocol that involves incubation at such temperatures for a few hours is not applicable to every systems.

---

[1] A standard pulling geometry is intended as N- and C-termini pulling positions.

MECHANICAL STABILITY The bond has to be covalent, or at least strong enough[2] to withstand the forces applied during the experiments (∼0–50 pN). Moreover, if the approach involves the introduction of additional protein domains, they have to unfold at high forces, like the ubiquitin domains used as spacers in some construct within this work.

OLIGOS AVAILABILITY Not many oligo modifications are available on the market.[3] The conjugation design has to take this factor into account.

PORTABILITY In some cases—for instance the PullT7 construct of Sec. 5.7—the pulling points need to be placed inside the protein, and not at the N- and C-termini. The conjugation of the oligos must not interfere with the folding/binding mechanics of the system.

To select a robust bionconjugation technique, all aforementioned requirements have to be fulfilled. Nonetheless, since in the majority of force-spectroscopy applications a sophisticated pulling geometry in terms of internal tethering is not required, an approach that satisfies the first four requirements (all but portability) is still a valid one.

B.3 BEYOND CYSTEINE MODIFICATIONS

The excellent review of Stephanopoulos and Francis [109] presents a practical workflow for choosing the most suited bioconjugation technique for protein labelling. Using the requirements presented in the previous section, the easiest choice one encounters following the workflow is the insertion of two cysteine residues at the desired positions: first, cysteines are very rare amino acids (about 1 % in Human and *E. coli* [79]), thus a few—or sometimes even any—mutations are needed. Second, they carry a thiol group that can be covalently coupled to a range of chemical groups such as thiol, maleimide and iodacetamide, some of them available for oligo modification. Third, the addition of a cysteine is a single point mutation that can be placed more or less in every loop region of a protein, usually with minimal interference with the stability of the protein. No surprise that cysteine modification is the most common conjugation approach in force-spectroscopy.

---

[2] The streptavidin-biotin bond employed for bead coupling is not covalent, but it is one of the strongest non-covalent bond known in nature [42].

[3] Although many companies offer custom oligo conjugation, the feasibiliy and purity of the sample are difficult to predict.

Nonetheless, the addition of cysteines at the pulling positions requires the mutation of all the other internal cysteines.[4] A mutation using an amino acid with similar structure (serine) or similar chemical properties (valine) may in many cases not affect the mechanical stability of the protein. However, there are situations where many cysteines are present and/or they are required for functional or structural reasons. Moreover, alternative conjugation approaches could be employed in order to use cysteines for other applications, for example fluorescent labelling (Box 15).

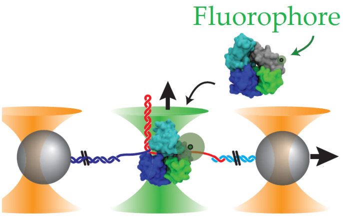

FIG. 86. Schematic of a hybrid setup with dual-beam optical tweezers (orange lasers) and confocal fluorescence (green laser), also called *fleezers*. UvrD helicase is labelled with a fluorophore. The number of proteins required to unzip a DNA harpin is observed by combination of fluorescence and force signals [18].

BOX 15. COMBINING SINGLE-MOLECULE FLUORESCENCE AND FORCE-SPECTROSCOPY

Another reason for investigating orthogonal chemistries to cysteine conjugation is to utilise cysteine residues for fluorescence experiments. It is remarkable how all the information obtained from the SMFS data are coming from one variable—the protein extension, thus the force—observed over time. A recent experiment on helicase activity (Fig. 86) paved the way to the addition of orthogonal information by combining single-molecule fluorescence and force spectroscopy [18]. Comstock *et al.* investigated the number of UvrD helicases necessary to unwind a DNA hairpin, monitoring unwinding activity with the force signal (optical tweezers) and counting the number of proteins by photobleaching (fluorescence). Moreover, they showed how the combination of FRET and optical tweezers allows the correlation of the two structural conformation of the UvrD helicase with its function of zipping or unzipping a DNA hairpin. To label a protein for fluorescence applications, cysteine modification is an unique tool, because it is highly specific and requires a single point mutation. Another strategy with the same spacial resolution (a single point mutation) is the use of unnatural amino acids [135], but the incorporation of them into a protein is not a straightforward process.

---

[4] Cysteines can covalently crosslink, thanks to the disulfide bond formed by their thiol residues. Cysteines that are hidden inside the structure of the protein, i. e. that are not at the surface of a domain, are not exposed to oligo coupling. Nonetheless, if two or more cysteines are present, repeated unfolding and refolding cycles can favor crosslinking. The disulfide bond can be disrupted by addition of reducing agents, but the refolding kinetics would be modified. The purpose of this chapter is to discuss an approach as general as possible, thus the presence of internal cysteines is overall unwanted, if the cystein-modification pulling approach is chosen.

B.4 PROTEIN TAGS AS AN ALTERNATIVE APPROACH

The most promising alternative approach satisfying the requirements listed in Sec. B.2 is the incorporation of protein tags within the protein construct. A couple of different tags—ranging from a few amino acids to big domains—have been identified to have binding partners (termed *ligands* hereafter) with which they form a covalent bond. Some examples are the SNAP tag [58], ybbR tag [131], CLIP tag [36], SpyTag [68] and HaloTag [73].

The applicability of protein tags for optical tweezers measurements is shown in Fig. 87, for simplicity starting from the standard N-C-termini pulling geometry. If the protein under study is recombinantly expressed, the DNA sequence of the tag can be introduced in the plasmid, before and after the sequence of the target protein. The only concern is the final size of the construct, especially if expression is carried out in *E. coli*.[5]

Once the protein harbouring two tags is expressed, there are two possible ways to let the protein, the ligand and the oligos bind together, as depicted in Fig. 87.

In the next sections two different tag-based strategies are investigated, in both cases drawing inspiration from recent AFM studies.

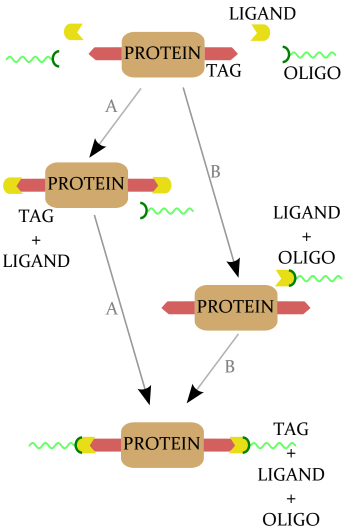

Fig. 87. Oligonucleotide conjugation to a target protein in a tag-based approach. Two tags are fused (here at N- and C-termini) via recombinant techniques, and the incorporation of ligand and oligos can be obtained following two pathways (A and B).

B.5 HALOTAG

The HaloTag is a 33 kDa domain which is able to bind a chloroalkane ligand with all the requirements listed in Sec. B.2, except the last one: the size of the Tag do not permit any other fusion than N- and C-termini. The HaloLigands® can carry a variety of modifications, and bind covalently the residue `D106` of the HaloTag in a fast and autocatalitic reaction, i. e. no enzymes are required.[6]

The unfolding behaviour of the HaloTag has been probed by AFM [96, 116]. The measured unfolding forces were higher than 100 pN in both possible N- and C-terminal incorporations in a polyprotein construct [96]. If the HaloTag is fused at the C-terminal of the protein, the N-terminal side is under load (amino acids

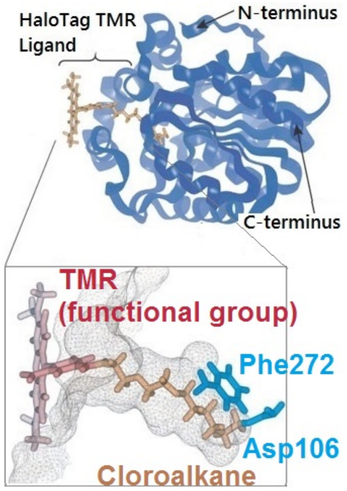

Fig. 88. Structure of the complex formed by HaloTag and HaloTag TMR ligand®, and zoom of the binding cavity. A TMR ligand is shown as an example, but range of ligand modifications is available.

---

[5] There is no teoretical limitation to this value. Protein until 100–120 kDa with a good solubility are usually expressed well.

[6] The HaloTag has been obtained by mutating some amino acids of an haloalkane dehydrogenase (DhaA) protein from *Rhodococcus rhodochrous*. In particular, the point mutation `H272F` has been performed to create a stable covalent bond (Fig. 88).

1-106, called *N-HaloTag*); viceversa, incorporation at the N-terminal exposes to force the C-terminal region of the tag (amino acids 106-299, *C-HaloTag*). The observed contour length gain allowed Popa *et al.* to hypothesise that the first 35 and the last 29 amino acids unravel at low forces ($\lesssim$30 pN), not detectable with AFM (Fig. 89) as summarised in the following table:

Construct	aa under force	expected CL [nm]	measured CL [nm]	aa missing
N-HaloTag	106	39.7	26.5 ± 0.6	1-35
C-HaloTag	193	70.5	66 ± 2	271-299

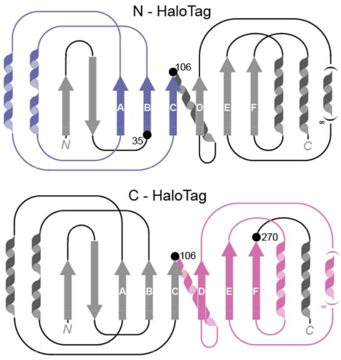

Fig. 89. Topology of the HaloTag in the two pulling geometries [96]. The coloured regions mark residues under force. From the CL gain of the N-HaloTag (top), the amino acids 1-35 (first two β strands) have been assumed to unfold at low forces. Using similar arguments on the C-HaloTag (bottom), the last α helix (271-299) is also expected to unravel at forces lower than 30 pN.

Hence, it is possible that the the unfolding of these sectors occurs in the sensitive force region of the optical tweezers, interfering with the unfolding/unbinding events under investigation.

The HaloTag has been also employed in optical tweezers applications, in order to couple target proteins to DNA handles [11, 29]. Although this insertion did not seem to harm the resolution of the apparatus, none of the previous works investigated low-force effects.

B.6 HALOTAG WITH A KNOWN TARGET PROTEIN

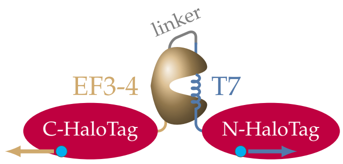

Fig. 90. HaloTag construct equivalent to the cysteines fusion construct of Fig. 37. In the HaloTag version, at both N- and C-termini a tag is introduced to substitute terminal cysteines. The pulling positions (at residue `D106`) are marked by cyan dots.

In order to test the mechanical stability of the HaloTag at low forces, a target protein with a well-known fingerprint in the force range 0–5 pN would be suited. To this purpose, the PullA-T7 construct presented in chapter 5 was chosen as a template. The target protein is rather small (~10 kDa), thus a variant where it is sandwitched between two HaloTags is feasible. Hence, a construct was designed, called PullA-T7(halo), where the tags were fused at both termini, substituting previous ubiquitin domains and cysteines (Fig. 90).

Among the range of HaloLigands®, the Iodacetamide (O4) Ligand was selected, because the Iodacetamide group form a covalent irreversible bond with the thiol group. The ligand was coupled to thiol-modified oligos, following the path B of Fig. 87.[7] Since the ligand is small (0.5 kDa) compared to the oligos (11 kDa), size exclusion chromatography allows the separation of the unreacted ligand from the ligand+oligos fraction (Fig. 91).[8]

---

[7] There are other options to obtain the same result, for example following path A of Fig. 87, but also changing oligos and ligand modifications.

This reaction was then incubated over night at 4 °C with the PullA-T7(halo) construct, and again using size-exclusion chromatography the fraction corresponding to a protein and two ligand+oligo molecules was isolated (more details on the incubation steps are in appendix C.5).

To probe the unfolding pathway of the PullA-T7(halo) with optical tweezers, a combination of force ramps and passive mode was applied, as shown in Fig. 92A. In this way it is possible to monitor the presence of HaloTag unfolding events at the upper force limit, before the traps lose their linearity.

The constant-velocity trace in Fig. 92B shows the typical combination of the T7 peptide unbinding and the EF34 domain unfolding (ΔL_1, see Fig. 38 for comparison). Furthermore, an additional unfolding event at a force of 25 pN is present, with a CL gain $\Delta L_2 = 9 \pm 1\,\text{nm}$.[9] This second event has never been observed in the cysteine construct PullA-T7, thus it has to be ascribed to the unfolding of some region of the HaloTag. As discussed in the previous section, two different portions of the HaloTag are under load, the N-terminal region 1-106 and the C-terminal one 107-299. The observed contour length ΔL_2 could indicate the unfolding of the first two N-terminal β strands (Fig. 89).[10]

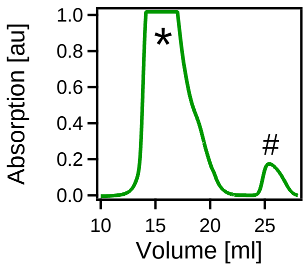

Fig. 91. Size-exclusion chromatogram of the solution containing the iodacetamide-modified HaloLigand and the thiol-modified oligos (absorption at 290 nm). *= ligand+oligo. #= unreacted ligands.

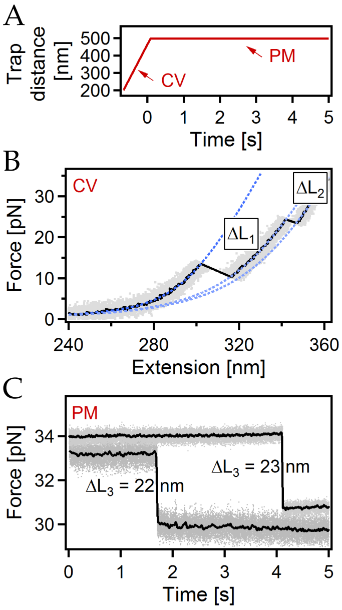

Fig. 92. Unfolding of PullA-T7(halo). (A) Measuring assay. The trap distance was first increased at a constant velocity (CV). Afterwards, the trap distance was kept fixed (passive-mode, PM) at a preload of ~30 pN. (B) Constant-velocity data. ΔL_1 =33 nm; ΔL_2 =10 nm. (C) Two examples of passive-mode data (two different molecules) at high forces. The contour length gain of the unfolding event ΔL_3 is reported.

---

[8] The peak depicted by a * in Fig. 91 is in fact a mixture of reacted oligos (ligand+oligo) and unreacted oligos. Note that the unreacted oligos carry an exposed thiol group, whose interaction with exposed cysteines of the target protein can be inhibited by the use of reducing agents, e. g. tris(2-carboxyethyl)phosphine (TCEP). Consequently, they won't interfere with the measurments.

[9] The presented HaloTag unfolding pathway of Fig. 92 is not the only one observed, but the most frequent, observed in more than 80 % of the measured proteins. Moreover, the unfolding force depends on the pulling speed, ranging from 15 to 30 pN.

[10] The measurement of the expected CL gain from the crystal structure (PDB id: 4KAF) is not straightforward. The structured amino acids start from residue 12, that is separated by 2.4 nm from residue 35 in the folded conformation. Assuming the unraveling of residues 12–35, the expected CL gain would be $24 \times 0.365\,\text{nm} - 2.4\,\text{nm} = 6.4\,\text{nm}$. Assuming instead the unravelling of all 35 amino acids, the initial separation is hard to estimate (there is no structure of the first 12 amino acids), while the total CL of the region would be 12.8 nm. The observed CL gain could indicate the presence of intermediate conditions, but a more precise analysis is not possible based on these data. On the other hand, the last 29 amino acids of the tag would lead to a lower CL gain, of about 5 nm.

Driving the system to forces above 30 pN and keeping it in passive mode (Fig. 92C) reveals a further unfolding event within a couple of seconds, associated with a CL increase $\Delta L_3 = 22 \pm 1$ nm. The CL gain of this event is a slightly shorter than that observed for the N-HaloTag (see Table 2), while the lower unfolding forces compared to the AFM experiments can be explained by the use of different measuring assays: a protein can resist to significantly higher forces before unfolding if pulled by fast force ramps, compared to passive-mode experiments.[11]

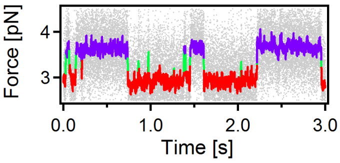

Fig. 93. Passive-mode trace of PullA-T7(halo) construct in the low force range. Three states can be recognised, as in the analogous PullA-T7 construct explored in Sec. 5.2.

The resolution of the experiments below 10 pN, i. e. before the HaloTag starts unravelling (ΔL_2), is not harmed by the presence of the tags: A passive-mode experiment was performed at 3.5 pN of pretension, and the transition ΔL_1 of Fig. 92B shows the typical three-state network of the PullA-T7 geometry (Fig. 93, to be compared with Fig. 40). The data have the same resolution and lead to the same extracted kinetics as the cysteine-based conjugation technique. Hence, it can be asserted that the HaloTag approach is appropriate for the study of molecular interactions below 10 pN. At higher forces, unravelling of parts of the tag may hamper the investigation of the protein under study. In the next chapter, an application of the HaloTag technology is presented.

B.7 INTERACTION OF α-ACTININ 2 WITH THE NECK REGION

As introduced in Sec. 4.1 (Box 7), the regulatory model for α-actinin states that the EF3-4 domain of one subunit binds the neck region of the opposite subunit, thus inhibiting the binding of titin Z-repeats. In the Z-disk, the presence of PIP_2 decreases the affinity of the EF3-4 with the neck, thus enabling the recognition of titin Z-repeats.

Remarkably, only a truncation of α-actinin carring the ABD, the neck and the SR1 showed a measurable affinity with the EF3-4, while the binding of the neck peptide lacking the neighbouring domains was never observed. Using the same strategy adopted to probe the interaction of EF3-4 with several titin Z-repeats (Sec. 6.1), a fusion construct of EF3-4 and the neck was created (named pullA-neck), with N- and C-termini pulling position. Since the neck region carries a cystein in one of the four key binding positions (see Table 2), the only way of measuring such interactions using the standard cysteine modification is to mutate the cysteine present in the neck with another residue (complete sequences in appendix C.3). In this case a valine residue was chosen, because it is the most common residue present in that position in the titin Z-repeats.

---

[11] This behaviour, known as the *Bell-Evans effect*, is related to the loading-rate dependence of the rupture force [39].

The pullA-neck construct reveals a very weak interaction between the EF3-4 and the neck (Fig. 94). The free-energy of the binding is only 0.2 $k_{\mathrm{B}}T$, and the calculated affinity (see Sec. 6.1) is 0.24 ± 0.16 mM.

In parallel, a construct with two HaloTags at the termini and the original internal cysteine in the neck was designed. This construct, named PullA-neck(halo), is analog to the PullA-T7(halo) described in the previous section, with the substitution of the T7 peptide with the native neck sequence. The binding energy extracted with the native sequence and the valine-mutated construct are compatible, showing that the low affinity is not due to the point mutation, but rather to the lacking of the neck neighbouring domains.

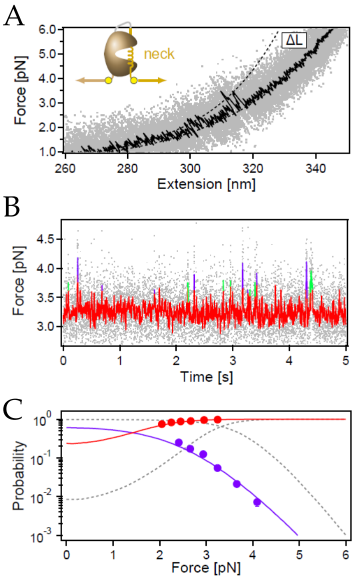

FIG. 94. PullA-neck construct under force. Colour coding as in Fig. 51. (A) Constant-velocity trace, with schematic of the construct. At very low forces, rapid transitions between the bound state and the unbound-/unfolded state can be observed. (B) Passive-mode trace. Three states can be identified from equilibrium traces, as for the other fusion constructs explained in Sec. 5.2. (C) Rate constants extracted from different passive-mode experiments. In grey, data from the PullA-T7 construct, for comparison.

B.8 YBBR TAG

The ybbR tag is an 11 amino acid sequence coming from the *Bacillus subtilis* genome. It was identified as a substrate for the Sfp phosphopantetheinyl transferase, an enzyme that catalyzes the covalent binding of small molecule carrying a coenzyme A (CoA) modification [131]. The tag is an excellent candidate for versatile labelling of target proteins, fulfilling all the criteria of Sec. B.2. Notably, the small size (only 11 residues) increases the portability: Labelling of target proteins was achieved not only with tag fusion to N- and C-termini, but also with tag insertion in flexible loop regions [131]. The tag has been successfully introduced in AFM studies, with high efficiency and short reaction times [95].

The main concern for optical tweezers applications is whether the peptide can fold in solution. A structured tag, as already discussed for the HaloTag in Secs. B.5 and B.6, may unravel at low forces, thus interfering with the unfolding events of the target protein. However, the sequence used in literature was reported to have an helix content of 35 % in acqueous TFE [44], which points to very low mechanical stability.

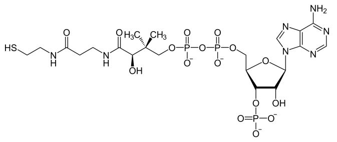

Fig. 95. Coenzyme A formula. The thiol group at the left hand can be coupled with maleimide-modified oligonucleotides, hence obtaining CoA-modified oligos.

To test the usability of the tag in a dual-beam optical tweezers setup, again the PullA-T7 fusion construct of Fig. 37 was used. Following the path B of Fig. 87—CoA acts as the ligand—two ybbR tags were substituted to replace the terminal cysteine residues, in a construct called pullA-T7(ybbR). CoA-modified oligos were employed (Biomers), that were produced by letting react CoA (formula in Fig. 95) with maleimide-modified oligos, in order to obtain a covalent irreversible bond, in the same way the HaloTag Ligand was coupled to thiol-modified oligos in Sec. B.6. Again, the size of the CoA ligand (0.8 kDa) is significantly smaller than that of the oligonucleotide (11 kDa), thus the unreacted CoA can be separated from the oligos by size-exclusion chromatography. The pullA-T7(ybbR) construct was further incubated with the CoA-modified oligos obtained in the previous step, with the addition of the Sfp enzyme. By using size-exclusion chromatography, the fraction containing proteins with two oligos attached could be isolated (more details in appendix C.6).[12]

Data collected with the PullA-T7(ybbR) construct were perfectly compatible with standard cysteine-modified PullA-T7 proteins. In Fig. 96A the typical unbinding/unfolding of the construct is visible, compatible with the original cysteine construct (PullA-T7, Fig. 38) and the first event ΔL_1 of the HaloTag construct (PullA-T7(halo), Fig. 92B). No further unfolding events nor increase in the noise were observed above 2 pN, which is the threshold for detectable events,[13] confirming the prediction that eventual α-helical structures of the ybbR tag does not survive high mechanical load. The resolution at low forces can be tested with passive-mode experiments. A trace excerpt is shown in Fig. 96B. The typical three-state network of the fusion construct could be successfully assigned to the data using the HMM analysis, as in the PullA-T7 construct (Fig. 40). Moreover, measurements could be carried out for tens of minutes, as expected for a successful covalent conjugation.

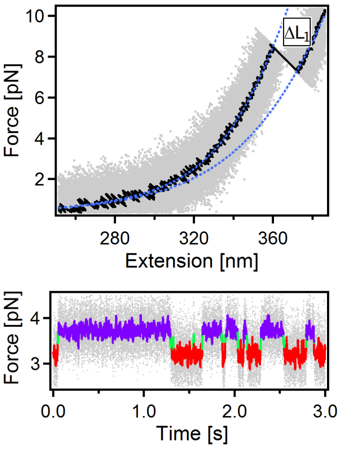

Fig. 96. PullA-T7(ybbR) construct. (A) Force ramp at 100 pN/s, showing a single peak with a CL gain of $\Delta L_1 = 33.7$ pN. (B) Passive-mode trace, with the typical three states of the EF3-4 and T7 fusion construct.

---

[12] By this fractionating step, also the Sfp enzyme is removed from the sample.

[13] The resolution of the instrument increases with the applied load. In the hypothesis that all 11 amino acids of the ybbR tag adopt an α-helical conformation, the CL gain upon unfolding would be about 2 nm, a distance that can be resolved at not less than 8–10 pN. In the force range from 3 to 10 pN, fast unfolding/refolding events lead to noise increase. In the PullA-T7(ybbR) data, no significant noise increase was observed.

The ybbR tag conjugation is thus a valid cysteine-free method to couple proteins and nucleid acids for optical tweezers applications.

B.9 SUMMARY

Among the range of alternative bioconjugation methods to couple a target protein to DNA molecules, two similar strategies have been employed in this chapter. They both consisted in recombinantly fusing certain peptide tags to the target protein, and link it to the oligonucleotides via certain binding partners (ligands).

The first probed tag, called the HaloTag, partly unravels at forces within the range of loads applicable with optical tweezers, although higher than 10 pN. These unfolding events may interfere with unfolding or unbinding events of the molecules under study, making the HaloTag a useful but not versatile tag for protein labelling. In addition, the big size of the tag does not allow its insertion within a protein loop. Nonetheless, the mechanical strength of the binding between the neck region and the EF3-4 domain of α-actinin could be probed using this strategy and keeping an original internal cysteine, thanks to the low mechanical stability of this bond.

The other investigated approach, i. e. labelling the protein with the small ybbR tag, has been shown not to alter the resolution of the data in the sensitive region between 2 and 5 pN. Moreover, no unfolding of the tag has been observed at high forces, making this approach a versatile method for protein/DNA coupling for optical tweezers experiments.

C

MATERIAL AND METHODS

The protocols used to prepare the biological samples are explained in detail in this chapter, together with the measuring procedure.

In Sec. C.1 the complete procedure used to express and purify the target proteins is described, followed by the experimental procedure (C.2). The protocols of these first two sections are complementary to those introduced in Sec. 2.5. Afterwards, the amino acid sequences of all proteins used for the study of the α-actinin/titin interaction (C.3) and the talin/integrin interaction (C.4) are reported. The last part of the chapter deals with the protocols for alternative bioconjugation techniques, namely the HaloTag (C.5) and the ybbR tag (C.6) conjugations.

C.1 CLONING AND EXPRESSION

All constructs presented in this thesis, with exception of appendix B, were cloned in pet28a vectors, which contain a C-terminal His6-tag. The vectors were transformed and expressed in E. coli BL21 (DE3). The expression was induced by addition of 1mM isopropyl β-D-1-thiogalactopyranoside (IPTG) at OD600 = 0.6 in 500 ml for 2 h in LB0 buffer, at the temperature of 37 °C. The proteins were further purified in two steps, first using affinity chromatography (NI-NTA column, QIAGEN), then by size exclusion chromatography (Superdex 200 10/300 GL column, GE Healthcare).

The oligonucleotides coupled to the proteins carried the sequence `5'-GGCAGGGCTGACGTTCAACCAGACCAGCGAGTCG-Maleimide 3'`. The oligos were incubated at a ratio 2:1 with the target proteins, for 2 h at room temperature. The proteins with two oligos bound were purified using size exclusion chromatography (Superdex 200 10/300 GL column, GE Healthcare).

C.2 EXPERIMENTAL PROTOCOL

The dsDNA handles have a contour length of 175 nm. The protein-oligos-handles construct was incubated with 1-µm-sized streptavidin-coated silica beads (Bang laboratories). The other sort of beads are similar silica beads (Bang laboratories) functionalized with anti-digoxigenin Fab fragments (Roche). All data were recorded at 23 °C in 10 mM PBS, 2.7 mM KCl, and 140 mM NaCl, pH 7.4, with the addition of an oxygen scavenger system consisting of 26 U/ml glucose oxidase, 1700 U/ml catalase, and 0.66 % glucose, to reduce photodamage of the protein [66]. The chambers used to measure were made by two 170-µm-thick coverslips (Carl Roth) attached with Parafilm (Bemis Company). The passivation of the surface was obtained with addition of 10 mg/ml BSA (Sigma-Aldrich), to prevent beads from sticking. The chambers were washed with measuring buffer before addition of the final solution.

C.3 PROTEIN SEQUENCES FOR THE STUDY OF α-ACTININ/TITIN INTERACTION

With the exception of the PullT7 construct, all other fusion construct carried two ubiquitin domains between the protein and the terminal cysteines, in order to prevent disulfide bonds formation. Ubiquitins have a high mechanical stability, thus they unfold at forces higher than those applied in this work [103]. In the EF3-4 (human) domain, an internal cysteine (`C862`) was mutated to prevent unwanted coupling with oligonucleotides. A structurally similar serine was employed. In analogy, in the neck region a cystein (`C270`) was mutated to a valine (see Sec. B.7). To better compare the results with literature, the rabbit titin sequences were employed. The residue numbers come from UniProtKB - O97791. Rabbit Z-repeats are highly homologous with the human orthologues [56]. Peptides T1, T5 and T7 fused to EF3-4 are identical in the two species, while T3, T2 and T7long[1] differ by one, two and five amino acids respectively, none of them in the key binding positions.

The amino acid sequences of the single domains and peptides are listed below:
ubi: `MQIFVKTLTGKTITLEVEPSDTIENVKAKIQDKEGIPPDQQRLI-`

---

[1] T7long has been employed in the competition assay

FAGKQLEDGRTLSDYNIQKESTLHLVLRLR

GGS_link: GGSGGSGGSGGS

EF3-4_C862S: ADTDTAEQVIASFRILASDKPYILAEELRRELPPDQAQYSIKRMPAYSGPGSVPGALDYAAFSSALYGESDL

T1: ADKSAAVATVVAAVDMARVREPV (422–444)

T2: EAEKIAVSKVVVAADKAKEQELK (472–494)

T3: GTEKAFVPKVVISAAKAKEQET (518–539)

T5: ETRKTVVPKVIVATPKVKEQDLV (562–584)

T7: GKKAEAVATVVAAVDQARVREPR (654–676, fusion constructs)

T7long: KVGVGKKAEAVATVVAAVDQARVREPREPGLPEDSYAQQTTLEYGYKEH (650–698, used in all competition assays)

neck: AEQAETAANRICKVLAVNQENERLME (259–284)

neck_C270V: AEQAETAANRIVKVLAVNQENERLME (259–284)

HaloTag: EIGTGFPFDPHYVEVLGERMHYVDVGPRDGTPVLFLHGNPTSSYVWRNIIPHVAPTHRCIAPDLIGMGKSDKPDLGYFFDDHVRFMDAFIEALGLEEVVLVIHDWGSALGFHWAKRNPERVKGIAFMEFIRPIPTWDEWPEFARETFQAFRTTDVGRKLIIDQNVFIEGTLPMGVVRPLTEVEMDHYREPFLNPVDREPLWRFPNELPIAGEPANIVALVEEYMDWLHQSPVPKLLFWGTPGVLIPPAEAARLAKSLPNCKAVDIGPGLNLLQEDNPDLIGSEIARWLSTLEIS

ybbR_tag: DSLEFIASKLA

The fusion constructs were created combining the domains, as follows:

PullA-T7: ACK (ubi) SSGEL (EF3-4_C862S) (GGS_link) (T7) GGSGGT (ubi) GGKCLEHHHHHH

PullA-T1: ACK (ubi) SSGEL (EF3-4_C862S) (GGS_link) (T1) GGSGGT (ubi) GGKCLEHHHHHH

PullA-T2: ACK (ubi) SSGEL (EF3-4_C862S) (GGS_link) (T2) GGSGGT (ubi) GGKCLEHHHHHH

PullA-T3: ACK (ubi) SSGEL (EF3-4_C862S) (GGS_link) (T3) GGSGGT (ubi) GGKCLEHHHHHH

PullA-T5: ACK (ubi) SSGEL (EF3-4_C862S) (GGS_link) (T5) GGSGGT (ubi) GGKCLEHHHHHH

PullA-neck: ACK (ubi) SSGEL (EF3-4_C862S) (GGS_link) (neck_C270V) GGSGGT (ubi) GGKCLEHHHHHH

PullT7: ASK(EF3-4_C862S) (GGS_link) C VGV (T7) KCLEHHHHHH

PullA-T7(halo): (HaloTag) SGEL (EF3-4_C862S) (GGS_link) (T7) GGSGGS (HaloTag) LEHHHHHH

PullA-neck(halo): (HaloTag) SGEL (EF3-4_C862S) (GGS_link) (neck) GGSGGS (HaloTag) LEHHHHHH

PullA-T7(ybbR): (ybbR_tag) GGG (ubi) (EF3-4_C862S) (GGS_link) (T7) SGSGSGS (ybbR_tag) LEHHHHHH

The quality of the purified constructs was assessed by SDS-Page and mass spectrometry.

C.4 PROTEIN SEQUENCES FOR THE STUDY OF TALIN/INTEGRIN INTERACTION

The C-terminal domain F3 of talin was employed in all constructs, together with the cytoplasmic tail of integrin. The sequences of the domains and the peptides employed are:
talin1: `GVSFFLVKEKMKGKNKLVPRLLGITKESVMRVDEKTKEVIQEWSLTNIKRWAASPKSFTLDFGDYQDGYYSVQTTEGEQIAQLIAGYIDIILKKKKS`
talin2: `GVSFFLVKEKMKGKNKLVPRLLGITKDSVMRVDEKTKEVLQEWPLTTVKRWAASPKSFTLDFGEYQESYYSVQTTEGEQISQLIAGYIDIILKKKQS`
SGGG_link: `SGGGSGGGSGGGSGGGSGGGSGGGSGG`
long_link: `ASGGGSAGGSGSGSSGGSSGASGTGTAGGTGSGSGTGSGGGSGGGSEGGGSEGGGSEGGGSEGGGSEGGGSGGGS`
β1A: `HDRREFAKFEKEKMNAKWDTGENPIYKSAVTTVVNPKYEGK`
β1D: `HDRREFAKFEKEKMNAKWDTQENPIYKSPINNFKNPNYGRKAGL`
β1D_V: `HDRREFAKFEKEKMNAKWVENPIYKSPINNFKNPNYGRKAGL`
β1D_noMP: `SGGGSGGGSGGGSGGAKWDTQENPIYKSPINNFKNPNYGRKAGL`

The fusion constructs employed in chapter 8 and 9 are listed below:
T1-β1A: `C` (talin1) (`SGGG`_link) `C G` (β1A)
T2-β1D: `C` (talin2) (`SGGG`_link) `C G` (β1D)
T2-β1D_noMP: `C` (talin2) (`SGGG`_link) `C G` (β1D_noMP)
T1-β1A_LL: `C` (talin2) (long_link) `C G` (β1D)
T2-β1D_LL: `C` (talin2) (long_link) `C G` (β1D)

C.5 PROTOCOL FOR HALOTAG CONJUGATION

To obtain the HaloTag-modified proteins presented in Sec. B.6, two reactions were carried out. First the iodacetamide HaloLigand were reacted with thiol-modified oligonucleotides, and purified. Second, the oligo-ligand reaction was incubated with the HaloTag protein. The full protocols are presented here.

BOX 16. ETOH PRECIPITATION

1. Add 1/10 volume Na-Acetate (3M, pH 5.2)
2. Add 2 volumes pure EtOH (100 %)
3. Keep for 60 min at −80 °C
4. Centrifuge 15 min at max speed in the 0 °C centrifuge
5. Remove the supernatant
6. Add 200 µl 100 % EtOH
7. Centrifuge 5 min at max speed in the 0 °C centrifuge
8. Remove the supernatant
9. Dry the tube at 37 °C for 10 min, or until EtOH evaporates
10. Resuspend the pellet in buffer

The conjugation of thiol oligos with the HaloLigand is performed as follows:

1. Take 100 nmol of thiol-modified oligos, reduce them with tris(2-carboxyethyl)phosphine (TCEP), and remove TCEP with ethanol (EtOH) precipitation (Box 16). Resuspend the oligos in 400 µl PBS pH 8.

2. Elute 5 mg of iodacetamide HaloLigand in inert chamber with 500 µl dimethyl sulfoxide (DMSO). The final concentration should be about 20 mM (the HaloLigand molecular mass is about 0.5 kDa). The iodacetamide group hydrolise rapidly, thus it is fundamental to be fast in this step (also to avoid redimerisation of the thiol oligos).

3. Add 100 µl ligand to 400 µl of thiol oligos (molar ratio 20:1) and let react for 2 h at room temperature.

4. Use size exclusion chromatography (Superdex 200 10/300 GL column, GE Healthcare) to separate the unreacted ligand from the ligand+oligo (Fig. 91).

5. Pool the fraction corresponding to the wanted peak and concentrate to get a final concentration in the order of 50µM.

The second set of reactions with the HaloTag-modified proteins were perfomed by adding together:

- 4 nmol of ligand+oligos (e. g. 60 µl at 70 µM)
- 1 nmol of protein (e. g. 40 µl at 25 µM)
- 1 mM (final concentration) of TCEP

The necessary oligo:protein ratio (4:1) was higher than in the standard cysteine protocol, probably because the coupling with the HaloLigand didn't have a 100 % efficiency. The reaction was carried out over night at 4 °C, and again purified with size exclusion chromatography (Superdex 200 10/300 GL column, GE Healthcare) to isolate the fraction corresponding to a protein with two attached oligonucleotides.

C.6 PROTOCOL FOR YBBR CONJUGATION

The ybbR-tag variant of the PullA-T7 construct—called PullA-T7(ybbR)—presented in Sec. B.8 has a sequence that can be found in Sec. C.3. The protein was designed with the following sequence:
`M` (initial codon)
`DSLEFIASKLA` (ybbR Tag)
`GGG` (spacer)
Protein of interest
`SGSGSGS` (longer spacer)
`DSLEFIASKLA` (ybbR Tag)
`LEHHHHHH` (His Tag)
It is important to note that the the second spacer is longer. The reason is that the second amino acid of the ybbR tag (a serine) is covalently bound to CoA via an enzymatic reaction, and a longer linker may facilitate the reaction.

The covalent coupling of the protein—carrying two ybbR tags—and the CoA-modified oligonucleotides is catalyzed by the Sfp phosphopantetheinyl transferase (Sfp). A 10× Hepes buffer pH 7.5 was employed (500 mM Hepes and 100 mM $MgCl_2$) with addition of magnesium, required for the Sfp enzymatic activity.

The compounds were mixed as follows:

- 2 nmol of CoA-oligos (e. g. 20 µl at 100 µM)
- 0.5 nmol of protein (e. g. 10 µl at 50 µM)
- 0.4 nmol of Sfp enzyme (e. g. 10 µl at 40 µM)
- 10× Sfp buffer (in this case, 10 µl)

The reaction was carried out over night at 4 °C, but a few hours at room temperature should be sufficient as well.

BIBLIOGRAPHY

[1] B. R. Anderson and H. L. Granzier. “Titin-based tension in the cardiac sarcomere: molecular origin and physiological adaptations.” *Prog Biophys Mol Biol* 110.2-3 (2012), pp. 204–17.

[2] B. R. Anderson and H. L. Granzier. “Biophysics of Titin in Cardiac Health and Disease.” *Biophysics of the Failing Heart*. Ed. by R. J. Solaro and J. C. Tardiff. New York, NY: Springer New York, 2013, pp. 201–223.

[3] N. J. Anthis and I. D. Campbell. “The tail of integrin activation.” *Trends in Biochemical Sciences* 36.4 (Apr. 2011), pp. 191–198.

[4] N. J. Anthis et al. “The structure of an integrin/talin complex reveals the basis of inside-out signal transduction.” *The EMBO journal* 28.22 (Nov. 2009), pp. 3623–3632.

[5] N. J. Anthis, K. L. Wegener, D. R. Critchley, and I. D. Campbell. “Structural Diversity in Integrin/Talin Interactions.” *Structure (London, England : 1993)* 18.12 (Dec. 2010), p. 1654.

[6] G. Žoldák, J. Stigler, B. Pelz, H. Li, and M. Rief. “Ultrafast folding kinetics and cooperativity of villin headpiece in single-molecule force spectroscopy.” *Proceedings of the National Academy of Sciences* 110.45 (Nov. 2013), pp. 18156–18161.

[7] A. Ashkin, J. M. Dziedzic, and T. Yamane. “Optical trapping and manipulation of single cells using infrared laser beams.” *Nature* 330.6150 (Dec. 1987), pp. 769–771.

[8] A. Ashkin and J. Dziedzic. “Optical trapping and manipulation of viruses and bacteria.” *Science* 235.4795 (1987), pp. 1517–1520.

[9] M. Atakhorrami, K. M. Addas, and C. F. Schmidt. “Twin optical traps for two-particle cross-correlation measurements: Eliminating crosstalk.” *Review of Scientific Instruments* 79.4 (2008), p. 043103.

[10] R. A. Atkinson, C. Joseph, G. Kelly, F. W. Muskett, T. A. Frenkiel, D. Nietlispach, and A. Pastore. “Ca2+-independent binding of an EF-hand domain to a novel motif in the alpha-actinin-titin complex.” *Nat Struct Biol* 8.10 (2001), pp. 853–7.

[11] M.-E. Aubin-Tam, A. O. Olivares, R. T. Sauer, T. A. Baker, and M. J. Lang. “Single-molecule protein unfolding and translocation by an ATP-fueled proteolytic machine.” *Cell* 145.2 (Apr. 2011), pp. 257–267.

[12] E. L. Baker and M. H. Zaman. “The biomechanical integrin.” *Journal of Biomechanics* 43.1 (Jan. 2010), pp. 38–44.

[13] A. M. Belkin, N. I. Zhidkova, F. Balzac, F. Altruda, D. Tomatis, A. Maier, G. Tarone, V. E. Koteliansky, and K. Burridge. "Beta 1D integrin displaces the beta 1A isoform in striated muscles: localization at junctional structures and signaling potential in nonmuscle cells." *The Journal of Cell Biology* 132.1-2 (Jan. 1996), pp. 211–226.

[14] G. I. Bell. "Models for the specific adhesion of cells to cells." *Science* 200.4342 (May 1978), pp. 618–627.

[15] M. Bertz, M. Wilmanns, and M. Rief. "The titin-telethonin complex is a directed, superstable molecular bond in the muscle Z-disk." *Proc Natl Acad Sci U S A* 106.32 (2009), pp. 13307–133310.

[16] S. M. Block, L. S. Goldstein, and B. J. Schnapp. "Bead movement by single kinesin molecules studied with optical tweezers." *Nature* 348.6299 (Nov. 1990), pp. 348–352.

[17] D. A. Calderwood, B. Yan, J. M. d. Pereda, B. n. G. Alvarez, Y. Fujioka, R. C. Liddington, and M. H. Ginsberg. "The Phosphotyrosine Binding-like Domain of Talin Activates Integrins." *Journal of Biological Chemistry* 277.24 (June 2002), pp. 21749–21758.

[18] M. J. Comstock, K. D. Whitley, H. Jia, J. Sokoloski, T. M. Lohman, T. Ha, and Y. R. Chemla. "Direct observation of structure-function relationship in a nucleic acid–processing enzyme." *Science* 348.6232 (Apr. 2015), pp. 352–354.

[19] F. J. Conti, A. Felder, S. Monkley, M. Schwander, M. R. Wood, R. Lieber, D. Critchley, and U. Müller. "Progressive myopathy and defects in the maintenance of myotendinous junctions in mice that lack talin 1 in skeletal muscle." *Development* 135.11 (June 2008), pp. 2043–2053.

[20] G. E. Crooks. "Entropy production fluctuation theorem and the nonequilibrium work relation for free energy differences." *Physical Review E* 60.3 (Sept. 1999), pp. 2721–2726.

[21] A. A. Deniz, S. Mukhopadhyay, and E. A. Lemke. "Single-molecule biophysics: at the interface of biology, physics and chemistry." *Journal of The Royal Society Interface* 5.18 (Jan. 2008), pp. 15–45.

[22] K. A. Dill and J. L. MacCallum. "The Protein-Folding Problem, 50 Years On." *Science* 338.6110 (2012), pp. 1042–1046.

[23] M. Du and R. J. McCormick. *Applied Muscle Biology and Meat Science*. CRC Press, May 2009.

[24] S. W. Englander and L. Mayne. "The nature of protein folding pathways." *Proceedings of the National Academy of Sciences of the United States of America* 111.45 (Nov. 2014), pp. 15873–15880.

[25] E. Evans and K. Ritchie. "Dynamic strength of molecular adhesion bonds." *Biophysical Journal* 72.4 (Apr. 1997), pp. 1541–1555.

[26] J. M. Ferrer, H. Lee, J. Chen, B. Pelz, F. Nakamura, R. D. Kamm, and M. J. Lang. "Measuring molecular rupture forces between single actin filaments and actin-binding proteins." *Proceedings of the National Academy of Sciences of the United States of America* 105.27 (July 2008), pp. 9221–9226.

[27] J. T. Finer, R. M. Simmons, and J. A. Spudich. "Single myosin molecule mechanics: piconewton forces and nanometre steps." *Nature* 368.6467 (Mar. 1994), pp. 113–119.

[28] A. Freiburg and M. Gautel. "A molecular map of the interactions between titin and myosin-binding protein C - Implications for sarcomeric assembly in familial hypertrophic cardiomyopathy." *European Journal of Biochemistry* 235.1-2 (1996), pp. 317–323.

[29] K. Fujita, M. Iwaki, A. H. Iwane, L. Marcucci, and T. Yanagida. "Switching of myosin-V motion between the lever-arm swing and Brownian search-and-catch." *Nature Communications* 3 (July 2012), p. 956.

[30] J. J. Funke, P. Ketterer, C. Lieleg, S. Schunter, P. Korber, and H. Dietz. "Uncovering the forces between nucleosomes using DNA origami." *Science Advances* 2.11 (Nov. 2016), e1600974.

[31] B. n. García-Alvarez, J. M. d. Pereda, D. A. Calderwood, T. S. Ulmer, D. Critchley, I. D. Campbell, M. H. Ginsberg, and R. C. Liddington. "Structural Determinants of Integrin Recognition by Talin." *Molecular Cell* 11.1 (Jan. 2003), pp. 49–58.

[32] S. Garcia-Manyes, C. L. Badilla, J. Alegre-Cebollada, Y. Javadi, and J. M. Fernández. "Spontaneous Dimerization of Titin Protein Z1Z2 Domains Induces Strong Nanomechanical Anchoring." *The Journal of Biological Chemistry* 287.24 (June 2012), p. 20240.

[33] M. Gautel. "The sarcomeric cytoskeleton: who picks up the strain?" *Curr Opin Cell Biol* 23.1 (2011), pp. 39–46.

[34] M. Gautel and K. Djinovic-Carugo. "The sarcomeric cytoskeleton: from molecules to motion." *J Exp Biol* 219.Pt 2 (2016), pp. 135–45.

[35] M. Gautel, D. Goulding, B. Bullard, K. Weber, and D. O. Furst. "The central Z-disk region of titin is assembled from a novel repeat in variable copy numbers." *Journal of Cell Science* 109 (1996), pp. 2747–2754.

[36] A. Gautier, A. Juillerat, C. Heinis, I. R. Corrêa, M. Kindermann, F. Beaufils, and K. Johnsson. "An engineered protein tag for multiprotein labeling in living cells." *Chemistry & Biology* 15.2 (Feb. 2008), pp. 128–136.

[37] J. C. M. Gebhardt, T. Bornschlögl, and M. Rief. "Full distance-resolved folding energy landscape of one single protein molecule." *Proceedings of the National Academy of Sciences of the United States of America* 107.5 (Feb. 2010), pp. 2013–2018.

[38] M. A. Geeves and K. C. Holmes. "Structural mechanism of muscle contraction." *Annual Review of Biochemistry* 68 (1999), pp. 687–728.

[39] C. Gergely, J.-C. Voegel, P. Schaaf, B. Senger, M. Maaloum, J. K. H. Hörber, and J. Hemmerlé. "Unbinding process of adsorbed proteins under external stress studied by atomic force microscopy spectroscopy." *Proceedings of the National Academy of Sciences* 97.20 (Sept. 2000), pp. 10802–10807.

[40] J. M. Glück, M. Wittlich, S. Feuerstein, S. Hoffmann, D. Willbold, and B. W. Koenig. "Integral Membrane Proteins in Nanodiscs Can Be Studied by Solution NMR Spectroscopy." *Journal of the American Chemical Society* 131.34 (Sept. 2009), pp. 12060–12061.

[41] W. H. Goldmann and G. Isenberg. "Analysis of filamin and alpha-actinin binding to actin by the stopped flow method." *FEBS letters* 336.3 (Dec. 1993), pp. 408–410.

[42] M. González, L. A. Bagatolli, I. Echabe, J. L. R. Arrondo, C. E. Argaraña, C. R. Cantor, and G. D. Fidelio. "Interaction of Biotin with Streptavidin. Thermostability and conformational changes upon binding." *Journal of Biological Chemistry* 272.17 (Apr. 1997), pp. 11288–11294.

[43] H. L. Granzier and S. Labeit. "The giant protein titin: a major player in myocardial mechanics, signaling, and disease." *Circ Res* 94.3 (2004), pp. 284–95.

[44] N. Greenfield and G. D. Fasman. "Computed circular dichroism spectra for the evaluation of protein conformation." *Biochemistry* 8.10 (Oct. 1969), pp. 4108–4116.

[45] C. C. Gregorio et al. "The NH2 terminus of titin spans the Z-disc: its interaction with a novel 19-kD ligand (T-cap) is required for sarcomeric integrity." *The Journal of Cell Biology* 143.4 (Nov. 1998), pp. 1013–1027.

[46] C. C. Gregorio, H. Granzier, H. Sorimachi, and S. Labeit. "Muscle assembly: a titanic achievement?" *Curr Opin Cell Biol* 11.1 (1999), pp. 18–25.

[47] Y. von Hansen, A. Mehlich, B. Pelz, M. Rief, and R. R. Netz. "Auto- and cross-power spectral analysis of dual trap optical tweezer experiments using Bayesian inference." *Review of Scientific Instruments* 83.9 (2012), p. 095116.

[48] A. Houmeida, J. Holt, L. Tskhovrebova, and J. Trinick. "Studies of the Interaction between Titin and Myosin." *Journal of Cell Biology* 131.6 (1995), pp. 1471–1481.

[49] J Howard, A. Hudspeth, and R. Vale. "Movement of microtubules by single." *Nature* 342 (1989), p. 9.

[50] A. F. Huxley and R. Niedergerke. "Structural Changes in Muscle During Contraction: Interference Microscopy of Living Muscle Fibres." *Nature* 173.4412 (May 1954), pp. 971–973.

[51] H. Huxley and J. Hanson. "Changes in the Cross-Striations of Muscle during Contraction and Stretch and their Structural Interpretation." *Nature* 173.4412 (May 1954), pp. 973–976.

[52] R. O. Hynes. "Integrins: bidirectional, allosteric signaling machines." *Cell* 110.6 (Sept. 2002), pp. 673–687.

[53] M. Ibrahim et al. "A critical role for Telethonin in regulating t-tubule structure and function in the mammalian heart." *Human Molecular Genetics* 22.2 (Jan. 2013), pp. 372–383.

[54] M. Itoh-Satoh et al. "Titin mutations as the molecular basis for dilated cardiomyopathy." *Biochem Biophys Res Commun* 291.2 (2002), pp. 385–93.

[55] M. Jahn, J. Buchner, T. Hugel, and M. Rief. "Folding and assembly of the large molecular machine Hsp90 studied in single-molecule experiments." *Proc Natl Acad Sci U S A* 113.5 (2016), pp. 1232–7.

[56] C. Joseph, G. Stier, R. O'Brien, A. S. Politou, R. A. Atkinson, A. Bianco, J. E. Ladbury, S. R. Martin, and A. Pastore. "A structural characterization of the interactions between titin Z-repeats and the alpha-actinin C-terminal domain." *Biochemistry* 40.16 (2001), pp. 4957–65.

[57] A. C. Kalli, K. L. Wegener, B. T. Goult, N. J. Anthis, I. D. Campbell, and M. S. P. Sansom. "The structure of the talin/integrin complex at a lipid bilayer: an NMR and MD simulation study." *Structure (London, England: 1993)* 18.10 (Oct. 2010), pp. 1280–1288.

[58] A. Keppler, S. Gendreizig, T. Gronemeyer, H. Pick, H. Vogel, and K. Johnsson. "A general method for the covalent labeling of fusion proteins with small molecules in vivo." *Nature Biotechnology* 21.1 (Jan. 2003), pp. 86–89.

[59] F. Kilchherr, C. Wachauf, B. Pelz, M. Rief, M. Zacharias, and H. Dietz. "Single-molecule dissection of stacking forces in DNA." *Science (New York, N.Y.)* 353.6304 (Sept. 2016).

[60] J. Kim, C.-Z. Zhang, X. Zhang, and T. A. Springer. "A mechanically stabilized receptor–ligand flex-bond important in the vasculature." *Nature* 466.7309 (Aug. 2010), pp. 992–995.

[61] F. Kong, A. J. García, A. P. Mould, M. J. Humphries, and C. Zhu. "Demonstration of catch bonds between an integrin and its ligand." *The Journal of cell biology* 185.7 (2009), pp. 1275–1284.

[62] V. M. Krishnamurthy, L. A. Estroff, and G. M. Whitesides. "Multivalency in Ligand Design." *Fragment-based Approaches in Drug Discovery*. Ed. by W. Jahnke and D. A. Erlanson. Wiley-VCH Verlag GmbH & Co. KGaA, 2006, pp. 11–53.

[63] S. K. Kufer, H. Dietz, C. Albrecht, K. Blank, A. Kardinal, M. Rief, and H. E. Gaub. "Covalent immobilization of recombinant fusion proteins with hAGT for single molecule force spectroscopy." *European biophysics journal: EBJ* 35.1 (Dec. 2005), pp. 72–78.

[64] S. Labeit and B. Kolmerer. "Titins: giant proteins in charge of muscle ultrastructure and elasticity." *Science (New York, N.Y.)* 270.5234 (Oct. 1995), pp. 293–296.

[65] S. Labeit, B. Kolmerer, and W. A. Linke. "The giant protein titin. Emerging roles in physiology and pathophysiology." *Circulation Research* 80.2 (Feb. 1997), pp. 290–294.

[66] M. P. Landry, P. M. McCall, Z. Qi, and Y. R. Chemla. "Characterization of Photoactivated Singlet Oxygen Damage in Single-Molecule Optical Trap Experiments." *Biophysical Journal* 97.8 (Oct. 2009), pp. 2128–2136.

[67] H. Li, W. A. Linke, A. F. Oberhauser, M. Carrion-Vazquez, J. G. Kerkvliet, H. Lu, P. E. Marszalek, and J. M. Fernandez. "Reverse engineering of the giant muscle protein titin." *Nature* 418.6901 (2002), pp. 998–1002.

[68] L. Li, J. O. Fierer, T. A. Rapoport, and M. Howarth. "Structural analysis and optimization of the covalent association between SpyCatcher and a peptide Tag." *Journal of Molecular Biology* 426.2 (Jan. 2014), pp. 309–317.

[69] Z. Li, M. K. Delaney, K. A. O'Brien, and X. Du. "Signaling during platelet adhesion and activation." *Arteriosclerosis, thrombosis, and vascular biology* 30.12 (Dec. 2010), pp. 2341–2349.

[70] W. A. Linke. "Sense and stretchability: the role of titin and titin-associated proteins in myocardial stress-sensing and mechanical dysfunction." *Cardiovasc Res* 77.4 (2008), pp. 637–48.

[71] W. A. Linke, M. Ivemeyer, S. Labeit, H. Hinssen, J. C. Rüegg, and M. Gautel. "Actin-titin interaction in cardiac myofibrils: probing a physiological role." *Biophysical Journal* 73.2 (Aug. 1997), pp. 905–919.

[72] S.-Q. Liu, X.-L. Ji, Y. Tao, D.-Y. Tan, K.-Q. Zhang, and Y.-X. Fu. "Protein Folding, Binding and Energy Landscape: A Synthesis." *Protein Engineering*. Ed. by P. Kaumaya. InTech, Feb. 2012.

[73] G. V. Los et al. "HaloTag: a novel protein labeling technology for cell imaging and protein analysis." *ACS chemical biology* 3.6 (June 2008), pp. 373–382.

[74] P. K. Luther, H. Winkler, K. Taylor, M. E. Zoghbi, R. Craig, R. Padron, J. M. Squire, and J. Liu. "Direct visualization of myosin-binding protein C bridging myosin and actin filaments in intact muscle." *Proc Natl Acad Sci U S A* 108.28 (2011), pp. 11423–8.

[75] P. K. Luther and J. M. Squire. "Muscle Z-band Ultrastructure: Titin Z-repeats and Z-band Periodicities Do Not Match." *Journal of Molecular Biology* 319.5 (2002), pp. 1157–1164.

[76] B. Ma, S. Kumar, C. J. Tsai, and R. Nussinov. "Folding funnels and binding mechanisms." *Protein Engineering* 12.9 (Sept. 1999), pp. 713–720.

[77] A. P. Maartens and N. H. Brown. "The many faces of cell adhesion during Drosophila muscle development." *Developmental Biology*. Cell Adhesion in Development 401.1 (May 2015), pp. 62–74.

[78] P. J. Mak, I. G. Denisov, Y. V. Grinkova, S. G. Sligar, and J. R. Kincaid. "Defining CYP3A4 Structural Responses to Substrate Binding. Raman Spectroscopic Studies of a Nanodisc-Incorporated Mammalian Cytochrome P450." *Journal of the American Chemical Society* 133.5 (Feb. 2011), pp. 1357–1366.

[79] S. R. Maloy, V. J. Stewart, and R. K. Taylor. *Genetic Analysis of Pathogenic Bacteria: A Laboratory Manual*. Cold Spring Harbor Laboratory Press, 1996.

[80] J. F. Marko and E. D. Siggia. "Stretching DNA." *Macromolecules* 28.26 (Dec. 1995), pp. 8759–8770.

[81] K. Maruyama, S. Matsubara, R. Natori, Y. Nonomura, and S. Kimura. "Connectin, an elastic protein of muscle. Characterization and Function." *Journal of Biochemistry* 82.2 (Aug. 1977), pp. 317–337.

[82] U. Mayer. "Integrins: Redundant or Important Players in Skeletal Muscle?" *Journal of Biological Chemistry* 278.17 (Apr. 2003), pp. 14587–14590.

[83] R. Merkel, P. Nassoy, A. Leung, K. Ritchie, and E. Evans. "Energy landscapes of receptor-ligand bonds explored with dynamic force spectroscopy." *Nature* 397.6714 (Jan. 1999), pp. 50–53.

[84] H. Miyata, R. Yasuda, and K. Kinosita. "Strength and lifetime of the bond between actin and skeletal muscle alpha-actinin studied with an optical trapping technique." *Biochimica Et Biophysica Acta* 1290.1 (May 1996), pp. 83–88.

[85] S. J. Monkley, C. A. Pritchard, and D. R. Critchley. "Analysis of the mammalian talin2 gene TLN2." *Biochemical and Biophysical Research Communications* 286.5 (Sept. 2001), pp. 880–885.

[86] C. Muhle-Goll, M. Habeck, O. Cazorla, M. Nilges, S. Labeit, and H. Granzier. "Structural and functional studies of titin's fn3 modules reveal conserved surface patterns and binding to myosin S1–a possible role in the Frank-Starling mechanism of the heart." *J Mol Biol* 313.2 (2001), pp. 431–47.

[87] M. K. Nahas, T. J. Wilson, S. Hohng, K. Jarvie, D. M. J. Lilley, and T. Ha. "Observation of internal cleavage and ligation reactions of a ribozyme." *Nature Structural & Molecular Biology* 11.11 (Nov. 2004), pp. 1107–1113.

[88] K. C. Neuman and A. Nagy. "Single-molecule force spectroscopy: optical tweezers, magnetic tweezers and atomic force microscopy." *Nature Methods* 5.6 (June 2008), pp. 491–505.

[89] A. A. R. Neves, A. Fontes, L. d. Y. Pozzo, A. A. de Thomaz, E. Chillce, E. Rodriguez, L. C. Barbosa, and C. L. Cesar. "Electromagnetic forces for an arbitrary optical trapping of a spherical dielectric." *Optics Express* 14.26 (2006), p. 13101.

[90] P. C. Nickels, B. Wünsch, P. Holzmeister, W. Bae, L. M. Kneer, D. Grohmann, P. Tinnefeld, and T. Liedl. "Molecular force spectroscopy with a DNA origami–based nanoscopic force clamp." *Science* 354.6310 (Oct. 2016), pp. 305–307.

[91] L. Oberbarnscheidt, R. Janissen, and F. Oesterhelt. "Direct and Model Free Calculation of Force-Dependent Dissociation Rates from Force Spectroscopic Data." *Biophysical Journal* 97.9 (Nov. 2009), pp. L19–L21.

[92] W. Ott, M. A. Jobst, C. Schoeler, H. E. Gaub, and M. A. Nash. "Single-molecule force spectroscopy on polyproteins and receptor-ligand complexes: The current toolbox." *Journal of Structural Biology* (Feb. 2016).

[93] S. Pernigo, A. Fukuzawa, M. Bertz, M. Holt, M. Rief, R. A. Steiner, and M. Gautel. "Structural insight into M-band assembly and mechanics from the titin-obscurin-like-1 complex." *Proc Natl Acad Sci U S A* 107.7 (2010), pp. 2908–13.

[94] R. Phillips, J. Kondev, J. Theriot, and H. Garcia. *Physical Biology of the Cell, Second Edition*. Garland Science, Oct. 2012.

[95] D. A. Pippig, F. Baumann, M. Strackharn, D. Aschenbrenner, and H. E. Gaub. "Protein-DNA chimeras for nano assembly." *ACS nano* 8.7 (July 2014), pp. 6551–6555.

[96] I. Popa, R. Berkovich, J. Alegre-Cebollada, C. L. Badilla, J. A. Rivas-Pardo, Y. Taniguchi, M. Kawakami, and J. M. Fernandez. "Nanomechanics of HaloTag Tethers." *Journal of the American Chemical Society* 135.34 (Aug. 2013), pp. 12762–12771.

[97] J. Ribeiro Ede A. et al. "The structure and regulation of human muscle alpha-actinin." *Cell* 159.6 (2014), pp. 1447–60.

[98] M. Rief, M. Gautel, F. Oesterhelt, J. M. Fernandez, and H. E. Gaub. "Reversible unfolding of individual titin immunoglobulin domains by AFM." *Science* 276.5315 (1997), pp. 1109–12.

[99] L. Rognoni, J. Stigler, B. Pelz, J. Ylanne, and M. Rief. "Dynamic force sensing of filamin revealed in single-molecule experiments." *Proc Natl Acad Sci U S A* 109.48 (2012), pp. 19679–84.

[100] L. Rognoni. "Molecular Mechanism of the Mechanosensor Filamin." PhD thesis. Techische Universität München, 2014.

[101] C. S. Roy. "The Elastic Properties of the Arterial Wall." *J Physiol* (1881).

[102] M. Schlierf, F. Berkemeier, and M. Rief. "Direct observation of active protein folding using lock-in force spectroscopy." *Biophys J* 93.11 (2007), pp. 3989–98.

[103] M. Schlierf, H. Li, and J. M. Fernandez. "The unfolding kinetics of ubiquitin captured with single-molecule force-clamp techniques." *Proc Natl Acad Sci U S A* 101.19 (2004), pp. 7299–304.

[104] K. da Silva Lopes, A. Pietas, M. H. Radke, and M. Gotthardt. "Titin visualization in real time reveals an unexpected level of mobility within and between sarcomeres." *J Cell Biol* 193.4 (2011), pp. 785–98.

[105] G. Sitters, D. Kamsma, G. Thalhammer, M. Ritsch-Marte, E. J. G. Peterman, and G. J. L. Wuite. "Acoustic force spectroscopy." *Nature Methods* 12.1 (Jan. 2015), pp. 47–50.

[106] B. Sjoblom, A. Salmazo, and K. Djinovic-Carugo. "Alpha-actinin structure and regulation." *Cell Mol Life Sci* 65.17 (2008), pp. 2688–701.

[107] S. B. Smith, Y. Cui, and C. Bustamante. "Overstretching B-DNA: The Elastic Response of Individual Double-Stranded and Single-Stranded DNA Molecules." *Science* 271.5250 (Feb. 1996), pp. 795–799.

[108] H Sorimachi, A Freiburg, B Kolmerer, S Ishiura, and G Stier. "Tissue-specific expression and alpha-actinin binding properties of the Z-disc titin : Implications for the nature of vertebrate Z-discs." *J Mol Biol* (1997), pp. 688–695.

[109] N. Stephanopoulos and M. B. Francis. "Choosing an effective protein bioconjugation strategy." *Nature Chemical Biology* 7.12 (Nov. 2011), pp. 876–884.

[110] J. Stigler and M. Rief. "Hidden Markov analysis of trajectories in single-molecule experiments and the effects of missed events." *Chemphyschem* 13.4 (2012), pp. 1079–86.

[111] J. Stigler. "Complex ligand-dependent folding of single proteins observed with optical tweezers." PhD thesis. Technische Universität München, 2012.

[112] A. L. Stout, J. Wang, J. M. Sanger, and J. W. Sanger. "Tracking changes in Z-band organization during myofibrillogenesis with FRET imaging." *Cell Motil Cytoskeleton* 65.5 (2008), pp. 353–67.

[113] Z. Sun, S. S. Guo, and R. Fässler. "Integrin-mediated mechanotransduction." *J Cell Biol* (Nov. 2016), jcb.201609037.

[114] K. Svoboda and S. M. Block. "Biological applications of optical forces." *Annual Review of Biophysics and Biomolecular Structure* 23 (1994), pp. 247–285.

[115] S. Tadokoro, S. J. Shattil, K. Eto, V. Tai, R. C. Liddington, J. M. d. Pereda, M. H. Ginsberg, and D. A. Calderwood. "Talin Binding to Integrin ß Tails: A Final Common Step in Integrin Activation." *Science* 302.5642 (Oct. 2003), pp. 103–106.

[116] Y. Taniguchi and M. Kawakami. "Application of HaloTag protein to covalent immobilization of recombinant proteins for single molecule force spectroscopy." *Langmuir: the ACS journal of surfaces and colloids* 26.13 (July 2010), pp. 10433–10436.

[117] I. Tessmer, P. Kaur, J. Lin, and H. Wang. "Investigating bioconjugation by atomic force microscopy." *Journal of Nanobiotechnology* 11 (July 2013), p. 25.

[118] M. Theodosiou et al. "Kindlin-2 cooperates with talin to activate integrins and induces cell spreading by directly binding paxillin." *eLife* 5 (Jan. 2016), e10130.

[119] W. Thomas. "Catch bonds in adhesion." *Annu. Rev. Biomed. Eng.* 10 (2008), pp. 39–57.

[120] T. Tlusty, A. Meller, and R. Bar-Ziv. "Optical Gradient Forces of Strongly Localized Fields." *Physical Review Letters* 81.8 (Aug. 1998), pp. 1738–1741.

[121] S. F. Tolić-Nørrelykke, E. Schäffer, J. Howard, F. S. Pavone, F. Jülicher, and H. Flyvbjerg. "Calibration of optical tweezers with positional detection in the back focal plane." *Review of Scientific Instruments* 77.10 (Oct. 2006), p. 103101.

[122] J. Wang, N. Shaner, B. Mittal, Q. Zhou, J. Chen, J. M. Sanger, and J. W. Sanger. "Dynamics of Z-band based proteins in developing skeletal muscle cells." *Cell Motil Cytoskeleton* 61.1 (2005), pp. 34–48.

[123] K. Wang, J. McClure, and A. Tu. "Titin: major myofibrillar components of striated muscle." *Proceedings of the National Academy of Sciences of the United States of America* 76.8 (Aug. 1979), pp. 3698–3702.

[124] M. D. Wang, H. Yin, R. Landick, J. Gelles, and S. M. Block. "Stretching DNA with optical tweezers." *Biophys J* 72.3 (1997), pp. 1335–46.

[125] M. D. Wang, M. J. Schnitzer, H. Yin, R. Landick, J. Gelles, and S. M. Block. "Force and velocity measured for single molecules of RNA polymerase." *Science (New York, N.Y.)* 282.5390 (Oct. 1998), pp. 902–907.

[126] K. Watanabe, P. Nair, D. Labeit, M. S. Kellermayer, M. Greaser, S. Labeit, and H. Granzier. "Molecular mechanics of cardiac titin's PEVK and N2B spring elements." *J Biol Chem* 277.13 (2002), pp. 11549–58.

[127] K. L. Wegener, A. W. Partridge, J. Han, A. R. Pickford, R. C. Liddington, M. H. Ginsberg, and I. D. Campbell. "Structural basis of integrin activation by talin." *Cell* 128.1 (Jan. 2007), pp. 171–182.

[128] M. Weitkunat, A. Kaya-Çopur, S. W. Grill, and F. Schnorrer. "Tension and Force-Resistant Attachment Are Essential for Myofibrillogenesis in Drosophila Flight Muscle." *Current Biology* 24.7 (Mar. 2014), pp. 705–716.

[129] Y. Wu, O. Cazorla, D. Labeit, S. Labeit, and H. Granzier. "Changes in titin and collagen underlie diastolic stiffness diversity of cardiac muscle." *J Mol Cell Cardiol* 32.12 (2000), pp. 2151–62.

[130] J. Yang et al. "Conformational activation of talin by RIAM triggers integrin-mediated cell adhesion." *Nature Communications* 5 (Dec. 2014), p. 5880.

[131] J. Yin, P. D. Straight, S. M. McLoughlin, Z. Zhou, A. J. Lin, D. E. Golan, N. L. Kelleher, R. Kolter, and C. T. Walsh. "Genetically encoded short peptide tag for versatile protein labeling by Sfp phosphopantetheinyl transferase." *Proceedings of the National Academy of Sciences of the United States of America* 102.44 (Nov. 2005), pp. 15815–15820.

[132] P. Young and M. Gautel. "The interaction of titin and alpha-actinin is controlled by a phospholipid-regulated intramolecular pseudoligand mechanism." *EMBO J* 19.23 (2000), pp. 6331–40.

[133] P. Young, C. Ferguson, S. Banuelos, and M. Gautel. "Molecular structure of the sarcomeric Z-disk: two types of titin interactions lead to an asymmetrical sorting of alpha-actinin." *EMBO J* 17.6 (1998), pp. 1614–24.

[134] P. Young, E. Ehler, and M. Gautel. "Obscurin, a giant sarcomeric Rho guanine nucleotide exchange factor protein involved in sarcomere assembly." *The Journal of Cell Biology* 154.1 (2001), pp. 123–136.

[135] T. S. Young and P. G. Schultz. "Beyond the canonical 20 amino acids: expanding the genetic lexicon." *The Journal of biological chemistry* 285.15 (2010), pp. 11039–44.

[136] J. Zhang, J. Yun, Z. Shang, X. Zhang, and B. Pan. "Design and optimization of a linker for fusion protein construction." *Progress in Natural Science* 19.10 (Oct. 2009), pp. 1197–1200.

[137] R. Zhang, J. Yang, J. Zhu, and X. Xu. "Depletion of zebrafish Tcap leads to muscular dystrophy via disrupting sarcomere-membrane interaction, not sarcomere assembly." *Human Molecular Genetics* 18.21 (Nov. 2009), pp. 4130–4140.

[138] P. Zou, N. Pinotsis, S. Lange, Y.-H. Song, A. Popov, I. Mavridis, O. M. Mayans, M. Gautel, and M. Wilmanns. "Palindromic assembly of the giant muscle protein titin in the sarcomeric Z-disk." *Nature* 439.7073 (Jan. 2006), pp. 229–233.